MEDITERRANEAN SHRUB CLASSIFICATION USING MULTI-TEMPORAL MULTI-SPECTRAL SATELLITE IMAGES

A THESIS SUBMITTED TO
THE GRADUATE SCHOOL OF NATURAL AND APPLIED SCIENCES
OF
MIDDLE EAST TECHNICAL UNIVERSITY

BY

INDIRA APRILIA LISTIANI

IN PARTIAL FULFILLMENT OF THE REQUIREMENTS
FOR
THE DEGREE OF MASTER OF SCIENCE
IN
GEODETIC AND GEOGRAPHIC INFORMATION TECHNOLOGIES

FEBRUARY 2021

Approval of the thesis:

MEDITERRANEAN SHRUB CLASSIFICATION USING MULTI-TEMPORAL MULTI-SPECTRAL SATELLITE IMAGES

submitted by **INDIRA APRILIA LISTIANI** in partial fulfilment of the requirements for the degree of **Master of Science in Geodetic and Geographic Information Technologies, Middle East Technical University** by,

Prof. Dr. Halil Kalıpçılar
Dean, **Graduate School of Natural and Applied Sciences** _____

Prof. Dr. Zuhal Akyürek
Head of the Department, **GGIT, METU** _____

Assoc. Prof. Dr. Uğur Murat Leloğlu
Supervisor, **GGIT, METU** _____

Dr. Uğur Zeydanlı
Co-Supervisor, **The Nature Conservation Center (DKM)** _____

Examining Committee Members:

Prof. Dr. Zuhal Akyürek
Dept. of Civil Eng., METU _____

Assoc. Prof. Dr. Uğur Murat Leloğlu
GGIT, METU _____

Prof. Dr. M. Lütfi Süzen
Dept. of Geological Eng., METU _____

Assoc. Prof. Dr. Cumhur Güngöroğlu
Dept. of Forest Eng., Karabük University _____

Asst. Prof. Dr. Semih Kuter
Dept. of Forest Eng., Çankırı Karatekin University _____

Date: 12.02.2021

I hereby declare that all information in this document has been obtained and presented in accordance with academic rules and ethical conduct. I also declare that, as required by these rules and conduct, I have fully cited and referenced all material and results that are not original to this work.

Name, Last name : Indira Aprilia Listiani
Signature :

ABSTRACT

MEDITERRANEAN SHRUB CLASSIFICATION USING MULTI-TEMPORAL MULTI-SPECTRAL SATELLITE IMAGES

Listiani, Indira Aprilia
Master of Science, Geodetic and Geographic Information Technologies
Supervisor: Assoc. Prof. Dr. Uğur Murat Leloğlu
Co-Supervisor: Dr. Uğur Zeydanlı

February 2021, 137 pages

Shrublands, which have a crucial role in retaining the ecological balance, constitute an important part of the Mediterranean ecosystems. However, their composition, distribution and dynamics are not well understood. It is necessary to know the distribution of the alliances at regional scale in order to construct models that explain their dynamics. Such models will help researchers to evaluate their role in ecosystems and predict their responses to climate change. Necessary alliance distribution maps can only be produced by employing remote sensing techniques. This study presents a methodology that generates alliance-level woodland/shrubland maps of the Mediterranean region in southern Turkey from satellite images using various machine learning techniques with different parameter combinations. Multi-temporal images are used to extract information from vegetation phenology. Topographic and meteorological data are also used for improving classification.

Cross-validation is performed using a ground-truth data set of 7452 polygons. Results show that detailed and accurate maquis shrubland classification is possible using a combination of environmental features and multi-spectral and multi-temporal satellite images. Addition of the environmental features to remotely sensed ones improved classification accuracy by 16%. The Random Forest (RF) algorithm is found to improve classification accuracy by 35.9% and 13.9% relative to Support Vector Machine and Quadratic Discriminant Analysis algorithms, respectively. Alliance-level classification maps of maquis acquired from RF classification are produced with 64.0-82.1% overall accuracy. Large-scale shrub classification method will have important implications on natural resource management and other ecological applications.

Keywords: Sentinel-2; Machine learning; Mediterranean shrub classification; Maquis; Shrubland;

ÖZ

ÇOK-ZAMANLI ÇOK-BANTLI UYDU GÖRÜNTÜLERİ KULLANARAK AKDENİZ ÇALI SINIFLANDIRMASI

Listiani, Indira Aprilia
Yüksek Lisans, Jeodezi ve Coğrafi Bilgi Teknolojiler
Tez Yöneticisi: Assoc. Prof. Dr. Uğur Murat Leloğlu
Ortak Tez Danışmanı: Dr. Uğur Zeydanlı

Şubat 2021, 137 sayfa

Ekolojik dengenin korunmasında çok önemli bir rol oynayan çalılıklar, Akdeniz ekosistemlerinin önemli bir bölümünü oluşturur. Bununla birlikte, bunların bileşimleri, dağılımları ve dinamikleri iyi anlaşılmamıştır. Alyansların dinamiklerini açıklayan modeller kurmak için bunların dağılımını büyük ölçekte bilmek gereklidir. Bu modeller, araştırmacıların bunların ekosistemlerdeki rollerini değerlendirmelerine ve iklim değişikliğine verdikleri yanıtları tahmin etmelerine yardımcı olacaktır. Gerekli alyans dağılım haritaları ancak uzaktan algılama teknikleri kullanılarak üretilebilir. Bu çalışma, Türkiye'nin güneyinde Akdeniz bölgesinde alyans düzeyinde ormanlık / çalılık haritalarını, çeşitli makina öğrenme tekniklerini kullanarak uydu görüntülerinden üreten bir algoritma sunmaktadır. Çok-zamanlı görüntüler, bitki örtüsü fenolojisinden bilgi elde etmek için kullanılmaktadır. Topoğrafik ve meteorolojik veriler de sınıflandırmayı iyileştirmek

için kullanılmaktadır. Çapraz-geçerleme, 7452 poligonluk saha ölçüm verileri kullanılarak gerçekleştirilmektedir. Sonuçlar, ayrıntılı ve doğru maki çalıları sınıflandırmasının, sayısal yükseklik modelleri ve çok-bantlı ve çok-zamanlı uydu görüntülerinin bir birleşimini kullanarak mümkün olduğunu göstermektedir. Çevresel özniteliklerin uzaktan algılamadan elde edilenlere eklenmesi sınıflandırma doğruluğunu %16 arttırmıştır. Rastgele Orman (RO) algoritmasının Destek Vektör Makinası ve İkinci Derece Ayırtaç Analizi algoritmalarına göre sınıflandırma doğruluğunu sırasıyla %35.9 ve %13.9 arttırdığı bulunmuştur. RO sınıflandırmasıyla elde edilen makinin alyans seviyesi sınıflandırma haritaları nihai olarak %64.0-82.1 toplam doğrulukla üretilmiştir. Büyük ölçekli çalı sınıflandırma yönteminin doğal kaynak yönetimi ve diğer ekolojik uygulamalar üzerinde önemli etkileri olacaktır.

Anahtar Kelimeler: Sentinel-2; Makine öğrenmesi; Akdeniz çalı sınıflandırması; Maki; fundalık ve çalılık;

I dedicate this thesis to my *ibu* and *bapak*.

ACKNOWLEDGMENTS

I would like to express my sincere gratitude to my supervisor Assoc. Prof. Dr. Uğur Murat Leloğlu for his guidance, advice, and criticism throughout this research. His continuous support was what made this thesis possible, and I am forever grateful to him for guiding me throughout my graduate studies.

I would also like to thank my co-supervisor, Dr. Uğur Zeydanlı, for his valuable insights and suggestions, and Doğa Koruma Merkezi (DKM), for providing me with the reference data required for this research.

I would also like to express my appreciation to the examining committee members, Prof. Dr. Zuhal Akyürek, Prof. Dr. M. Lütfi Süzen, Assoc. Prof. Dr. Cumhur Güngöroğlu, and Asst. Prof. Dr. Semih Kuter, for their valuable suggestions and comments.

I owe my deepest gratitude to my extended family for their endless support and motivation, especially to my mother and father for always giving me the best advice. I would not be where I am now without their trust, guidance, and their unconditional love for me.

And last but not least, I would like to thank Mehdi for his companionship, support, motivation, love, and trust.

TABLE OF CONTENTS

LIST OF TABLES

TABLES

LIST OF FIGURES

FIGURES

LIST OF ABBREVIATIONS

ABBREVIATIONS

AB	AdaBoost
a.s.l.	above sea level
BOA	Bottom-of-Atmosphere
CT	Classification Trees
DEM	Digital Elevation Model
DKM	Doğa Koruma Merkezi
ECOC	Error-Correcting Output Code
ESA	European Space Agency
EVI	Enhanced Vegetation Index
FF-ANNs	Feed Forward Artificial Neural Networks
FWHM	Full Width Half Maximum
GDVI	Generalized Difference Vegetation Index
GEE	Google Earth Engine
GT	Ground Truth
GVI	Green Vegetation Index
HydroSHEDS	**Hydro**logical data and maps based on **SH**uttle **E**levation **D**erivatives at multiple **S**cales
k-NN	k-Nearest Neighbors
MATLAB	Matrix Laboratory

MSI	Multi-Spectral Instrument
MTEs	Mediterranean-Type Ecosystems
NASA	National Aeronautics and Space Administration
NDVI	Normalized Difference Vegetation Index
NDWI	Normalized Difference Water Index
NIR	Near-Infrared
NN	Nearest Neighbor
OA	Overall Accuracy
PCABC	Principal Component Analysis-Based Classification
PA	Producer's Accuracy
QDA	Quadratic Discriminant Analysis
RF	Random Forest
RFE	Recursive Feature Elimination
RGB	Red Green Blue
SAR	Synthetic-Aperture Radar
SAVI	Soil Adjusted Vegetation Index
SRTM	Shuttle Radar Topography Mission
SST	Spectral-Spatial-Temporal
STP	Spectro-Temporal Pattern
SVM	Support Vector Machine
SWIR	Short-Wave Infrared
UA	User's Accuracy

VI	Vegetation Index
VNIR	Visible to Near-Infrared
WI	Water Index
WWF	World Wide Fund for Nature

CHAPTER 1

INTRODUCTION

1.1 Significance of the Mediterranean Ecosystem

The Mediterranean-type ecosystems (MTEs) are characterized by relatively high precipitation in winter and scarcity of it in summer. The most unique characteristic of the Mediterranean-type climates is the seasonality in air temperature and precipitation (Joffre & Rambal, 2001). Combination of high temperature and lack of moisture during the summer period with varying durations and the changes in yearly timing and amount of rainfall illustrate the profound influence that the Mediterranean-type climates have on the existing species as well as on the ecosystem (Médail, 2008).

Five extensively separated ecoregions of the world represent the MTEs. These ecoregions are parts of the Mediterranean Basin, California (Chaparral), central Chile, the southern and southwestern Cape Province of South Africa (South West Cape), and the southwestern and parts of southern Australia (South West Australia), which all together constitute the Mediterranean biome. They have clear similarities in terms of climatic trends, vegetation structure, as well as in the general landscape appearance and land-use patterns (Joffre & Rambal, 2001).

The five Mediterranean-climate regions exhibit unique and remarkable regional biodiversity. Although they make up less than 5% of the world's terrestrial surface, 48.250 of the Earth's known vascular plant species, approximately 20% of the world's total, can be found within the Mediterranean biome (Cowling et al., 1996),

with the Mediterranean Basin exhibiting the strongest heterogeneities of general and endemic plant species (Médail, 2008).

1.2 Research Problem

Shrublands, which have a crucial role in retaining the ecological balance, constitute an important part of Mediterranean ecosystems. Shrublands increase aggregate stability and reduce the movement of sediments, which limit soil erosion and control surface run-offs (Casermeiro et al., 2004). They help soil retain its organic matter content and increase the biochemical activities taking place within the soil, which in turn improve the soil profile, preparing it for the natural development of forest formation (Gabarrón-Galeote et al., 2013; Tomaselli, 1977). They create and maintain a microclimate that protects their surroundings (Tomaselli, 1977). From the economic point of view, shrublands provide benefits such as firewood, grass, and aromatic and pharmaceutical plants (Palahi et al., 2008), and are characteristic feature of the Mediterranean countryside, which constitutes recreational possibilities for tourists (Tomaselli, 1977).

Although shrublands have an evident significance, no adequate maps presenting the distribution of the maquis alliances exist, at least in most countries. Occasionally, it is simply marked as maquis, shrubland, or sparse forest, yet it is essential to know the distribution of the alliances at a large scale, mainly in order to construct models that explain their dynamics, as such models will help researchers to evaluate their role in ecosystems and predict their responses to climate change, but also for other benefits, such as forest fire prevention management (Baeza et al., 2005), better use of economic resources in maquis areas, and wildlife protection.

Maquis of the Mediterranean region make up approximately 20% of Turkey's 95.000 km^2 Mediterranean ecoregion (Olson et al., 2001), though the area is managed as if it is comprised of only tall trees (Demirbas Caglayan et al., 2020).

Obtaining maps showing the distribution of maquis types by surveying requires extensive amount of fieldwork, which is costly in time, labor, and resources, making the use of remote sensing far more advantageous for their assessment in larger spatial extents. Remote sensing is the best option to obtain these maps. Hence, a remote sensing-based method that can classify the shrublands in alliance-level is necessary.

1.3 Objectives of this Thesis

This study aims to classify the areas labelled as maquis at alliance level in the Mediterranean region of southern Turkey using Sentinel-2 Multi-Spectral Instrument (MSI) Level 2A data and several machine learning techniques.

Alliance is defined as a physiognomically uniform group characterized by a dominant tree species that extends over large geographic areas and varied environmental conditions (Grossman et al., 1998). In simpler terms, alliance is a vegetation class featured by the same dominant species and structural characteristics (e.g., short herbs, thorny plants, conifer trees).

This study presents a methodology to produce a map that shows the dominant alliances in Mediterranean shrublands. The results show that detailed and accurate maquis classification is possible using a combination of environmental parameters and multi-spectral and multi-temporal satellite images.

More specifically, the following are aimed in this thesis:

1. To classify maquis as accurately as possible with a large number of alliances.
2. To generate an alliance-level classification map of the maquis types.
3. To introduce new topographical features and remotely-sensed indices that help improve classification accuracy of maquis.

4. To explain the effects of environmental features on dominant maquis alliance distributions.

1.4 Research Innovations

Novel contributions of this study are listed as follows:

1. Alliance-level maquis classification at a regional scale using remote sensing and machine learning is demonstrated, and can efficiently be repeated for monitoring purposes as well as for further studies,
2. New topographical features that help improve the classification accuracy are introduced,
3. Large scale maps that will help to better understand the dynamics of forest and maquis are introduced,
4. Effects of environmental features on dominant maquis alliances distributions are explained and
5. New remotely-sensed indices helpful in discriminating maquis alliances are derived.

1.5 Structure of this thesis

This thesis is organized as follows:

CHAPTER 1 introduces the significance of the Mediterranean ecosystem. The research problem, objectives, innovations, and importance of this study are also described in this chapter.

CHAPTER 2 presents the background and literature review of woodland/shrubland classification in the Mediterranean region, including the general description of the Mediterranean region of southern Turkey, namely its topography, climate, ecology, and the important socio-economic considerations. The remote

sensing technology and various machine learning techniques and algorithms that have previously been applied for woodland/shrubland classification are also reviewed in this chapter.

CHAPTER 3 illustrates the exact boundaries of the study area and explains the datasets used in this study. The datasets used in this study include the Ground Truth (GT) polygons, Sentinel-2 MSI Level-2A reflectance data, the maquis mask, meteorological data, and topographical data.

CHAPTER 4 explains the methodology implemented in this study. The methodology is comprised of the feature extraction method, the classification algorithms, the feature selection process, and the accuracy assessment method.

CHAPTER 5 presents the ontology, the initial classification results, the feature selection results, the final classification results, the resulting classification maps, and the resulting classification accuracies.

CHAPTER 6 discusses the resulting classification maps and classification results for each of the three different classification schemes.

CHAPTER 7 presents a summary and conclusions drawn from this study. Recommendations for further research on shrubland classification in the Mediterranean region and possible applications of the results of this study are also presented.

CHAPTER 2

BACKGROUND AND LITERATURE REVIEW

2.1 Introduction

A biome is an extensive community of organisms with common characteristics, constructed by the pre-existing environmental conditions, such as climate and geology. The Mediterranean forests, woodlands, and scrubs biome mostly occurs within the Mediterranean climate zones, on the west coasts of all continents between latitudes 30^{o} and 40^{o} North and South of the equator, and is confined by the ocean-facing slopes of the continents upon which it resides. The Mediterranean biome covers roughly about 5% of the Earth's terrestrial surface (Cowling et al., 1996), making it one of the smallest biomes on the planet. However, an extraordinary amount of biodiversity can be found in this area regardless of its size.

Mediterranean ecosystems are indicated by rich spatiotemporal varieties of vegetation patterns (Shoshany, 2000). Understanding the constantly changing nature of these ecosystems calls for definite data of extensive regions. This compels the use of remote sensing satellites as well as interpretation methodologies that are suitable for ecological supervision over vast areas. In recent years, the use of spectral, temporal, and spatial information domains provided by satellite data to map the main vegetation types (forests, woodlands, scrub, dwarf shrubs, and herbaceous growth) in the Mediterranean region have been widely applied. Satellite sensors can observe relatively wide regions (e.g., the viewing swath width of SENTINEL-2 is 290 km) and several studies have confirmed the high potential of satellite data to generate specific maps of vegetation down to the species level (Clark, 2017, 2020; Grabska

et al., 2019; Immitzer et al., 2016; Karasiak et al., 2017; Kollert et al., 2021; Persson et al., 2018; Wessel et al., 2018).

In this chapter, the background introductory information is presented in Section 2.1. The general description of the study area, which includes the topography, climate, ecology, and the socio-economic importance of the Mediterranean Region of Turkey, is presented in Section 2.2. The literature review of woodland/shrubland classification studies are presented in Section 2.3.

The goal of this literature review is to summarize the research currently available that are relevant to the subject of this thesis: the application of satellite remote sensing in maquis classification, specifically to the maquis classification in the Mediterranean region.

2.2 General Description of the Study Area

2.2.1 The Topography of the Turkish Mediterranean Region

The Mediterranean Region (Turkish: Akdeniz Bölgesi) is a geographical region of Turkey. It is located near the Mediterranean Sea on the southern coast of Turkey, bordered by the Aegean Region to the west, the Central Anatolia Region to the north, the Eastern Anatolia Region to the northeast, the South-eastern Anatolia Region to the east, Syria to the southeast, and the Mediterranean Sea to the south. The land area is comprised of approximately 123.000 km^2 (47.500 sq mi). Elevation starts from sea level and reaches up to 3667 m above sea level (a.s.l.).

The Mediterranean Region of Turkey is mountainous. The Taurus Mountain complex runs from west to east, separating the Mediterranean coastal region from the central Anatolian Plateau, while the Amanos Mountains run from north to south covering the utmost eastern part of the region. The Çukurova coastal plain, formed

by the Berdan River, the Seyhan River, and the Ceyhan River, occupies the eastern area and is now the most important coastal plain of the region. The three main lakes of the region are Lake Beyşehir, Lake Eğirdir, and Lake Burdur, and together they form a closed basin area located in the north-west of the region.

The Mediterranean Region of Turkey spans over several provinces, namely: Adana, Antalya, Mersin, Burdur, Hatay, Isparta, and Osmaniye, while some others are only partially included, such as: Kahramanmaraş, Konya, Niğde, Kayseri, Denizli, Gaziantep, Muğla, Karaman, and Kilis.

2.2.2 The Climate of the Turkish Mediterranean Region

The Mediterranean Region of Turkey has a Mediterranean climate, which is portrayed by hot and moisture-less summers and cool and humid winters (Suc, 1984). According to the Turkish State Meteorological Service, the Mediterranean Region has an annual mean temperature of 15.3 ºC, while the mean minimum and maximum temperatures are 9.6 ºC and 21.4 ºC, respectively, and the annual mean precipitation is approximately 648.5 mm (TSMS - Turkish State Meteorological Service, 2020) as shown in Table 2.1. Measurement periods vary depending on cities. However, they were generally taken between 1930 – 2019.

Table 2.1. Annual mean meteorological data.

Provinces	Average Annual Temperature (ºC)	Average Annual Maximum Temperature (ºC)	Average Annual Minimum Temperature (ºC)	Annual Mean Precipitation (mm)
Adana	19.1	25.3	13.8	671.3
Antalya	18.7	24.1	13.7	1085.3
Mersin	19.1	23.3	14.7	615.8
Burdur	13.2	19.4	7.5	428.1
Hatay	18.3	23.1	14	1168.2
Isparta	12.2	18.3	6.1	570.2
Osmaniye	18.5	24.8	12.7	854.9
Kahramanmaraş	16.6	22.9	11.4	719.7
Konya	11.6	17.9	5.4	327.7
Niğde	11.2	17.5	5	344.5
Kayseri	10.6	18	2.9	389.2
Denizli	16.1	22.4	10.7	571.9
Gaziantep	15.2	21.5	9.3	568.5
Muğla	15.1	21.2	9.6	1214.8
Karaman	12	18.7	5.4	340.7
Kilis	17.1	23.4	11.7	505
Average	**15.3**	**21.4**	**9.6**	**648.5**

The Mediterranean climate is dominated by sclerophyll evergreen trees and shrubs (Joffre & Rambal, 2001), such as carob tree (*Ceratonia siliqua*), cork oak (*Quercus suber*), holm oak (*Quercus ilex*), mastic tree (*Pistacia lentiscus*), kermes oak (*Quercus coccifera*), and the fodder shrub (*Medicago arborea*) (Efe et al., 2008). However, under no conditions do they portray the majority of the total florae. The primary vegetation formations are called maquis.

2.2.3 The Ecology of the Turkish Mediterranean Region

Vegetation in the Mediterranean Region of Turkey varies noticeably in terms of its ecology in comparison to other Mediterranean biomes around the world. According to (Atalay & Efe, 2008), the Mediterranean Region of Turkey can be classified into three primary subregions, depending on altitude, soil, hydrologic, and geological conditions, namely: the Lower Subregion of the Mediterranean Zonobiome, which spreads out along the coastal belt of the Mediterranean region, the Mediterranean Mountain Forest Subregion, which encloses the mountainous areas between 800-1200 meters and rises up to 2000 meters, and the Mediterranean Grass-Steppic Subregion that only exists on the steep slopes that side to the south of the Bey Mountains, the Ak Mountains, and the Dedegöl Mountains. According to the existing literature, there exist three main vegetation groups within the Lower Subregion of the Mediterranean Zonobiome: 1) *Pinus brutia* forest; 2) Maquis; and 3) Garrigues (Atalay & Efe, 2008; Atalay et al., 2014a, 2014b; Efe et al., 2008).

Pinus brutia or Turkish Red Pine is one of the most common forest trees in Turkey. It is fairly abundant in the Mediterranean and is the climax tree species of the region (Atalay et al., 2014). This tree species has reached a steady state, making it best adapted to the climate of the Mediterranean Region. It is extremely immune to summer drought and has rapid regeneration skills. The main types of *Pinus brutia* in Turkey are *Pinus brutia Ten*. var. Agrophictii Papaj; *Pinus brutia Ten*. var. *pyramidalis* Selik; and *Pinus brutia Ten*. var. *densifolia* Yaltırık and Boydak (Efe et al., 2008).

Maquis is the natural Mediterranean vegetation, but grows as the shrub layer underneath *Pinus brutia* forests. Maquis develops when *Pinus brutia* forests are partly or completely destroyed. As a result, the maquis vegetation coincides to the natural development areas of *Pinus brutia* forests (Atalay & Efe, 2008). When *Pinus brutia* trees are surrounded by very few and scattered maquis stands, the seeds of the

trees are able to fall on the ground and germinate on open sunny sites among the maquis stands and, overtime, *Pinus brutia* will again seize the sparse maquis sites (Atalay et al., 2014; Atalay & Efe, 2008; Efe et al., 2008). However, under different circumstances, if the area is densely populated by maquis, red pine seeds would not be able to germinate as they would fall on top of the canopy cover of the surrounding maquis. Red pine seeds require bare soil rich in minerals and direct sunlight in order to germinate (Atalay et al., 2014). Natural competition is prevalent among *Pinus brutia* and maquis.

Maquis can be considered as a secondary succession type of vegetation for the Mediterranean Region of Turkey, with some of its most common species being: *Quercus coccifera*, *Arbutus unedo*, *Arbutus andrachne*, *Phillyrea latifolia*, *Olea europea* var. *sylvestris*, *Pistacia lentiscus*, *Pistacia terebinthus*, *Juniperus oxycedrus*, *Mrytus communis*, *Ceratonia siliqua*, *Spartium junceum*, *Vitex agnus castus*, *Nerium oleander*, and *Laurus nobilis* (Atalay & Efe, 2008).

Garrigues (phrygana) vegetation or low matorral vegetation is a regressive stage of succession type of vegetation (Efe et al., 2008) and is mostly widespread along the coastal areas of Turkey. They flourish and thrive at places where both maquis and red pine forests are completely cleared, dominating regions where the natural equilibrium had declined, such as burnt areas, abandoned fields, and poor habitats. The main garrigue vegetations are *Cistus salviifolius*, *Cistus criticus*, *Cistus parviflorus*, *Coridothymus capitatus*, *Erica verticillata*, *Fumana arabica*, *Fumana thymifolia*, *Genista acanthocloda*, *Micromeria nervosa*, *Majorana syriaca*, *Phlomis viscosa*, *Phlomis cretica*, *Salvia triloba*, *Sarcopoterium spinosum*, *Satureja thymbra*, *Thymbra spicata*, *Teucrium divaricatum*, *Teucrium creticum*, and the most common being *Poterium spinosum* (Atalay et al., 2014).

The Mediterranean Mountain Forest Subregion is the growing habitat of the black pine, cedar, fir, and some oak species. *Pinus nigra* or black pine prospers on soft and severely weathered bedrock, consisting of materials such as flysch, colluvial deposit,

and schist (Atalay et al., 2014). *Cedrus libani* or cedar is one of the climax trees of this region. It favors areas with thick snow cover, cool winds, and sunny habitats (Atalay & Efe, 2008). *Abies cilicica* or Taurus fir seldom stands alone. They can generally be found side-by-side with *Pinus nigra* and *Cedrus libani*, with optimum growth area between 1200-1800 m (Atalay et al., 2014). Juniper, such as *Juniperus excelsa* and *Juniperus foetidissima*, generally emerges in areas where cedar and black pine have been thoroughly damaged (Atalay & Efe, 2008). Oak forests frequently take place after the red pine forests end and around the beginning of the Mediterranean Mountain Forest Subregion, with some of the most typical species being: *Quercus infectoria*, *Quercus cerris*, *Quercus libani*, *Quercus frainetto* (Atalay & Efe, 2008; Atalay et al., 2014).

The Mediterranean Grass-Steppic Subregion is dominated by spiny cushion plants, such as the Acantholimon and Astragalus, both of which are extremely insusceptible to overgrazing (Atalay & Efe, 2008).

2.2.4 The Socio-Economic Value of the Turkish Mediterranean Region

The Mediterranean Region of Turkey spans over 16 different provinces. It has a considerable importance to the economy of Turkey. The Mediterranean basin is one of the main tourist destinations of the world (Almeida et al., 2014). Agricultural areas can be found along the coastal regions of the Mediterranean Sea. Plains spanning to the coastal belt are the dominant growing areas of citrus, vegetables, and flowers, some of which are being exported, while the central production of commercial agricultural come from the green houses in Antalya, Serik, and the Kumluca plains (Atalay & Efe, 2008).

The earliest settlement records in the Mediterranean Region dates back to the Paleolithic period. The forest areas have since been progressively damaged by

nomads due to animal grazing and for their cooking and heating necessities (Atalay & Efe, 2008).

Despite their benefits, social and economic activities also impose stress on the ecological environment of the Mediterranean Region. Consequently, environmental management needs to be strengthened.

2.3 Woodland / Shrubland Classification Studies

2.3.1 Remote Sensing Technologies for Classification of Woodland/Shrubland

In recent years, remote sensing technologies have been broadly applied for vegetation classification within the Mediterranean Region (Shoshany, 2000). Woodland/shrubland classification with remote sensing technology is pursued by interpreting the satellite sensors' signals in the spectral, temporal, and spatial domains. Various open access satellite sensor systems support essential data for regional scale vegetation classification, such as Sentinel, the Landsat Thematic Mapper, MODIS, RADARSAT, the Landsat Multi-Spectral Sensor, and ERS SAR. Satellite sensors can observe relatively wide regions (e.g., the swath width of SENTINEL-2 is 290 km). This presents opportunities to cover large areas at comparatively low costs in contrast with the conventional method of labor-intensive fieldwork.

Extensive application of satellite data for vegetation classification indicates that the spectral channels possess high capabilities for differentiating between flora. Multi-spectral classification methodologies have been proven to be able to classify the following vegetation types: forest (oak and conifer), woodland, chaparral, grassland, and low-density vegetation (Brodley & Friedl, 1997). Several approaches are available in order to promote classification accuracy as well as to acquire more

detailed classification outcomes, such as including band ratios and vegetation indices in the classification. Clark (2020) generated an alliance-level map of detailed forest alliances, specified by indicative plant species from the superior or preeminent growth form, using simulated multi-seasonal Sentinel-2 data in a Mediterranean-climate landscape. Results from this classification were then compared with simulated hyperspectral satellite data for the same study site and reference data (Clark et al., 2018). Clark (2020) concluded that hyperspectral-based classification performed only 1.6% slightly better than the Sentinel-2-based classifier. Grignetti et al. (1997) incorporated Landsat TM and SPOT, along with multi-temporal TM data in their studies to classify eight main natural Mediterranean vegetation communities. Kampouri et al. (2019) implemented fuzzy rules, established on topographic factors (e.g., altitudes and slope) for the dispersion of each tree species, obtained from professional judgement and in-situ measurements, in order to increase the accuracy of tree species classification.

The high seasonal variability of vegetation traits in the Mediterranean climates compels the need to pick an optimal date for the satellite images. Hardships in obtaining images at optimal dates have led to the use of multi-spectral classifications that are applied to combinations of multi-date images (Cheng & Wang, 2019; Grabska et al., 2019; Kampouri et al., 2019; Persson et al., 2018; Shoshany, 2000). Vegetation classification using multi-temporal satellite data encompassing vast areas has been proclaimed since the prime work of Justice et al. (1985). Combinations of multi-date images enable researchers to analyze the fluctuations of vegetation indices (VI) overtime. There are natural relationships between vegetation types, their environmental governing components, and their periodic VI changes. Seasonal deviations in the sensors' response are, to some extent, caused by variations in the surface vegetation characteristics (Shoshany, 2000), though, intermittently, they can also be caused by variations in the sensor viewing and sun illumination angles between time of acquisition. The most crucial multi-date methodologies for

vegetation classification make use of phenological data, such as mean value and difference between maximum and minimum VI values (Justice et al., 1985). Classification of the unprocessed seasonal VI variations and of mixture of phenological parametrizations had been implemented by using several different procedures, such as the hybrid tree classification (Brodley & Friedl, 1997); Random Forest (RF) algorithm and Recursive Feature Elimination (RFE) (Demirbas Caglayan et al., 2020); Integrated Spectral-Spatial-Temporal Features and RF algorithm (Cheng & Wang, 2019); Support Vector Machine (SVM), Nearest Neighbor (NN), RF, and Classification Trees (CT) algorithms (Macintyre et al., 2020); RF algorithm (Grabska et al., 2019).

On account of the effects that environmental conditions, such as climate and topography, have on the dynamic nature of plant spectral signatures (Castro-Esau et al., 2006), remotely sensed features are seldom used for vegetation mapping at species-level on their own. Zimmermann et al. (2007) concluded that there exists a significant correlation between climate and remotely sensed features. Domaç & Süzen (2006) combined Landsat images and environmental variables (i.e., DEM, slope, geology, aspect, and forest data) as ancillary data in regional scale vegetation classification. Accurate and precise assessments of the environmental conditions are required in order to yield reliable classification predictions (Evans et al., 2011).

Several studies have implemented remote sensing technologies for woodland/shrubland classification in the Mediterranean climate. Bajocco et al. (2012) classified maquis as a single group, Maselli et al. (2000) divided the classification results into three different categories on the basis of its height, Laurin et al. (2018) conducted the classification based on density or coverage, De Jong & Burrough (1995) classified maquis based on its physiological classes, and Manevski et al. (2011) conducted classification of maquis down to the species-level using field spectrometry, yet extensive fieldwork was required. Demirbas Caglayan et al. (2020)

introduced a detailed level classification scheme for the dominant maquis species, however, the study was limited to a small area.

2.3.2 Machine Learning Techniques and Algorithms for Classification of Woodland/Shrubland

The main objectives of woodland/shrubland classification via remote sensing is to predict the class of given data points by using the information enclosed in the image, such as the spectral patterns, spatial patterns, as well as temporal patterns, and to generate a thematic map of the study area.

There are two major types of classification, which are: supervised and unsupervised classification or clustering (Mather & Tso, 2016). In supervised classification, the class labels in the study area are known beforehand by the user. In unsupervised classification, on the other hand, the class labels are obscure, and the user gets to decide the number of separable classes along with their labels. However, a combination of both is also possible (hybrid classification).

For example, Wessel et al. (2018) evaluated several machine learning algorithms for classification of tree types based on Sentinel-2 data, and the best performance was found to be achieved by using object-based multi-temporal SVM approach. Dadon et al. (2019) applied an improved Principal Component Analysis-Based Classification (PCABC) by combining unsupervised classification along with reduction of data size to classify Mediterranean forest species. Cheng & Wang (2019) proposed a forest type classification framework based on Spectral-Spatial-Temporal (SST) features and the RF algorithm. Lapini et al. (2020) compared several machine learning methods (AdaBoost with decision trees (AB), SVM, k-Nearest Neighbors (k-NN), Feed Forward Artificial Neural Networks (FF-ANNs), RF, and Quadratic Discriminant Analysis (QDA)) by applying them to Synthetic-Aperture Radar (SAR) images for forest classification in Mediterranean areas, and found that

the best overall accuracy was achieved by RF classification. Caprioli et al. (2003) implemented a hybrid land cover classification for an efficient vegetation mapping.

Knowledge-based algorithms are important for boosting the quality of environmental information acquired from satellite images. Awareness regarding the existence and importance of transitional patterns representing successional stages is necessary in order to achieve this (Shoshany, 2000).

Demirbas Caglayan et al. (2020) demonstrated the effectiveness of RFE selection procedure and RF classifier for an accurate mapping of the dominant maquis formations in the Mediterranean region. Thereupon, RF and RFE were applied in this study for classifying the Mediterranean shrubland.

CHAPTER 3

DATA

3.1 Introduction

The objective of this chapter is to illustrate the exact location of the study area and to describe the data used in this study. Section 3.2 illustrates the precise location boundaries of the study area. Section 3.3.1 describes the Ground Truth (GT) polygons. Section 3.3.2 describes the Sentinel-2 MSI Level-2A reflectance data. Section 3.3.3 describes the maquis mask, and Section 3.3.4 describes the ancillary datasets.

3.2 The Study Area

The study area, covering an area of approximately 95.000 km^2, is shown in Figure 3.1. It encompasses the Mediterranean Region of Turkey, which was based on the Mediterranean forests, woodlands, and scrub terrestrial ecoregion (Olson et al., 2001), modified by the Nature Conservation Centre/Doğa Koruma Merkezi (DKM) in 2018. It is located between 27.3 – 37.2^o E and 35.8 – 38.4^o N. Maquis or shrublands of the Mediterranean region make up approximately 20% of the total area (Olson et al., 2001), though the area is managed as if it is comprised of only tall trees (Demirbas Caglayan et al., 2020). Figure 3.2 illustrates the distribution of maquis in the study area according to forest stand maps.

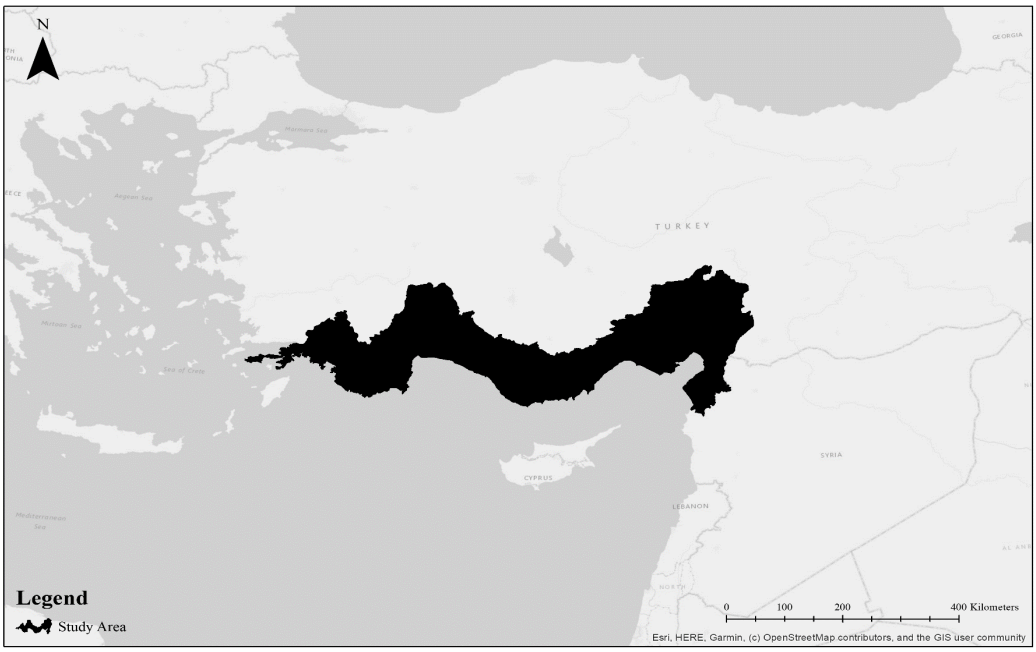

Figure 3.1. Location of the study area in southern Turkey.

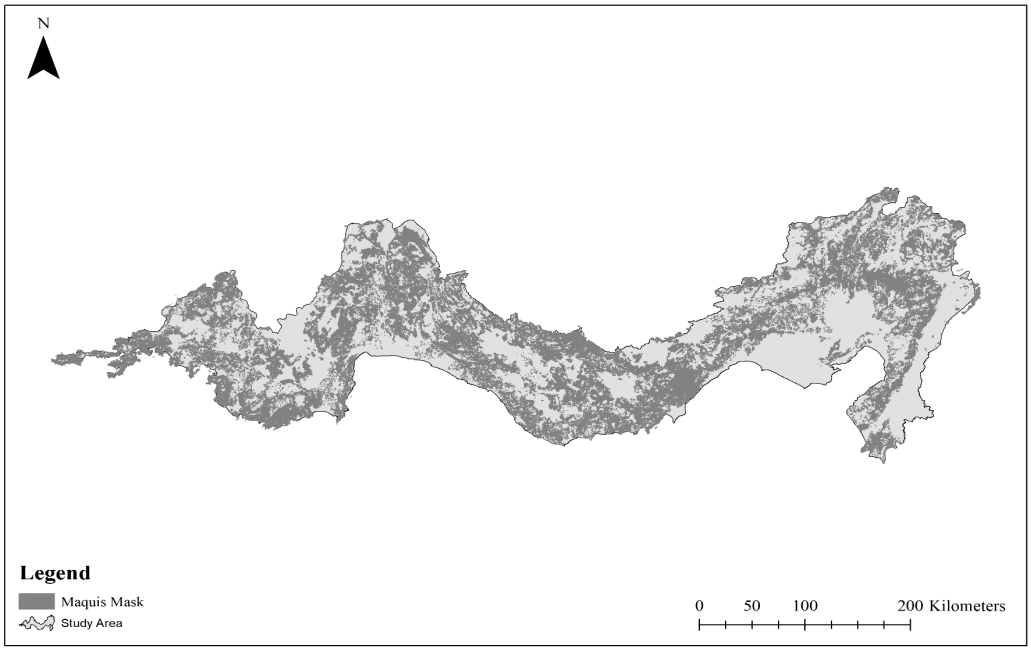

Figure 3.2. Maquis mask (provided by DKM) overlaying the study area.

3.3 Data Collection

3.3.1 Ground Truth (GT) Polygons

The Nature Conservation Centre (DKM) conducted a field survey between the years of 2016 – 2018 in order to obtain the Ground Truth (GT) data (Caliskan & Zeydanli, 2020). The GT data were originally collected as points. In this study, in order to reduce the noise in the data, these points were converted into polygons by creating a buffer zone around each point. Alliances with typically very small stands were converted into circular areas with 10 m radius (i.e., *Genista acanthoclada*, *Erica arborea, and Laurus nobilis*), while the rest of the alliances were converted into circles with 40 m radius. Figure 3.3 shows the distribution of the GT data in the study area.

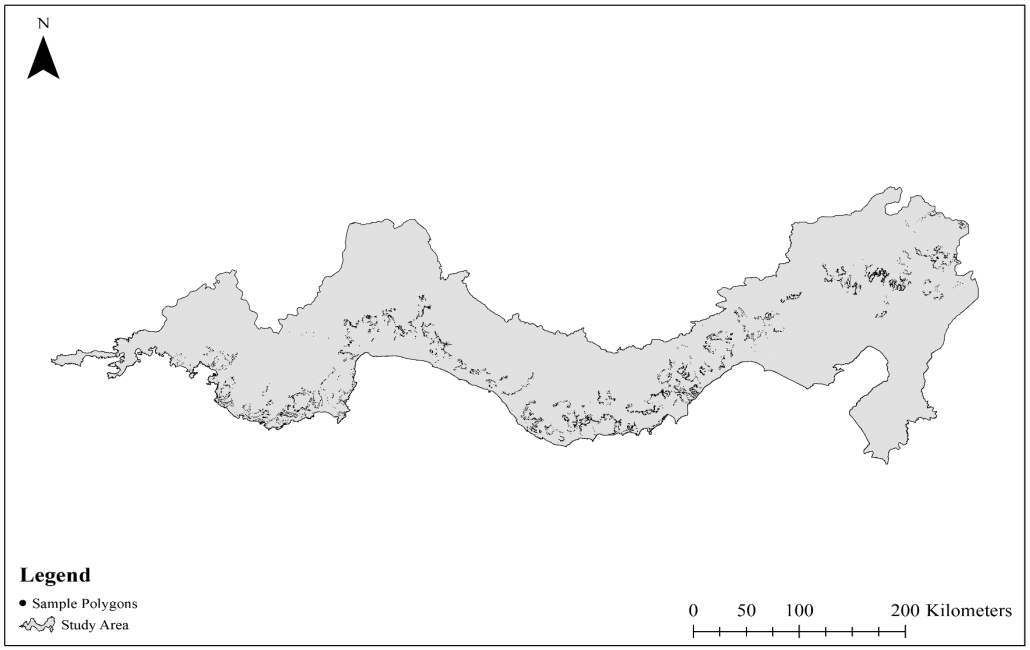

Figure 3.3. Distribution of the Ground Truth data (provided by DKM) in the study area.

3.3.2 Sentinel-2 MSI Level-2A Reflectance Data

Sentinel-2 MSI, developed by ESA (The European Space Agency, 2020), is a wide-swath, high-resolution, multi-spectral imaging mission. It measures the Earth's reflected radiance in 13 spectral bands from visible (VIS) to near-infrared region (NIR) to short-wave infrared (SWIR) and has a global 5-day revisit frequency which facilitates well in change detection analysis. Sentinel-2 has 10 m resolution visible and VNIR bands, making it especially significant for vegetation analysis, four bands (5, 6, 7, 8a) of 20 m resolution in the red-edge region of the electromagnetic spectrum and two bands (11, 12) of 20 m resolution in the SWIR, as shown in Table 3.1 (SENTINEL-2 User Handbook, 2013). The Bandwidth (nm) values shown in Table 3.1 is measured at Full Width Half Maximum (FWHM).

Sentinel-2A was launched on June 2015 and was later joined in orbit by its sister satellite, Sentinel-2B on March 2017. Sentinel-2 Level-2A dataset, which is comprised of Sentinel-2A as well as Sentinel-2B, started to become available on Google Earth Engine (GEE) from the end of March 2017. Since the GT data were collected between 2016 – 2018, Sentinel-2 images from 2018 were chosen in order to ensure that the satellite constellation had been fully functional and to minimize the effects of landscape changes.

Table 3.1. Sentinel-2 Bands' Central Wavelength (nm) and Bandwidth (nm) information.

Band Number	Sentinel-2A		Sentinel-2B	
	Central Wavelength (nm)	Bandwidth (nm)	Central Wavelength (nm)	Bandwidth (nm)
1	442.7	21	442.2	21
2	492.4	66	492.1	66
3	559.8	36	559	36
4	664.6	31	664.9	31
5	704.1	15	703.8	16
6	740.5	15	739.1	15
7	782.8	20	779.7	20
8	832.8	106	832.9	106
8a	864.7	21	864	22
9	945.1	20	943.2	21
10	1373.5	31	1376.9	30
11	1613.7	91	1610.4	94
12	2202.4	175	2185.7	185

GEE (Gorelick et al., 2017) is a cloud computing platform with ready-to-use datasets that are instantly available, making it very convenient for large-scale geospatial analysis. Results acquired by Clark (2017) suggested that repeat image acquisitions from satellite sensors are vital for land-cover classification, regardless of the sensor spectral resolution. Sentinel-2 Level-2A orthoimages Bottom-of-Atmosphere (BOA) corrected reflectance values for each GT polygon between 2018-01-01 and 2018-12-31 were acquired from GEE. A cloud-free pixel mask was applied to these images in order to guarantee substantial cloud-free pixels. Sentinel-2 bands B2, B3, B4, B8, B11, B12 (corresponding to blue, green, red, near-infrared (NIR), SWIR1, and SWIR2) were mostly used in the analysis, with the addition of B5, B6, and B7 (vegetation red-edge bands) to account for the phenological differences. Previous

studies that implemented Sentinel-2 data confirmed its high potential to generate specific maps of vegetation down to the species-level (Clark, 2017, 2020; Grabska et al., 2019; Immitzer et al., 2016; Karasiak et al., 2017; Kollert et al., 2021; Persson et al., 2018; Wessel et al., 2018). Figure 3.4 shows the true color composite (RGB) of Sentinel-2A image of the study area. The composite is composed of images taken in 2018 with the least cloud cover.

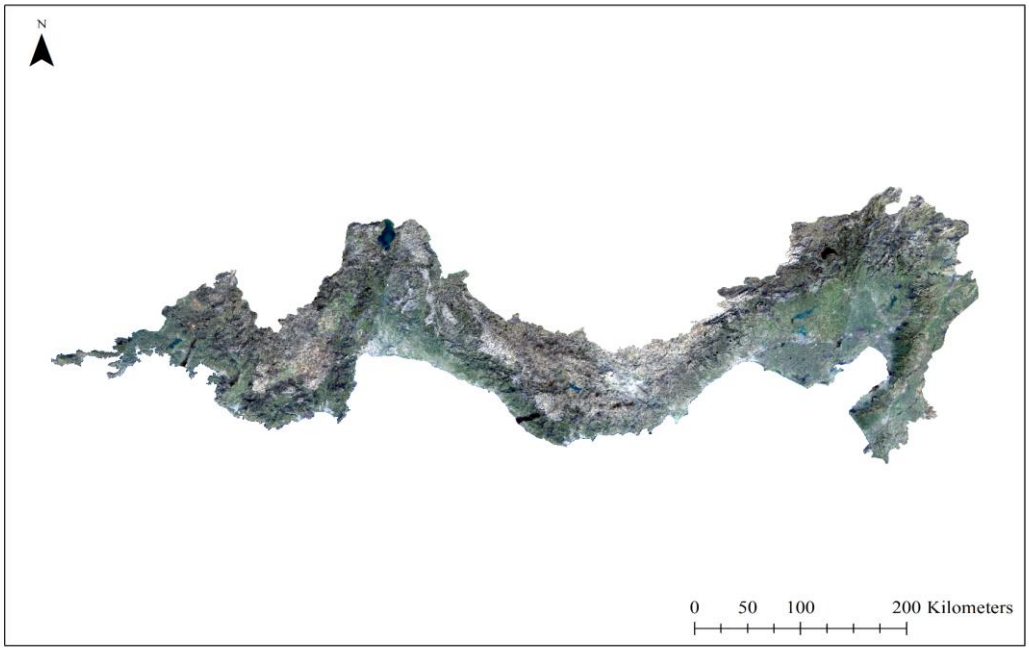

Figure 3.4. True color composite (RGB) of the study area.

3.3.3 Maquis Mask

As previously mentioned, in addition to all of the features explained above, a "maquis mask" is also used in this study. This maquis mask, provided by the Nature Conservation Centre (DKM), supports the algorithm to classify maquis by minimizing the area upon which the algorithm is carried out. It is used to classify the pixels that represent maquis, which conceivably could improve the classification

results. However, the area covered by the mask may still include small patches of areas covered with trees, rocks or grass.

3.3.4 Ancillary Datasets

In order to accurately classify the allocation of maquis at alliance level, a total of 23 environmental features (18 bioclimatic and five topographical) are acquired in addition to the remotely sensed features. Soil and geology datasets might also be useful for improving the classification, however, since these datasets are not available for this study, they are not further discussed.

Initially, there are 19 bioclimatic features as shown in Table 3.2, but BIO7 (temperature annual range ($BIO5 - BIO6$)) is excluded simply because the difference of two other features does not bring any novelty from the viewpoint of machine learning.

Apart from the remotely sensed features and environmental features, a shrubland cover map -herein referred to as "maquis mask"-, is also utilized. The mask shows areas having the status of forest but not covered with tall trees.

3.3.4.1 Meteorological Features (WorldClim BIO Variables V1)

Alliances are affected by both climatic and non-climatic factors. Climate change can impose physiological restrictions on alliances which can shape their distributions. Bioclimatic predictors are derived from climatic data sources to improve the representation of seasonal trends closely related to the physiological restrictions of different species (O'donnell & Ignizio, 2012).

WorldClim BIO Variables V1 is applied in this study as an ancillary dataset to further develop understanding of the alliance distributions throughout the study area. This dataset provides bioclimatic variables that are derived from the monthly temperature

and precipitation values in order to create more biologically meaningful values (Hijmans et al., 2005). The bioclimatic variables illustrate annual trends, seasonality, and extreme or limiting environmental factors. All of the bioclimatic variables used in this study are listed in Table 3.2.

Table 3.2. WorldClim BIO Variables V1 used in this study.

BIO1	Annual Mean Temperature
BIO2	Mean Diurnal Range $(\overline{Monthly\ maximum\ temperature - Monthly\ minimum\ temperature})$
BIO3	Isothermality (BIO2/BIO7) (x100)
BIO4	Temperature Seasonality (standard deviation x100)
BIO5	Maximum Temperature of Warmest Month
BIO6	Minimum Temperature of Coldest Month
BIO8	Mean Temperature of Wettest Quarter
BIO9	Mean Temperature of Driest Quarter
BIO10	Mean Temperature of Warmest Quarter
BIO11	Mean Temperature of Coldest Quarter
BIO12	Annual Precipitation
BIO13	Precipitation of Wettest Month
BIO14	Precipitation of Driest Month
BIO15	Precipitation Seasonality (Coefficient of Variation)
BIO16	Precipitation of Wettest Quarter
BIO17	Precipitation of Driest Quarter
BIO18	Precipitation of Warmest Quarter
BIO19	Precipitation of Coldest Quarter

3.3.4.2 Topographical Features

Two different datasets are used in this study in order to extract the topographical features, namely the Shuttle Radar Topography Mission (SRTM) Digital Elevation Data Version 4 (Jarvis et al., 2008) and the World Wide Fund for Nature (WWF) **Hydro**logical data and maps based on **SH**uttle **E**levation **D**erivatives at multiple **S**cales (HydroSHEDS) data (Lehner et al., 2008). A total of five topographical features are calculated: elevation, slope, distance to streams, distance to ridges and surface curvature. Slope and surface curvature are derived from Digital Elevation

Model (DEM), while distance to streams and distance to ridges are derived from the WWF HydroSHEDS data.

3.3.4.2.1 SRTM Digital Elevation Data Version 4

SRTM Digital Elevation Version 4 dataset (Jarvis et al., 2008) is used in this study as elevation feature and to extract slope and surface curvature. This dataset is of 90 m resolution.

Surface curvature outlines how much the surface is bending in a given direction at a particular point and is related to peaks, pits, and flats in digital images (Peet & Sahota, 1986). This topographical feature anticipates to consider the location of alliances that are situated within areas that might be overlooked by the satellite images.

3.3.4.2.2 WWF HydroSHEDS Data

WWF HydroSHEDS is a mapping product that supplies hydrographic information for regional and global-scale applications in a consistent format (Lehner et al., 2008). It provides geo-referenced vector and raster datasets at various scales, including river networks, watershed boundaries, drainage directions, and flow accumulations. HydroSHEDS is based on high-resolution elevation data acquired in 2000 during a Space Shuttle flight for National Aeronautics and Space Administration's (NASA) SRTM (Jarvis et al., 2008). WWF HydroSHEDS Free Flowing Rivers Network v1 (Lehner & Grill, 2013) and WWF HydroSHEDS Basins level 12 (Lehner & Grill, 2013) are used to calculate the distance to streams and distance to ridges from each GT polygon, respectively.

CHAPTER 4

METHODOLOGY

4.1 Introduction

The objective of this chapter is to explain the methodology implemented in this study. Section 4.2 demonstrates the feature extraction method. Section 4.3 explains the classification algorithms implemented in this study. Section 4.4 demonstrates the feature selection process, and Section 4.5 explains the accuracy assessment method implemented in this study. The flowchart showing the steps of the proposed methodology is shown in Figure 4.1. Details of the methods are explained in the following sections.

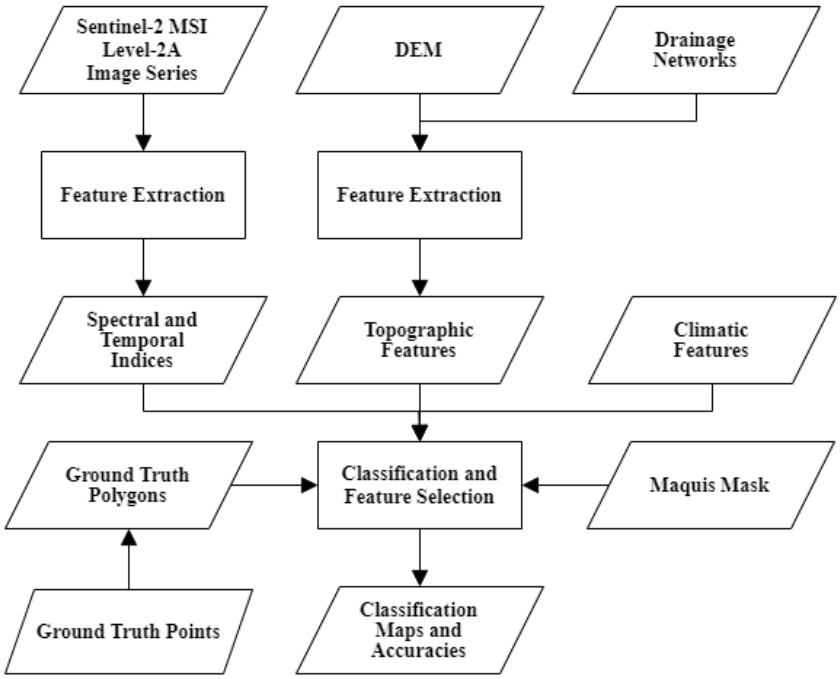

Figure 4.1. The flowchart of the proposed methodology.

4.2 Feature Extraction

Table 4.1 and Table 4.2 list all the potential features used in this study. In total, 118 features were extracted for each ground truth polygon: 54 features derived from the vegetation and water indices (i.e., NDVI, NDWI, SAVI, EVI, GVI, and GDVI) calculated for all the months (except winter months: December, January, and February), 23 environmental features, 24 coefficients derived from cubic polynomials fitted on the surface of all the VIs, nine coefficients inferred from the spectro-temporal patterns (STP), and eight additional newly computed spectro-temporal indices. Combining multi-spectral bands and indices or using just bands

was generally more accurate than relying on just indices for classification (Clark, 2020).

Table 4.1. List of Vegetation Indices (VI), Water Index (WI), and Environmental features.

Vegetation Indices (VI) and Water Index (WI)	**Environmental Features**
NDVI	Elevation (DEM)
NDWI	Slope
SAVI	Distance to Streams
EVI	Distance to Ridges
GVI	Surface Curvature
GDVI	Bioclimatic

Table 4.2. List of spectro-temporal indices.

Feature Name	Formula
Feature1	$\frac{(AugustB3 - AugustB4)}{(AugustB3 + AugustB4)}$
Feature2	$\frac{(AugustB11 - AugustB8)}{(AugustB11 + AugustB8)}$
Feature3	$\frac{(JulyB11 - JulyB12)}{(JulyB11 + JulyB12)}$
Feature4	$\frac{(MarchB11 - MarchB8)}{(MarchB11 + MarchB8)}$
Feature5	$\frac{(MayB11 - MayB8)}{(MayB11 + MayB8)}$
Feature6	$\frac{(MayB3 - MayB2)}{(MayB3 + MayB2)}$
Feature7	$\frac{(B3January - B3March)}{(B3January + B3March)}$
VI-fitted polynomials	$f(x) = p_1x^3 + p_2x^2 + p_3x + p_4$
Spectro-Temporal Patterns (STP)	$(x, y) = p_{00} + p_{10}x + p_{01}y + p_{20}x^2 + p_{11}xy + p_{02}y^2 + p_{21}x^2y + p_{12}xy^2 + p_{03}y^3$
Normalized Summer-Winter NDVI	$\frac{(\overline{Summer\ NDVI} - \overline{Winter\ NDVI})}{(\overline{Summer\ NDVI} + \overline{Winter\ NDVI})}$

4.2.1 Remotely-Sensed Features

Vegetation Index (VI) (i.e., NDVI, SAVI, EVI, GVI, and GDVI) and Water Index (WI) values (i.e., NDWI) were calculated monthly for each pixel inside each GT polygon, and the mean value was taken to represent each polygon. The whole process was done on the GEE cloud computing platform using Sentinel-2 Level-2A images that covered the study area between March 2018 and November 2018. Three months of the year (i.e., December, January, and February) were excluded for the indices' calculations because the significant snow cover during the winter months at high altitudes interfered with the surface reflectance values. Images for the month of

March was extended to include those between 2018-02-20 and 2018-04-10, since there were not enough images with substantial cloud and snow free pixels within the 31 days of March 2018 for a small number of polygons.

VIs are mathematical calculations of spectral bands that strengthen sensitivity towards vegetation properties in order to differentiate them from the other features present in the image as well as to minimize unwanted factors (e.g., soil background reflectance and atmospheric effects). Each index is designed to enhance a particular vegetation property. As mentioned above, this study implemented six indices, namely: NDVI, NDWI, SAVI, EVI, GVI, and GDVI. These indices are chosen in reference to results obtained by Demirbas Caglayan et al. (2020), who conducted a similar study.

Normalized Difference Vegetation Index (NDVI) is a numerical indicator of vegetation greenness that ranges from -1 to 1, with its earliest formal reporting dating back to 1973 (Rouse et al., 1973). NDVI attempts to indicate the amount of vegetation present in the image, to distinguish vegetation from soil, and to minimize the topographic effects. However, NDVI does not eliminate atmospheric effects.

The mathematical formula of NDVI for Sentinel-2 is given as:

$$NDVI = \frac{(B8 - B4)}{(B8 + B4)} \tag{4.1}$$

where B8 and B4 stand for band 8 (NIR) and band 4 (red), respectively. The red channel is located in the strong chlorophyll absorption region, while the NIR channel is located in the high reflectance plateau of vegetation canopies (Gao, 1996).

NDVI time-series needs to be smoothed before being used because some noise, which could be caused by remnants of cloud cover, water, snow, or shadow, high scan angle or transmission errors could still be present in the dataset (Pettorelli et al., 2005).

Normalized Difference Water Index (NDWI) resembles the NDVI methodology. NDWI employs the information contained in the NIR channel to monitor the change of water content of leaves and was developed from work done by (Gao, 1996). The mathematical formula of NDWI for Sentinel-2 is given as:

$$NDWI = \frac{(B8 - B11)}{(B8 + B11)} \tag{4.2}$$

where B8 and B11 stand for band 8 (NIR) and band 11 (SWIR), respectively. Because the atmospheric aerosol scattering effects in the 0.86–1.24 μm region are weak, NDWI is less sensitive to atmospheric effects than NDVI (Gao, 1996).

Since the creation of NDVI, attempts have been made in order to reduce the effects of the variable soil background and SAVI is one of them (Huete, 1988). Soil Adjusted Vegetation Index (SAVI) adds a constant term L to the NDVI equation in an attempt to normalize soil variations (Acker et al., 2014). The constant term L is a soil factor that varies from 0 to 1.

The mathematical formula of SAVI for Sentinel-2 is given as:

$$SAVI = \frac{(B8 - B4)}{(B8 + B4 + L)}(1 + L) \tag{4.3}$$

where B8 and B4 represent band 8 (NIR) and band 4 (red), respectively. In this study, L is set to 0.5.

Another VI used in this study is the Enhanced Vegetation Index (EVI). EVI supplies increased sensitivity in high biomass regions and attempts to correct for atmospheric and soil variations and for feedback between the two corrections (Acker et al., 2014). The mathematical formula of EVI for Sentinel-2 is given as:

$$EVI = \frac{(B8 - B4) \times 2.5}{(B8 + 2.4 \times B4 + 1)} \tag{4.4}$$

where B8 and B4 stand for band 8 (NIR) and band 4 (red), respectively.

Greenness Vegetation Index (GVI) or the Tasseled Cap Vegetation Index minimizes the effects of background soil while emphasizing green vegetation (Kauth & Thomas, 1976).

The mathematical formula of GVI for Sentinel-2 is given as:

$$GVI = (-0.283 \times B2) + (-0.2453 \times B3) + (-0.5436 \times B4) + (0.724 \times B11) + (-0.18 \times B12) \tag{4.5}$$

where B2, B3, B4, B11, and B12 refer to band 2 (blue), band 3 (green), band 4 (red), band 11 (SWIR1), and band 12 (SWIR2), respectively.

All previous indices have low sensitivity in areas with low vegetation cover. Generalized Difference Vegetation Index (GDVI) attempts to aid assessments of dryland environment (i.e., low vegetation cover). GDVI, developed by (Wu, 2014), has higher sensitivity and dynamic range in the low vegetal biomes.

The mathematical formula of GDVI for Sentinel-2 is given as:

$$GDVI = \frac{(B8^n - B4^n)}{(B8^n + B4^n)} \tag{4.6}$$

where B8 and B4 correspond to band 8 (NIR) and band 4 (red), respectively. In this study, the constant n is set as 2. When n is 1, GDVI = NDVI. The higher power of GDVI (n = 3, 4) is only applicable for extremely sparse vegetated regions (e.g., for monitoring land degradation and desertification) (Wu, 2014).

In addition to the VIs and WI, new features based on said indices are derived by fitting a cubic polynomial with robust fitting on all vegetation and water index data. The time series of the indices are noisy, but the polynomials can capture the phenology without the effect of the noise and clutter. The resulting coefficients are then added as new features for the RF classifier algorithm. The cubic polynomial fitted on the indices is given as:

$$f(x) = p_1x^3 + p_2x^2 + p_3x + p_4 \tag{4.7}$$

where $f(x)$ refers to the vegetation and water index values, x refers to the month (i.e., March to November), and p_1 until p_4 refer to the coefficients.

Additional new features are derived based on the spectro-temporal patterns by fitting a two-dimensional polynomial surface of second degree for the bands (x) and third degree for the months (y) on any given GT data. The coefficients of this polynomial are also added as nine new features.

The two-dimensional polynomial surface is given as:

$$(x, y) = p_{00} + p_{10}x + p_{01}y + p_{20}x^2 + p_{11}xy + p_{02}y^2 + p_{21}x^2y + p_{12}xy^2 + p_{03}y^3 \quad (4.8)$$

To account for the phenological differences between certain alliances, eight additional indices were also calculated. These indices are derived by averaging the reflectance values of each class and plotting them over wavelengths and time. By inspecting the behaviors of the spectral signatures of the classes in each month and the temporal changes of each band for all classes, bands that could help in discriminating classes were identified.

Feature1 – Feature 6 are spectral features while Feature7 is a temporal feature. Feature1 is based on August spectra as shown in Figure 5.12. Alliances like *Juniperus spp.* (Jun) and *Genista acanthoclada* (Brm) increase from B3 (Green) to Bd 4 (Red), while *Arbutus andrachne* (EST), *Laurus nobilis* (Bay) and *Pinus brutia* (TRP) decrease.

As can be seen in Figure 5.12, some alliances (e.g., Jun and Brm) have higher reflectance in B11 (SWIR) with respect to B8 (NIR), while others (e.g., EST and Bay) have lower reflection. Feature2 is designed to accentuate this behavior in August. This index is normalized to reduce the effect of canopy coverage differences along with all the following new features.

The rest of the features are derived using similar reasonings. For Feature3 – Feature7, reference can be made to Figure 5.11, Figure 5.7, Figure 5.9, and Figure 5.31, respectively.

4.2.2 Environmental Features

4.2.2.1 Meteorological Features

WorldClim BIO Variables V1 dataset can easily be accessed from the GEE cloud computing platform. The dataset is instantly available for all users. These variables are derived from monthly climate data. They are directly used as features for the classifier algorithms with no pre-processing required. Figure 4.2 and Figure 4.3 illustrate the variabilities of BIO1 (annual mean temperature) and BIO12 (annual precipitation) over the entire study area, respectively.

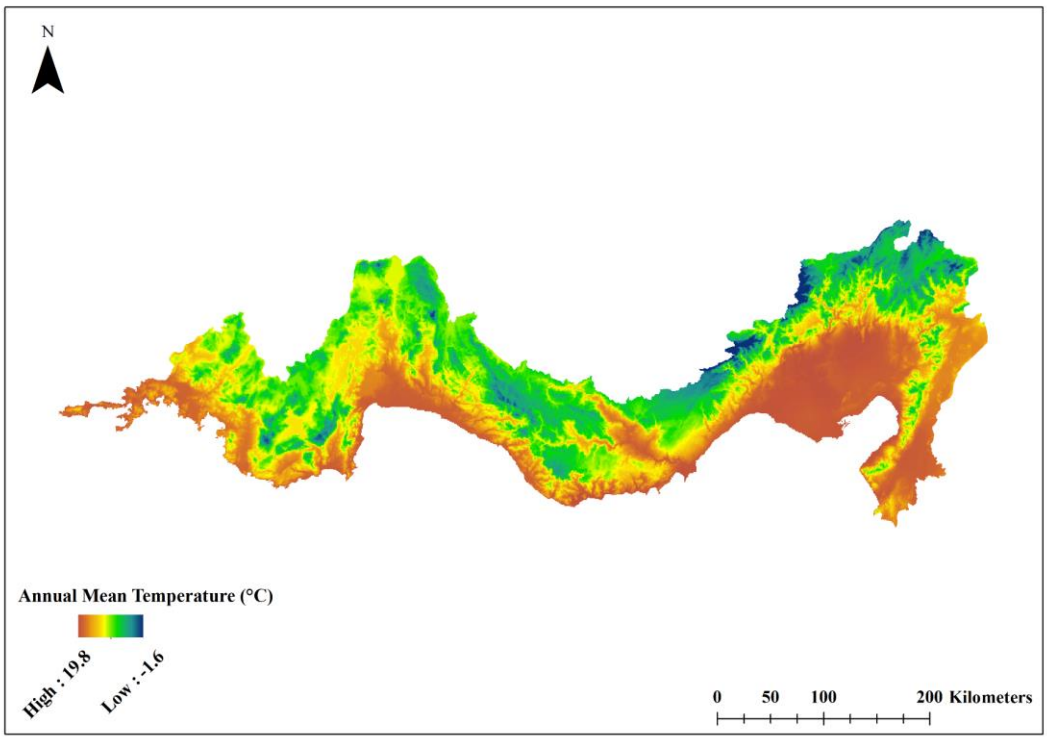

Figure 4.2. Annual mean temperature (BIO1) of the study area.

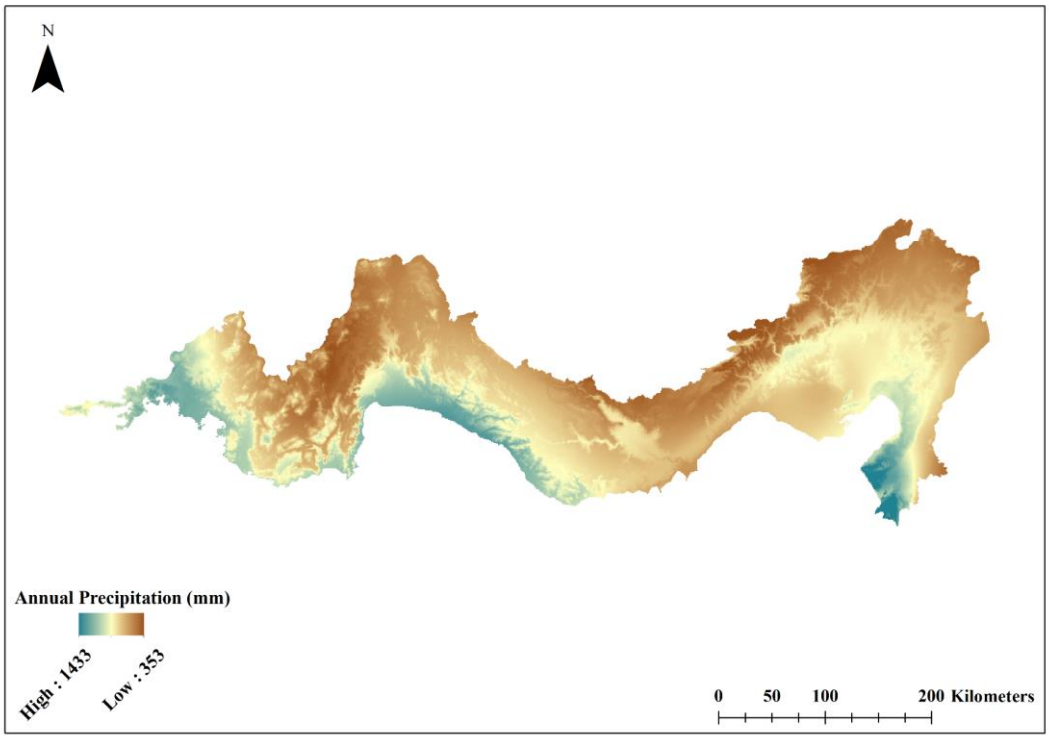

Figure 4.3. Annual precipitation (BIO12) of the study area.

4.2.2.2 Topographical Features

SRTM Digital Elevation Version 4 dataset (Jarvis et al., 2008) provides elevation data for the DEM feature. This dataset is available on GEE cloud computing platform. Figure 4.4 - Figure 4.24 show the elevation distributions of each class. Histograms showing elevation distribution of *Cercis siliquastrum* and *Vitex agnus-castus* are not plotted as only one sample polygon exists in each class. These aforementioned classes are found to have an elevation of 1160 m and 200 m, respectively. Note that the given distributions do not necessarily reflect the actual distributions of the alliances, because they are affected by the sampling. Nevertheless, they give an idea about the actual distributions.

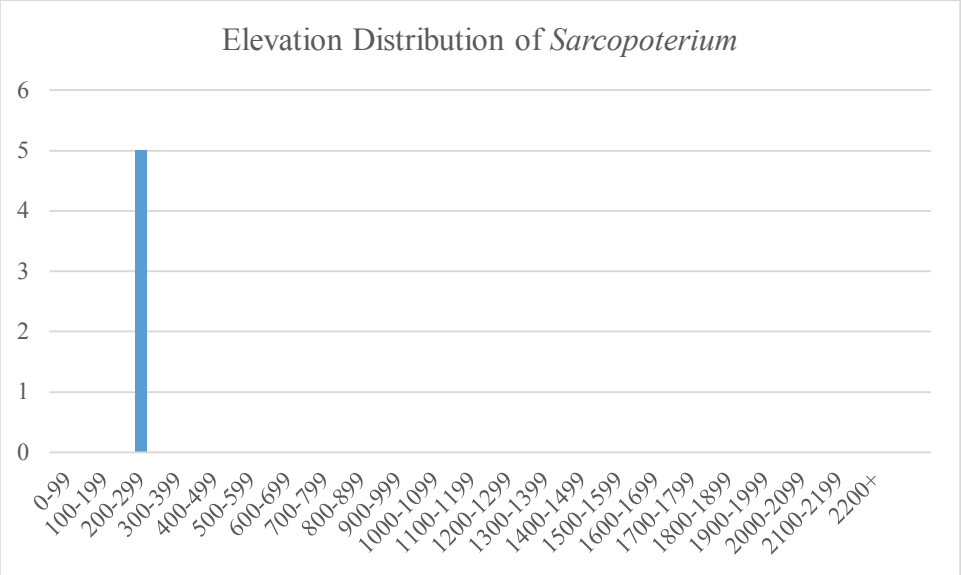

Figure 4.4. Histogram showing elevation (m) distribution of *Sarcopoterium*.

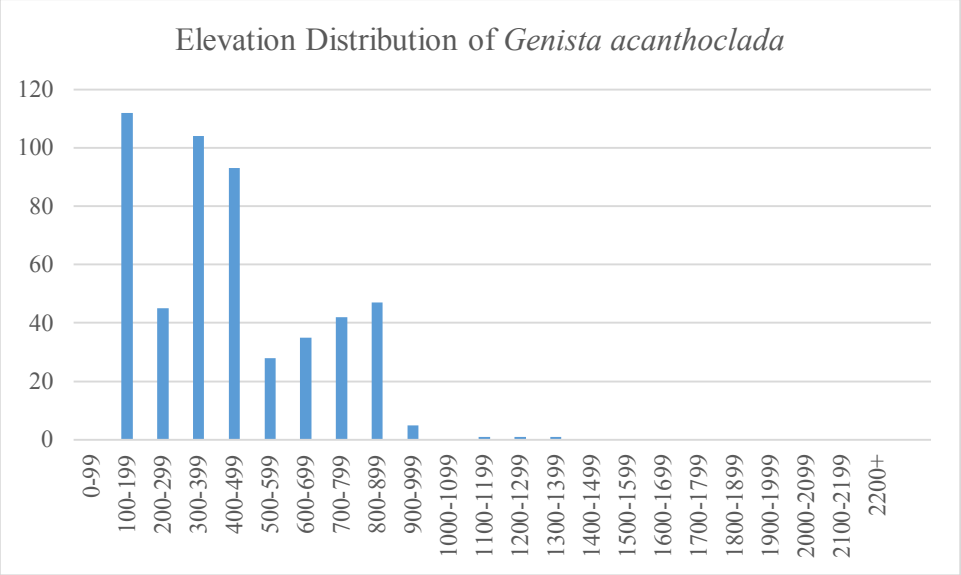

Figure 4.5. Histogram showing elevation (m) distribution of *Genista acanthoclada*.

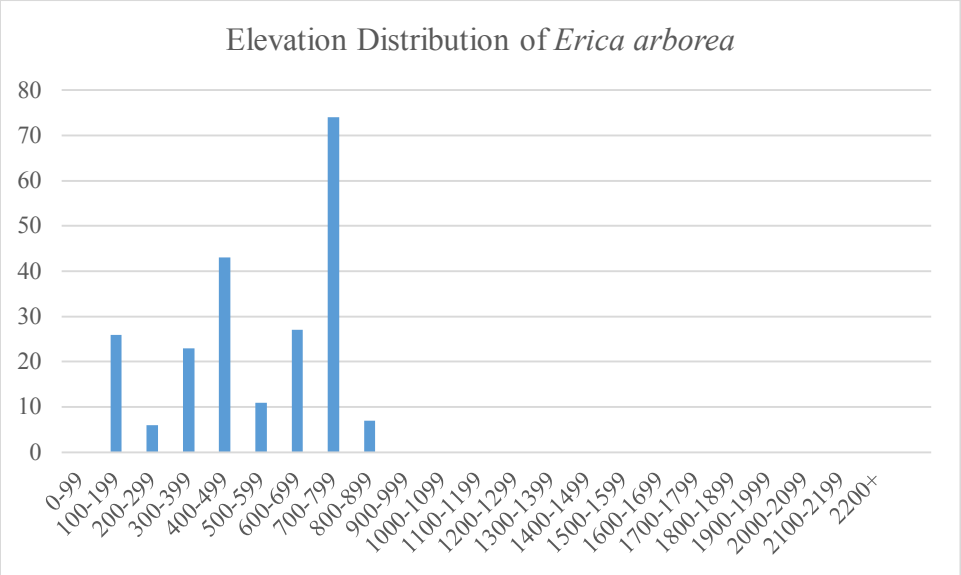

Figure 4.6. Histogram showing elevation (m) distribution of *Erica arborea*.

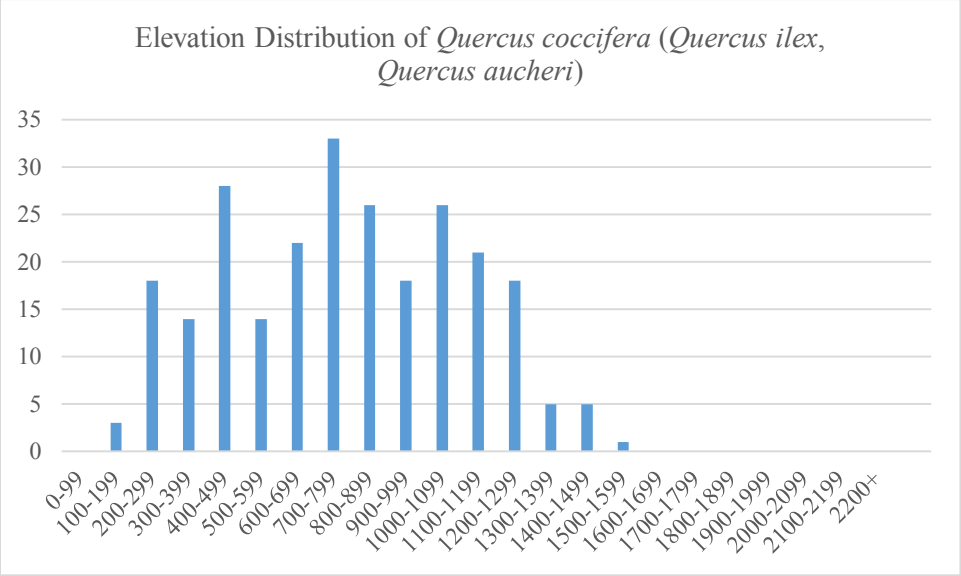

Figure 4.7. Histogram showing elevation (m) distribution of *Quercus coccifera* (*Quercus ilex*, *Quercus aucheri*).

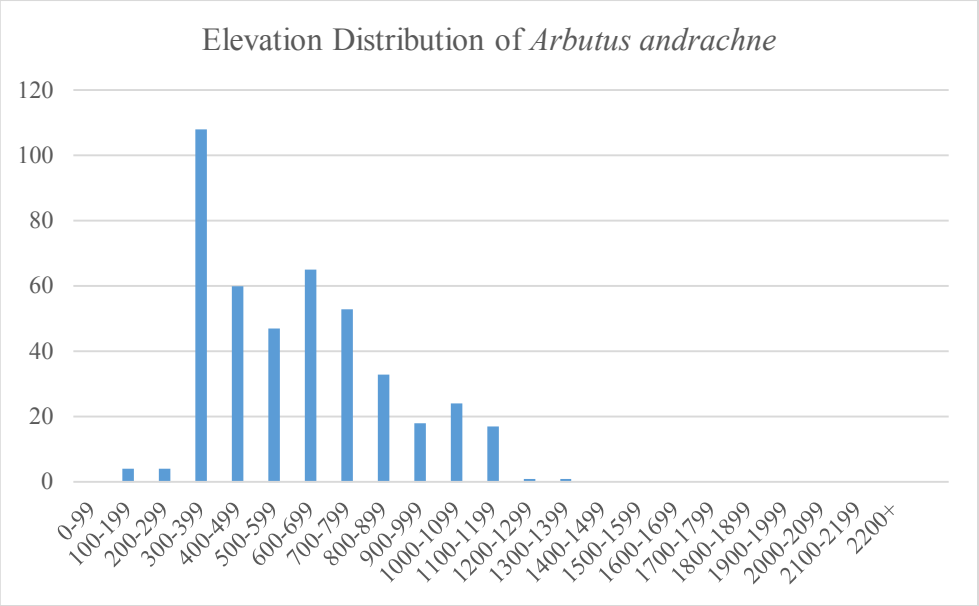

Figure 4.8. Histogram showing elevation (m) distribution of *Arbutus andrachne*.

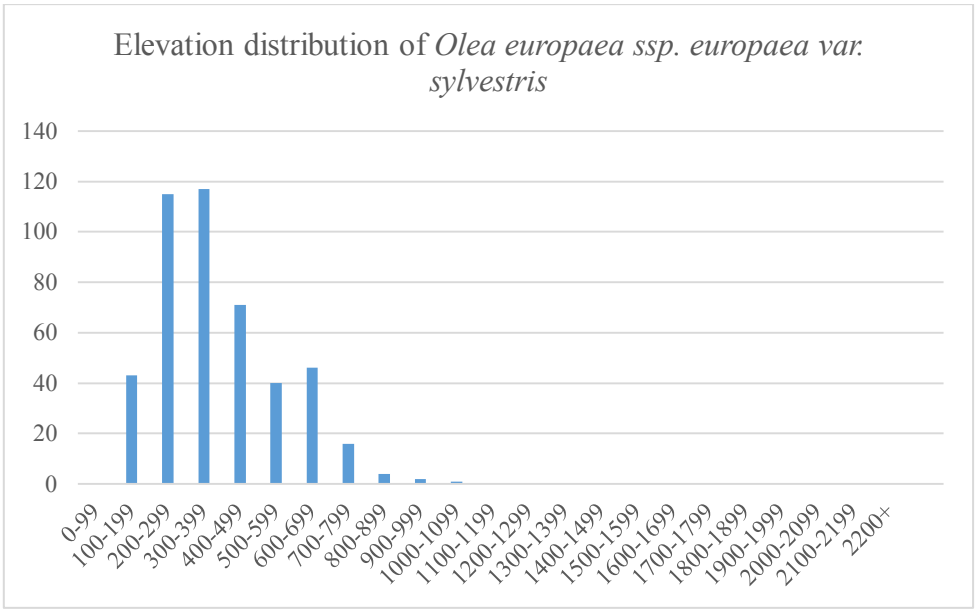

Figure 4.9. Histogram showing elevation (m) distribution of *Olea europaea ssp. europaea var. sylvestris*.

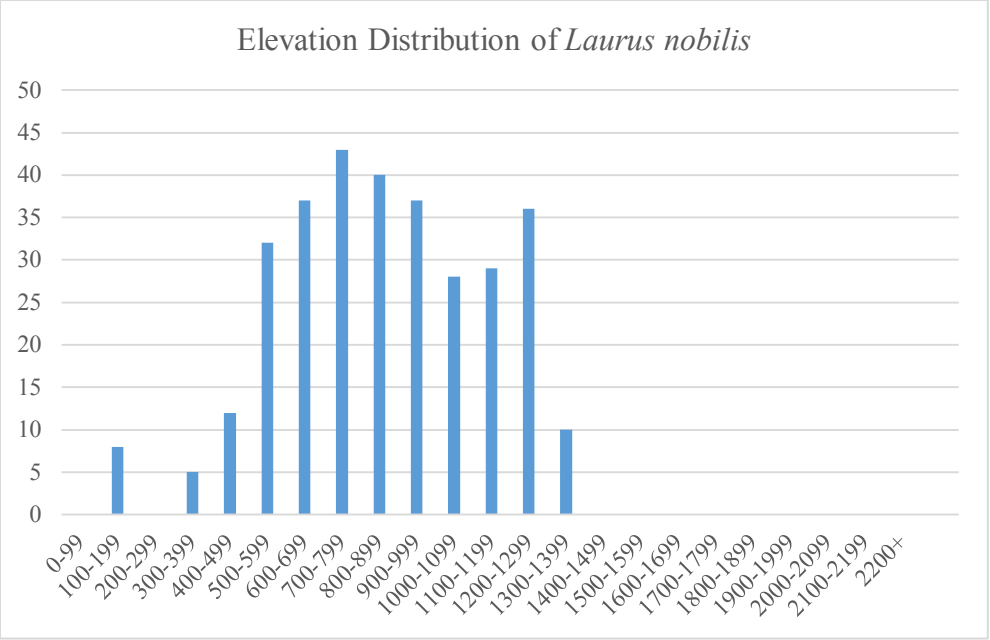

Figure 4.10. Histogram showing elevation (m) distribution of *Laurus nobilis*.

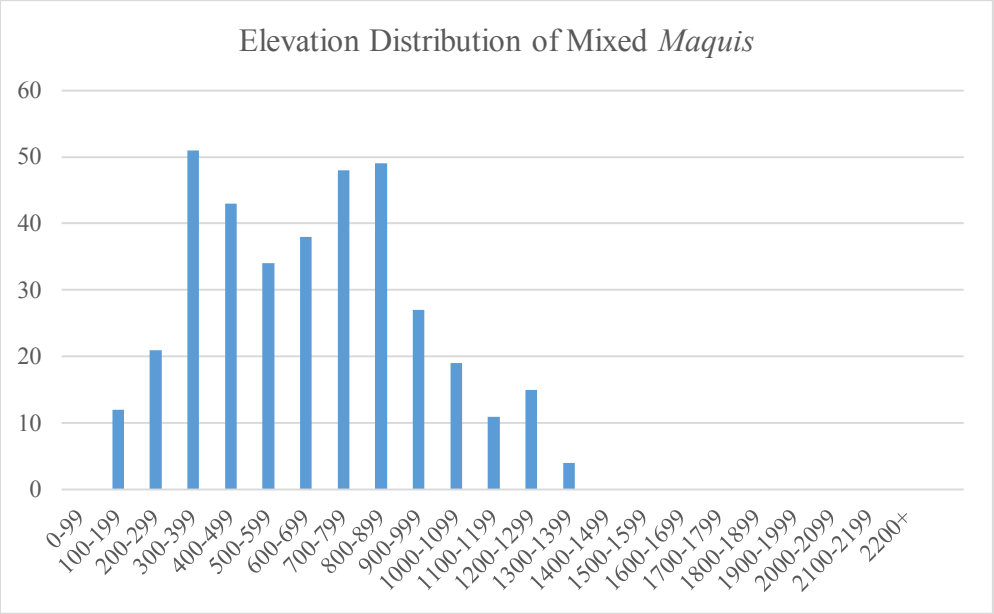

Figure 4.11. Histogram showing elevation (m) distribution of Mixed *Maquis*.

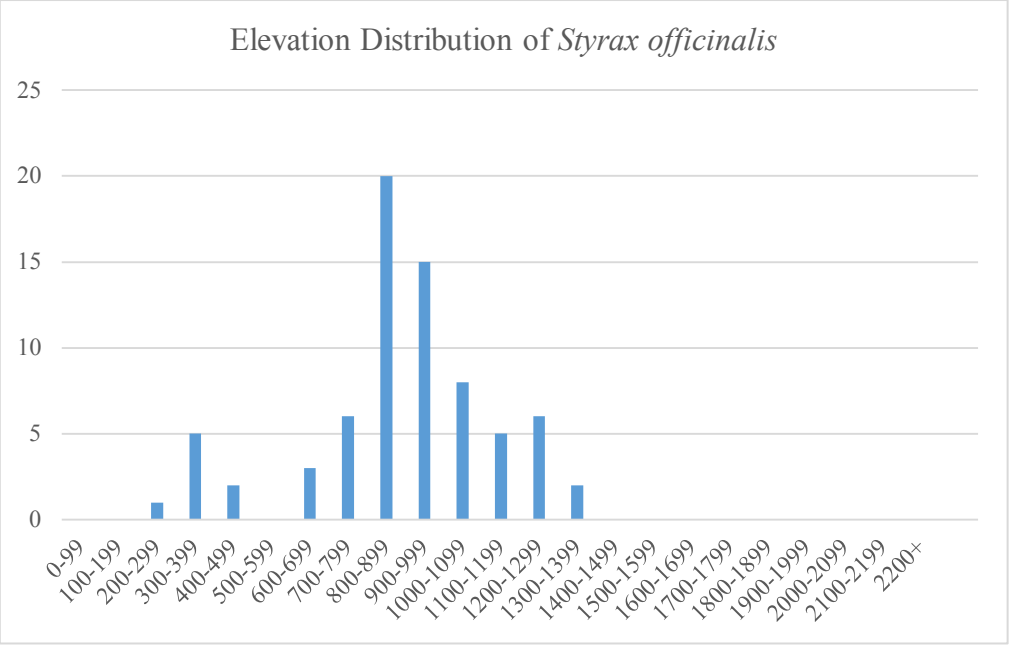

Figure 4.12. Histogram showing elevation (m) distribution of *Styrax officinalis*.

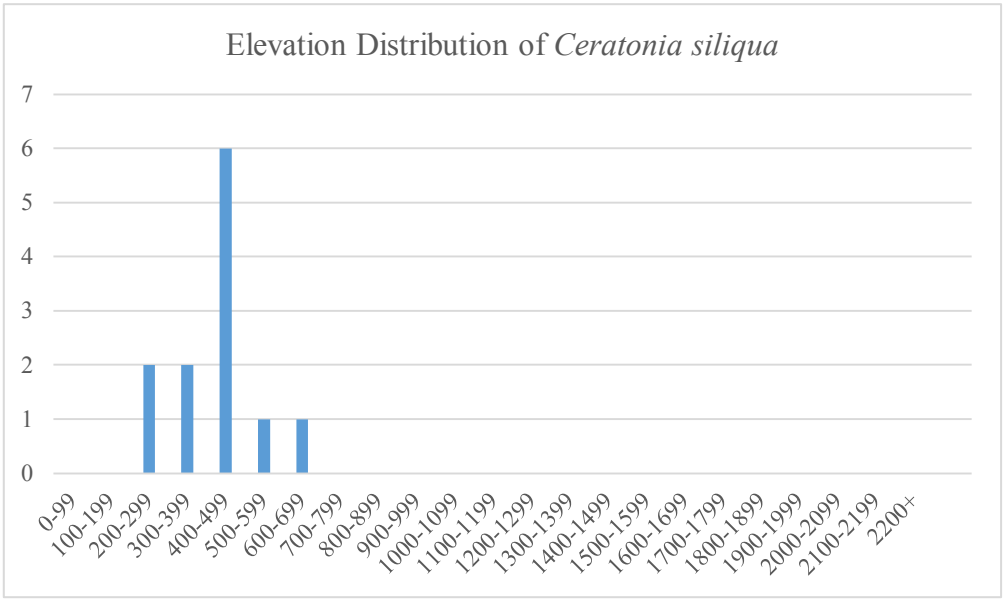

Figure 4.13. Histogram showing elevation (m) distribution of *Ceratonia siliqua*.

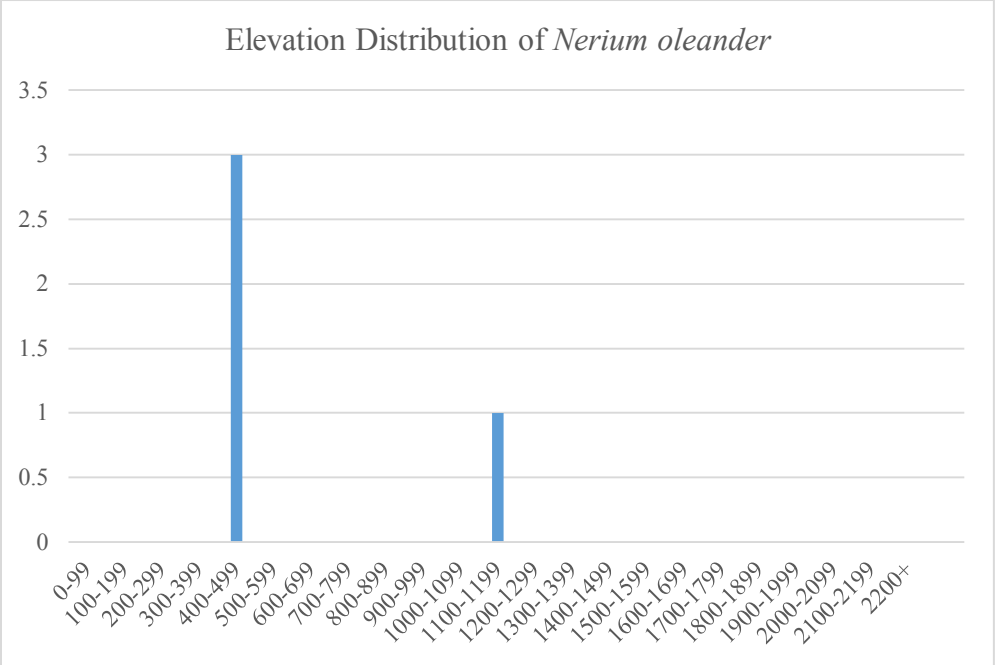

Figure 4.14. Histogram showing elevation (m) distribution of *Nerium oleander*.

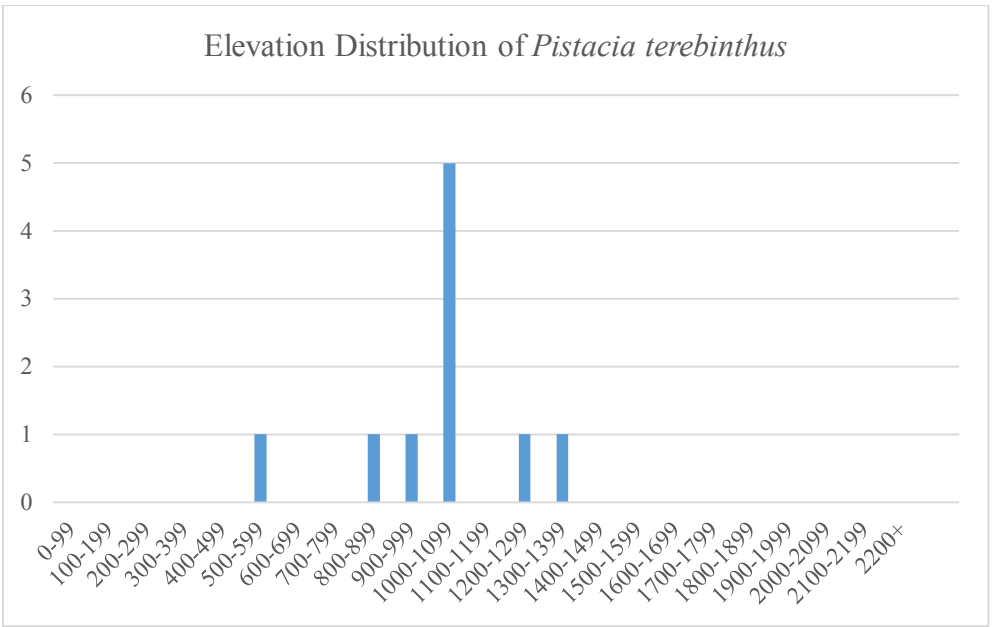

Figure 4.15. Histogram showing elevation (m) distribution of *Pistacia terebinthus*.

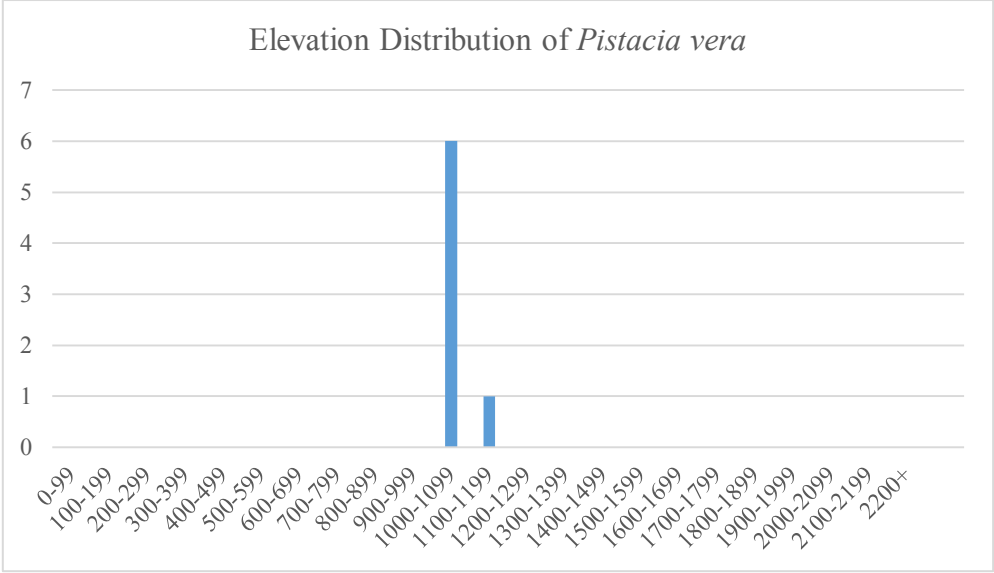

Figure 4.16. Histogram showing elevation (m) distribution of *Pistacia vera*.

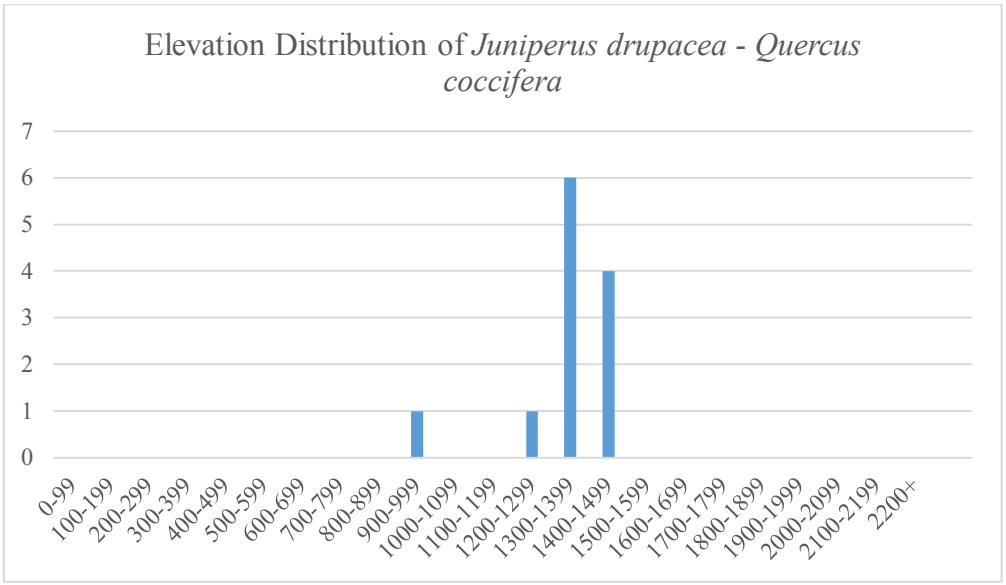

Figure 4.17. Histogram showing elevation (m) distribution of *Juniperus drupacea* - *Quercus coccifera*.

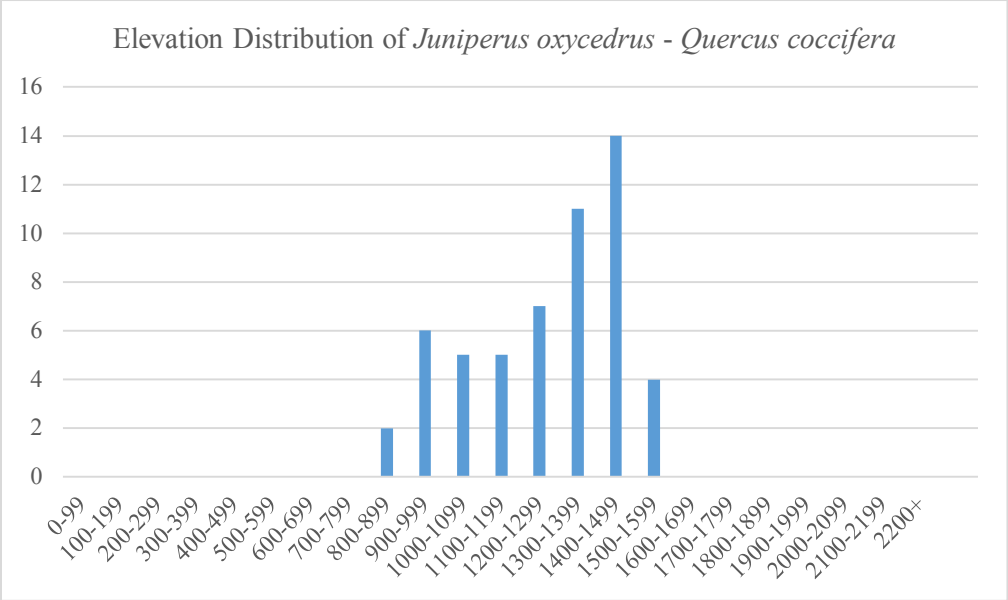

Figure 4.18. Histogram showing elevation (m) distribution of *Juniperus oxycedrus* - *Quercus coccifera*.

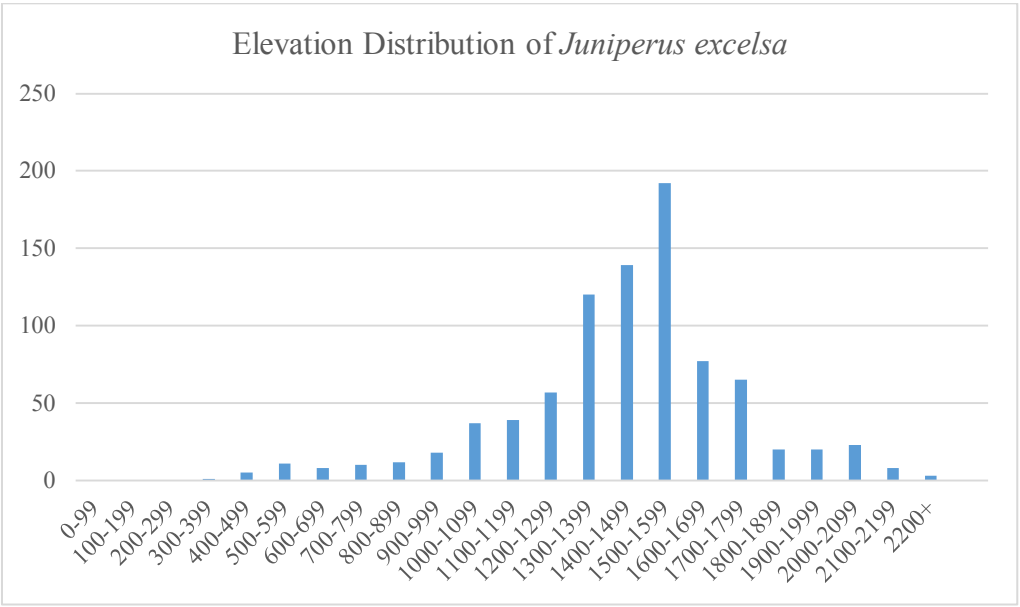

Figure 4.19. Histogram showing elevation (m) distribution of *Juniperus excelsa*.

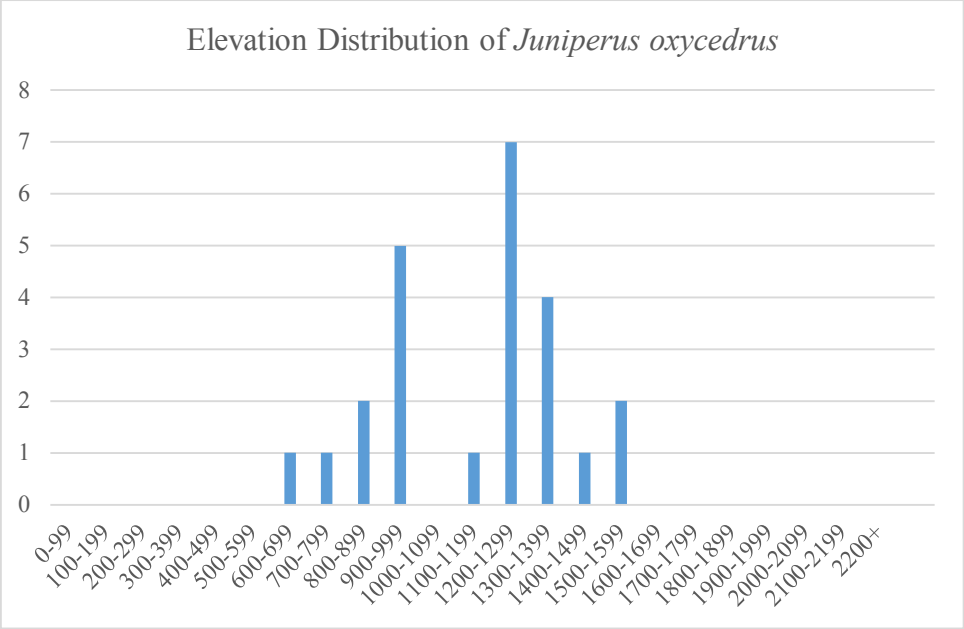

Figure 4.20. Histogram showing elevation (m) distribution of *Juniperus oxycedrus*.

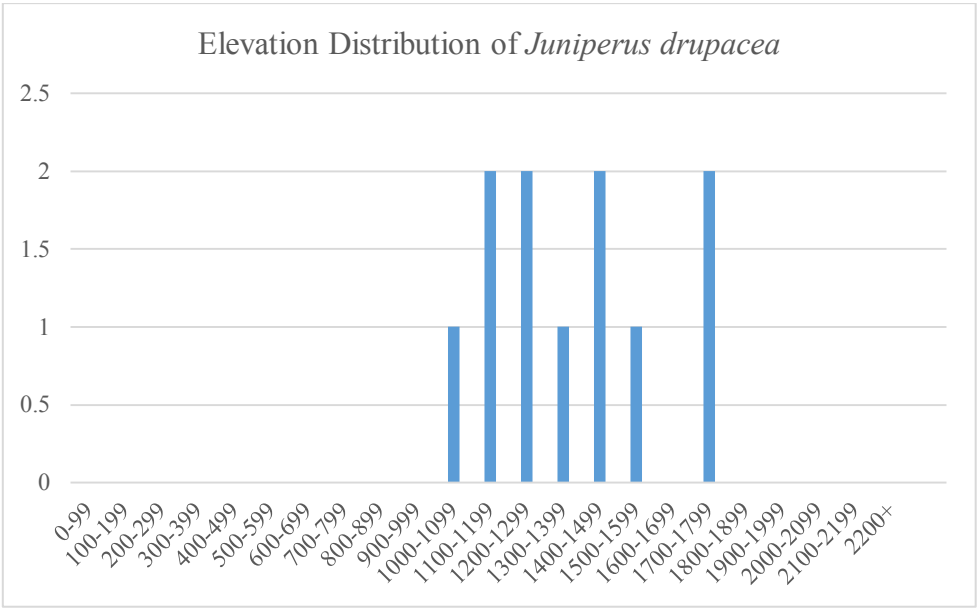

Figure 4.21. Histogram showing elevation (m) distribution of *Juniperus drupacea*.

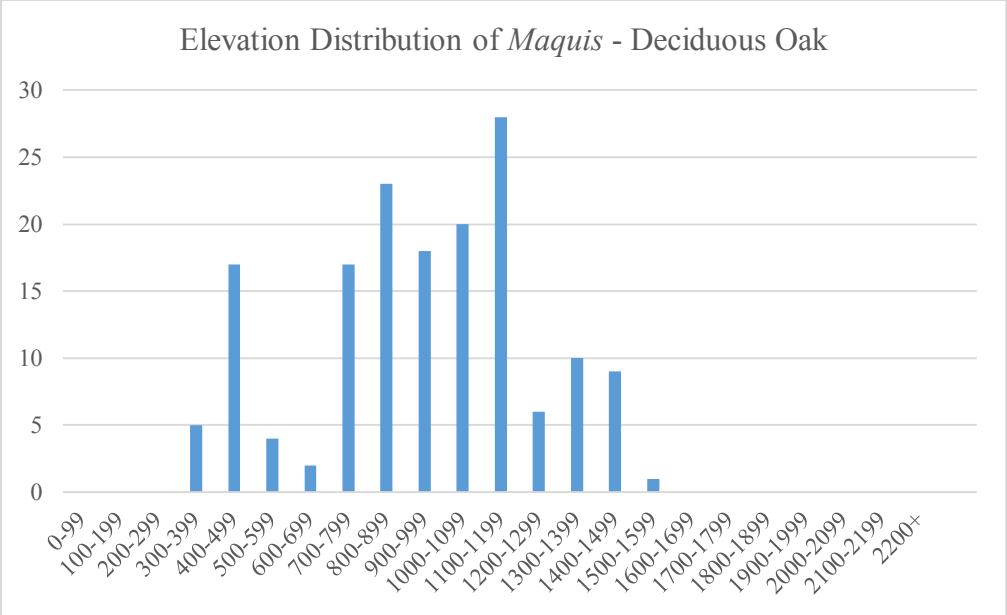

Figure 4.22. Histogram showing elevation (m) distribution of *Maquis* - Deciduous Oak.

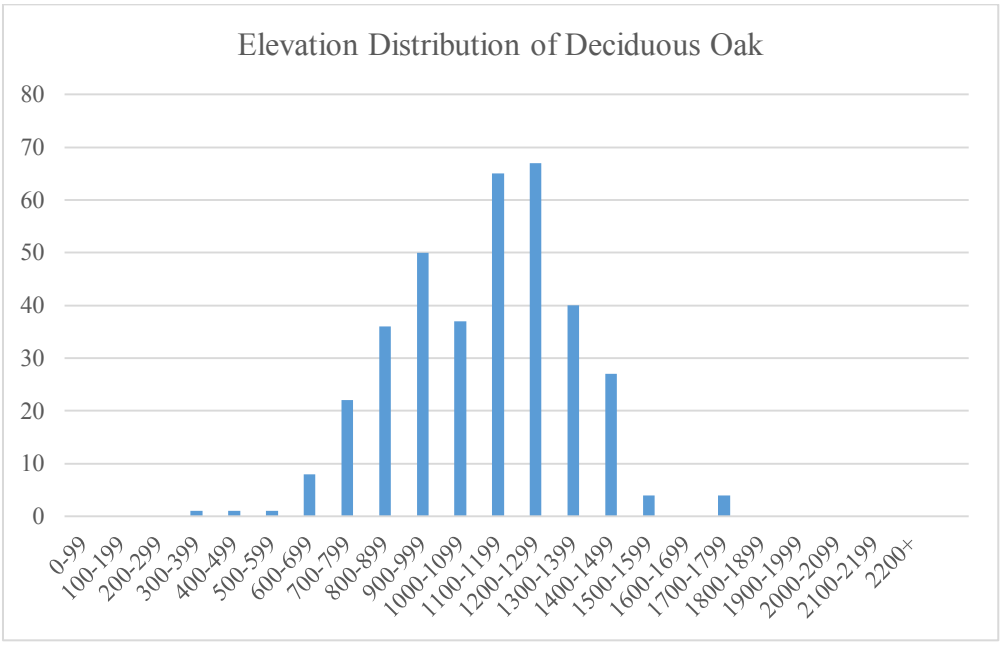

Figure 4.23. Histogram showing elevation (m) distribution of Deciduous Oak.

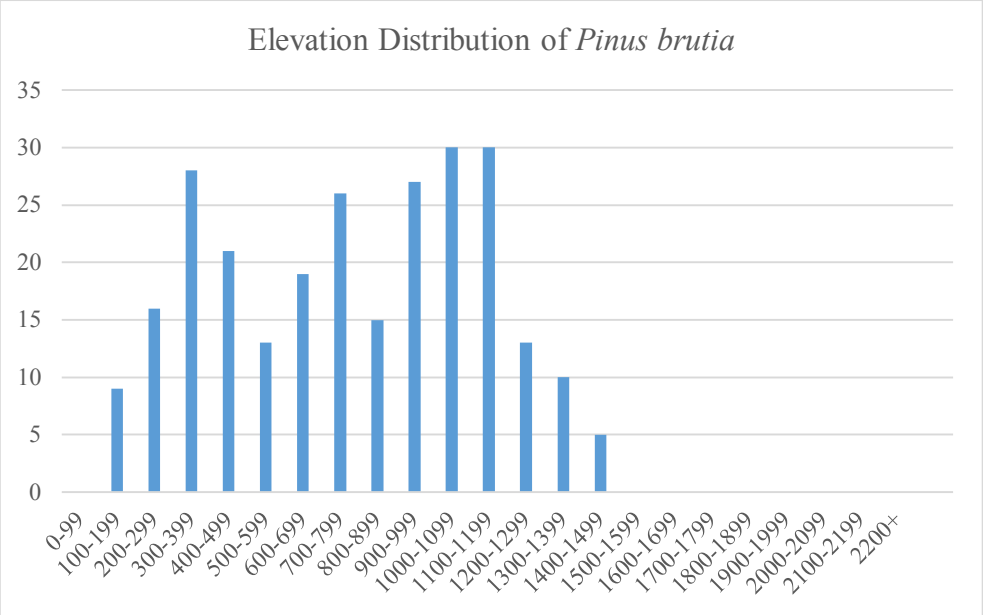

Figure 4.24. Histogram showing elevation (m) distribution of *Pinus brutia*.

The DEM, as shown in Figure 4.25, is used to extract slope and surface curvature. Slope calculations of the entire study area were done via GEE. Figure 4.26 shows the variability of the slope in the study area.

In order to generate the surface curvature of the study area, the DEM raster of the study area was exported from GEE and imported into ArcGIS software. The surface curvature was calculated in ArcGIS using the planform curvature tool from the Spatial Analyst toolbox. The curvature tool calculates the second derivative value of the DEM surface on a cell-by-cell basis. The planform curvature, which is related to the convergence and divergence of flow across a surface, is perpendicular to the direction of the maximum slope. A positive value indicates that the surface is laterally convex, a negative value indicates the surface is laterally concave, while zero indicates linearity of the surface (ESRI, 2020). Diagram illustrating the planform curvature is shown in Figure 4.27.

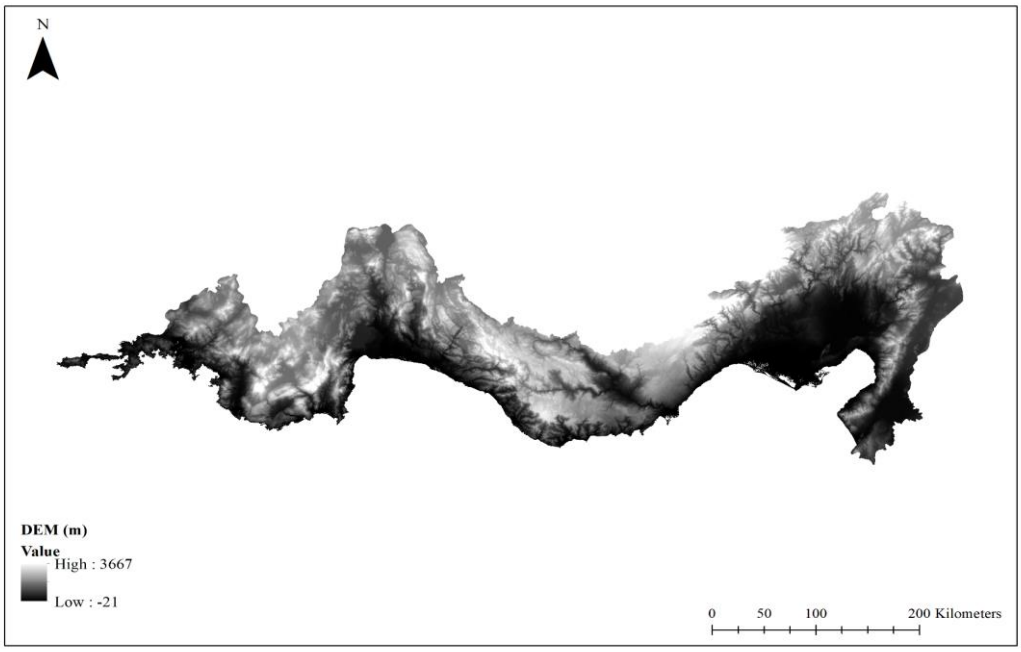

Figure 4.25. Digital Elevation Model of the study area.

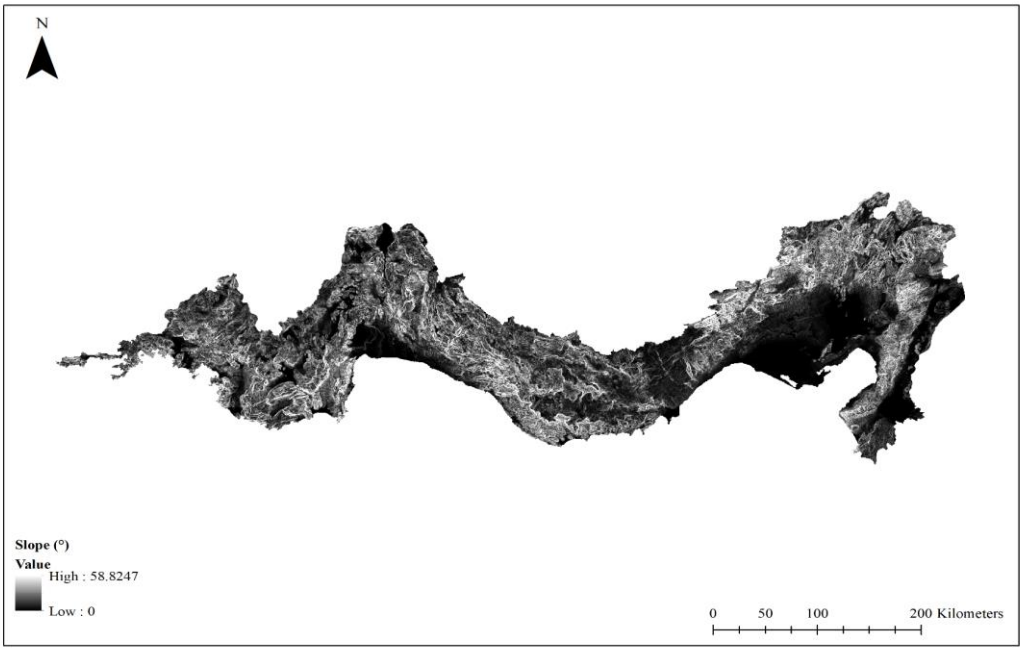

Figure 4.26. Slope variations throughout the study area.

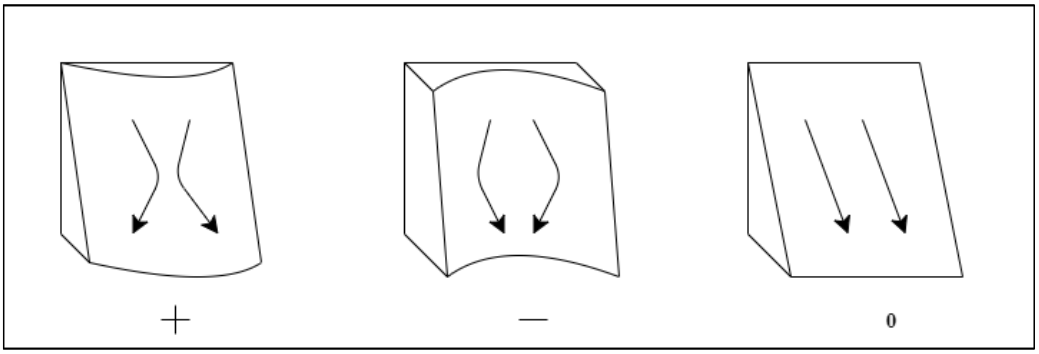

Figure 4.27. Illustration of the planform curvature.

Furthermore, the distances between each GT polygon to the nearest streams and basin borders, or ridges, are also calculated as ancillary features. These two additional features are referred to as “distance to streams” and “distance to ridges”, respectively as shown in Figure 4.28 and Figure 4.30. WWF HydroSHEDS (Lehner et al., 2008), which is readily accessible within the GEE platform, provides the dataset required to calculate these distances. WWF HydroSHEDS Free Flowing Rivers Network v1 (Lehner & Grill, 2013) dataset presents polylines that represent river networks based on 15 arc-seconds resolution raster data while WWF HydroSHEDS Basins level 12 (Lehner & Grill, 2013) dataset provides polygons of nested, hierarchical watersheds based on 15 arc-seconds resolution raster data. These features may be helpful in classification of alliances that prefer to grow in the valleys or along the ridges.

The datasets were filtered to only confine the study area and then exported from GEE and imported into ArcGIS. Distance to streams and distance to ridges were calculated in ArcGIS using the Euclidean Distance tool from the ArcToolbox Spatial Analyst Tools. The Euclidian distance measured distance from every cell to the nearest streams and basin borders or ridges.

Figure 4.29 and Figure 4.31 show the streamlines and the watershed basins overlaying the DEM, respectively.

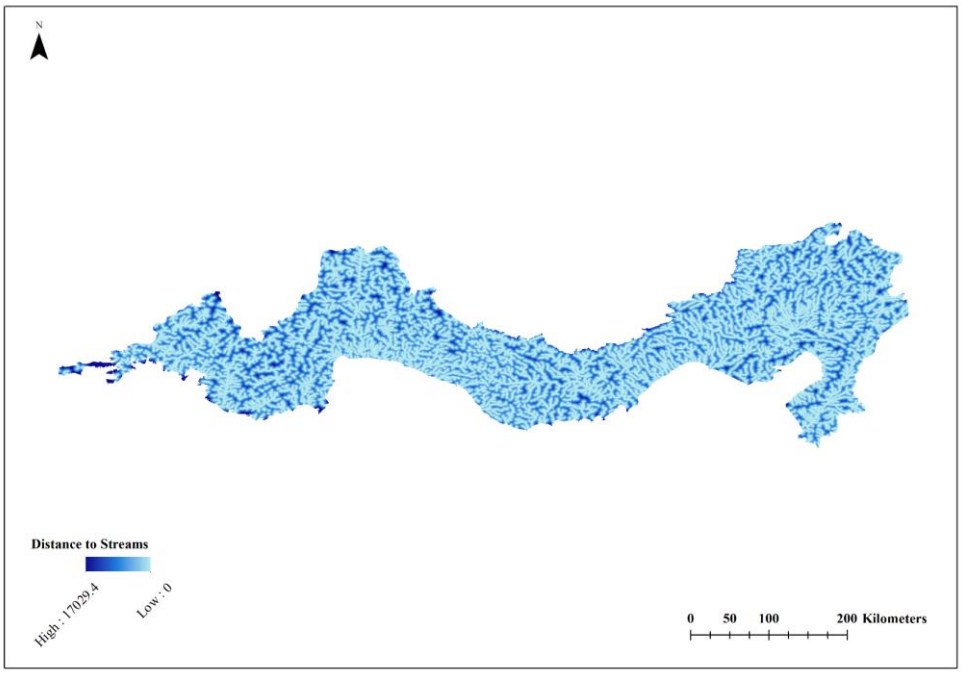

Figure 4.28. Distance to Streams feature.

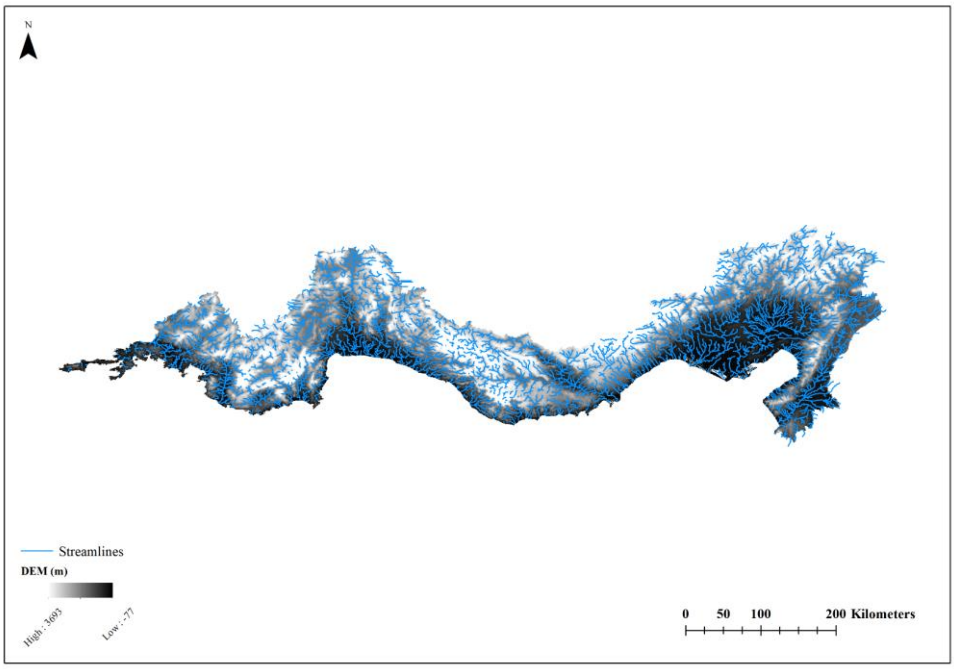

Figure 4.29. Streamlines overlaying the DEM.

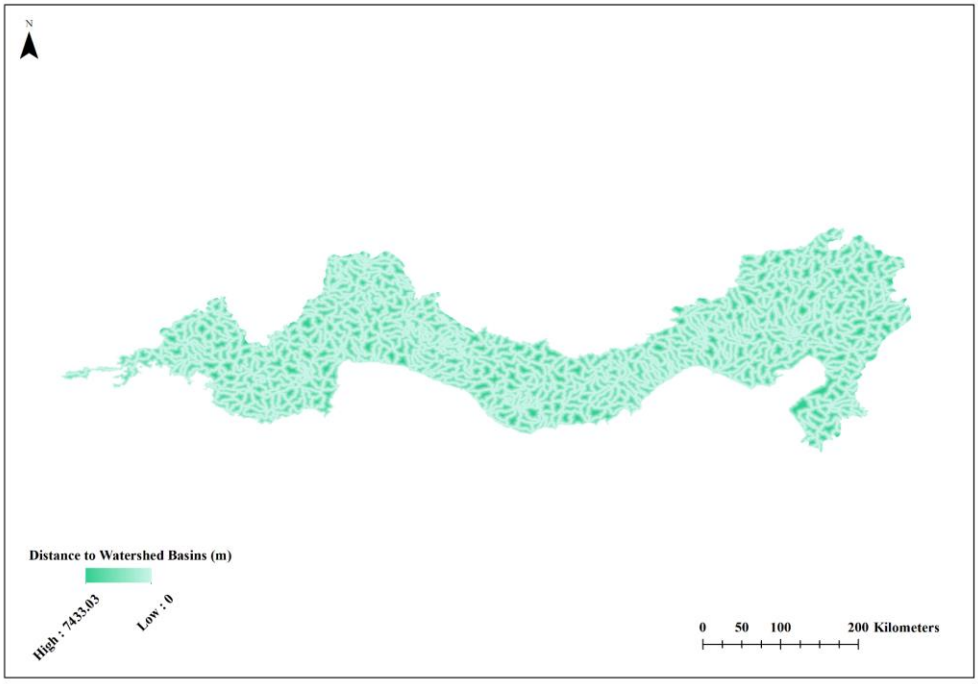

Figure 4.30. Distance to Ridges feature.

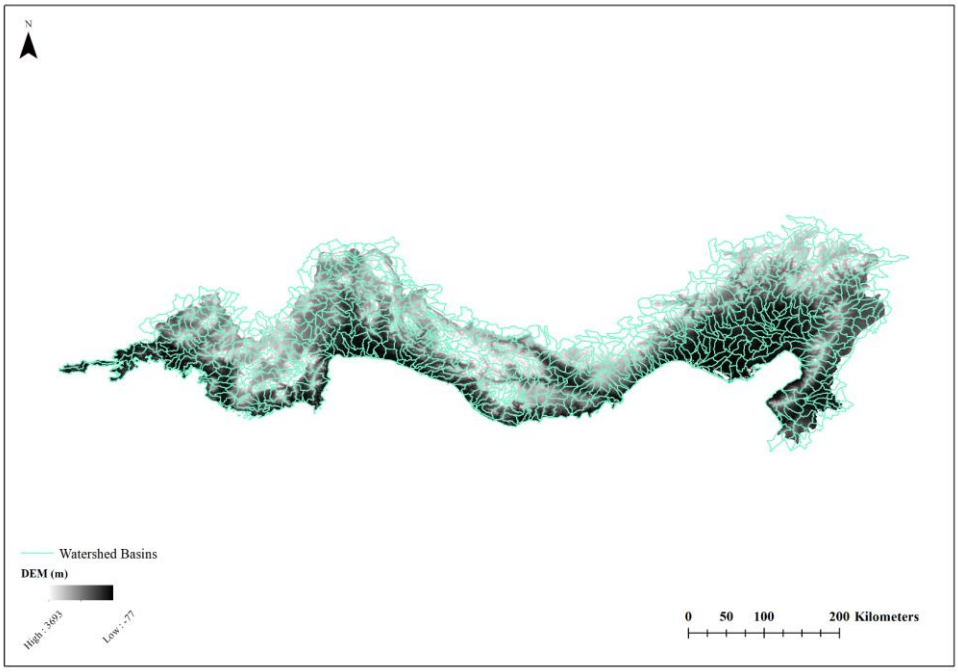

Figure 4.31. Watershed Basins overlaying the DEM.

4.3 Classification

The classification scheme is divided into three different parts: the first part is classification using only remotely-sensed features, the second part is classification using only environmental features, which involves meteorological and topographical features, and the third part is classification using all of the derived features combined, namely the environmental features in addition to the remotely-sensed features. The same sample points and cross-validation method were implemented for all three classification schemes.

4.3.1 Random Forest (RF)

The classification was initially performed using the Random Forest (RF) classifier (Breiman, 2001). RF is a robust and relatively quick machine learning algorithm (Pelletier et al., 2016). It is composed of multiple decision trees, which makes it resistant to overfittings. RF has the ability to recognize and analyze non-intuitive relationships, and has the flexibility required to handle complex, high-dimensional interactions (Evans et al., 2011). The RF algorithm is also known to be able to handle class imbalance within reasonable limits and is robust to outliers.

The RF algorithm was performed using both the matrix laboratory (MATLAB) programming platform as well as GEE. Their Overall Accuracies (OA) and Cohen's kappa values were then compared. Classification done on the GEE platform is vital in order to generate large scale maps of the classified areas labeled as maquis at alliance-level, which will be beneficial for understanding the distribution of forest and maquis.

The RF classification was implemented with tuning parameters that had been set to default values. The minimum number of observations per tree leaf was set to 1, and the number of features to select at random for each decision split (*mtry*) was set as

the square root of the total number of features for classification. The number of trees (*N*) was set to 150. The RF tuning parameters do not have significant effects on the overall classification accuracy, with only as much as 1% difference variation observed between the best and the worst parameter arrangements (Pelletier et al., 2016).

Importance of each feature is calculated as the increase in prediction error if the values of that feature are permuted across the out-of-bag observations. This measure is computed for every tree, then averaged over the entire ensemble and divided by the standard deviation over the entire ensemble.

4.3.2 Support Vector Machine (SVM)

In addition to RF, classification using Support Vector Machine (SVM) was also performed. SVM are supervised non-parametric learning models that can be implemented for classification as well as regression. In the context of this thesis, SVM was implemented for classification task. As SVM is non-parametric, no assumption was made on the underlying data distribution. The SVM training algorithm targets to find a hyperplane that splits the dataset into a predefined number of classes. The decision boundary obtained in the training step that minimizes misclassifications is known as the optimal separation hyperplane (Mountrakis et al., 2011). The simplest form of a hyperplane is a linear hyperplane that separates a given test sample into two possible classes. However, remote sensing data generally cannot be separated linearly due to their complexities. In such cases, a kernel can be used in order to map the data into a non-linear dimension to ease separation between classes.

The SVM algorithm was performed in MATLAB. The classification was implemented using MATLAB's 'fitceoc' function, with 'Coding' design chosen as 'onevsone' (for each binary learner, one class is positive, another is negative, and the software ignores the rest. This design exhausts all combinations of class pair

assignments), 'Learners' as 'svm', and hyperparameters optimization as 'none'. This function fits multiclass models for SVM and returns a trained error-correcting output codes (ECOC) model.

The overall accuracy and Cohen's kappa value are computed for comparison against the other machine learning algorithms implemented in this study.

4.3.3 Quadratic Discriminant Analysis (QDA)

In addition to RF and SVM, classification using Quadratic Discriminant Analysis (QDA) was also performed. QDA is a multi-class classifier that has a quadratic decision surface. QDA has no hyperparameters to tune. QDA was implemented using the 'fitdiscr' function on MATLAB. The 'DiscrimType' is set as 'quadratic', and 'ScoreTransform' is set as 'logit' ($1/(1 + e^{-x})$).

The overall accuracy and Cohen's kappa value from QDA are also computed for comparison against the other machine learning algorithms implemented in this study.

4.4 Feature Selection

A total of 118 remote sensing and ancillary features were computed, some of which might be highly correlated with others. In order to optimize the feature space, choosing the most competent features in relation to the dataset and eliminating highly correlated features are essential. RFE was applied to achieve this.

RFE, thoroughly explained in (Gregorutti et al., 2017), which has also been implemented by (Cheng & Wang, 2019 and Jiang et al., 2004), is a method that requires an updating of the permutation importance measures at each step of the algorithm. By applying RFE, features with least importance were eliminated. This results in variable rankings that are ultimately consistent with their use in the current

forest and features that contribute indispensably to the model. The RFE algorithm implemented in this study is done as follows (Gregorutti et al., 2017):

1. A RF is trained.
2. The predictor feature importance is computed.
3. Less relevant feature(s) are eliminated.
4. Steps 1 to 3 are repeated until no further features remained.

At Step 3 of the RFE mentioned above, the features that are eliminated at each loop are the features with the lowest importance measures. The exact number of features eliminated for each classification scheme vary as shown in Table 4.3 and Table 4.4.

For classification done using only remotely-sensed features, a total of 95 features were derived (i.e., 54 features for six vegetation indices (i.e., NDVI, NDWI, SAVI, EVI, GVI, and GDVI) calculated for all the months (except winter months: December, January, and February), 24 coefficients derived from cubic polynomials fitted on the surface of all the VIs, nine coefficients inferred from the spectro-temporal patterns (STP), and eight additional newly computed spectro-temporal indices). Number of features remained at each RFE for the remotely-sensed feature classification scheme is listed in Table 4.3.

Table 4.3. Number of remotely-sensed features at each RFE.

95	**80**	**65**	**50**	**45**	**40**	**35**	**32**	**29**	**26**	**23**	**20**	**17**	**16**	**15**	**14**	**13**	**12**	**11**	**10**	**5**	**1**

For the second classification scheme, which is classification done using only environmental features, a total of 23 features were derived. Two features were eliminated by RFE. Eliminating more features actually decreased the Overall Accuracy (OA).

The last classification scheme combined all remotely-sensed features with all environmental features. A total of 118 features were computed. Number of features remained at each RFE for the combined classification scheme is listed in Table 4.4.

Table 4.4. Number of combined features at each RFE.

118	**101**	**81**	**61**	**46**	**31**	**26**	**21**	**18**	**15**	**13**	**11**	**9**	**7**	**5**	**3**	**2**	**1**

4.5 Accuracy Assessment

In order to produce unbiased classification results, a 5-fold cross-validation was implemented to evaluate the RF and other classification models. The training and evaluation of the models were carried out in MATLAB and GEE. The OA and Cohen's kappa values were calculated for each classification scheme.

CHAPTER 5

RESULTS

5.1 Introduction

The results obtained throughout this study are summarized in this chapter. The ontology of the classes is presented in Section 5.2 and the classes and features used in the initial classification are presented in Section 5.3. Section 5.4 illustrates the features selection steps and presents the results for all three classification schemes. Section 5.5 presents the classes and features used in the final classification. Section 5.6 illustrates the classification maps produced. Section 5.7 presents the results of the classification accuracies for all three classification schemes.

5.2 The Ontology

The GT data originally contained 23 different alliances with varying number of polygons in each class, as listed in Table 5.1. Details of all the alliances along with their corresponding photographs can be found in Appendix A. The alliances with samples less than 10 polygons were eliminated from the samples set (i.e., *Sarcopoterium*, *Cercis siliquastrum*, *Nerium oleander*, *Pistacia vera*, and *Vitex agnus-castus*). There was extreme inequality between the number of polygons in each class, which is solely based on their rarity or abundances in the field. Since the RF algorithm does not perform well when there is class imbalance, the number of polygons of overly populated classes (e.g., *Quercus coccifera* (*Quercus ilex,*

Quercus aucheri) and mixed maquis) were randomly reduced in order to even out distribution of the number of training polygons in each class.

Table 5.1. List of all classes along with their corresponding number of polygons in the original GT data provided by DKM.

English Name	Latin	Number of Polygons
Prickly, spiny, or thorny burnet	*Sarcopoterium*	5
Spiny Broom (Brm)	*Genista acanthoclada*	525
Tree Heath (THt)	*Erica arborea*	216
Kermes oak (including other evergreen oak) (Kms)	*Quercus coccifera (Quercus ilex, Quercus aucheri)*	1692
Eastern strawberry tree (EST)	*Arbutus andrachne*	965
Wild olive (WOl)	*Olea europea ssp. europea var. sylvestris*	444
Bay, Laurel (Bay)	*Laurus nobilis*	376
Mixed Maquis (MxM)	*Mixed Maquis*	1053
Judas-tree	*Cercis siliquastrum*	1
Storax	*Styrax officinalis*	74
Carob	*Ceratonia siliqua*	12
Nerium or oleander	*Nerium oleander*	4
Turpentine tree or terebinth	*Pistacia terebinthus*	17
Pistachio	*Pistacia vera*	7
Chaste tree	*Vitex agnus-castus*	1
Syrian Juniper - Kermes oak (Jun)	*Juniperus drupacea - Quercus coccifera*	12
Prickly juniper - Kermes oak (Jun)	*Juniperus oxycedrus - Quercus coccifera*	54
Greek juniper (Jun)	*Juniperus excelsa*	886
Prickly juniper (Jun)	*Juniperus oxycedrus*	24
Syrian juniper (Jun)	*Juniperus drupacea*	11
Maquis - Deciduous oak (Maq-DOk)	*Maquis - Deciduous oak*	208
Deciduous oak (DOk)	*Deciduous oak*	564
Turkish Red Pines (TRP)	*Pinus brutia*	301

5.3 Initial Classification

All 23 classes mentioned in Section 5.2 were included in the initial classification and a total of 118 features consisting of remotely-sensed features as well as ancillary features, as explained in Section 0, were used as initial features. As mentioned in Section 4.3, the initial classification was performed using the RF algorithm with tuning parameters set as default values for classification.

The spectra and phenology of various juniper classes are very similar and the differences among them are within the range of intra-class variability, as shown in Figure 5.1 and Figure 5.2. The differences during the winter months are due to snow cover. As a result, *Juniperus drupacea* - *Quercus coccifera*, *Juniperus oxycedrus* - *Quercus coccifera, Juniperus excelsa, Juniperus oxycedrus*, and *Juniperus drupacea* were merged into one single class and referred to as *Juniperus spp.* for the rest of the classification. As shown in Figure 5.3, a considerable proportion of the junipers grow at high altitudes, so it is natural to see the effect of the snow during the winter months.

Styrax officinalis, *Ceratonia siliqua*, and *Pistacia terebinthus* were merged into the mixed maquis class. These alliances are difficult to find in the field. They do not usually form a dominant class and they have the tendency to grow as individual trees or small groups, which is also part of the reason why classifying maquis can be quite a challenging task.

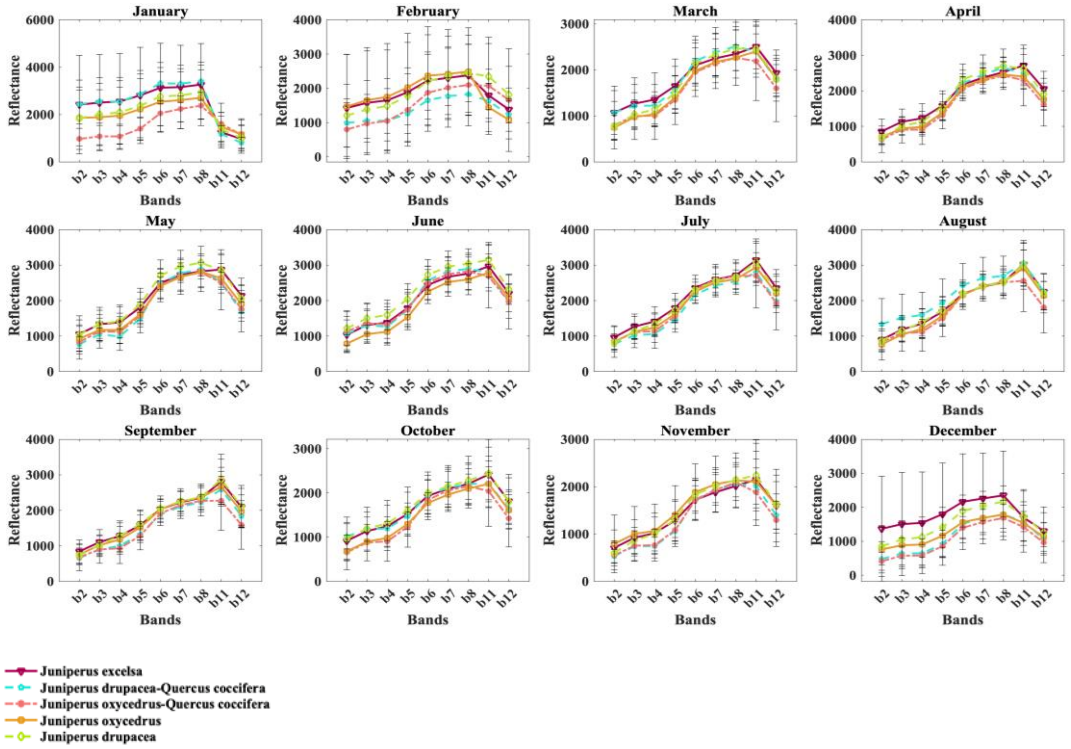

Figure 5.1. Spectral figures of all merged Juniper classes (*Juniperus spp.*) in each month with error bars for one standard deviation.

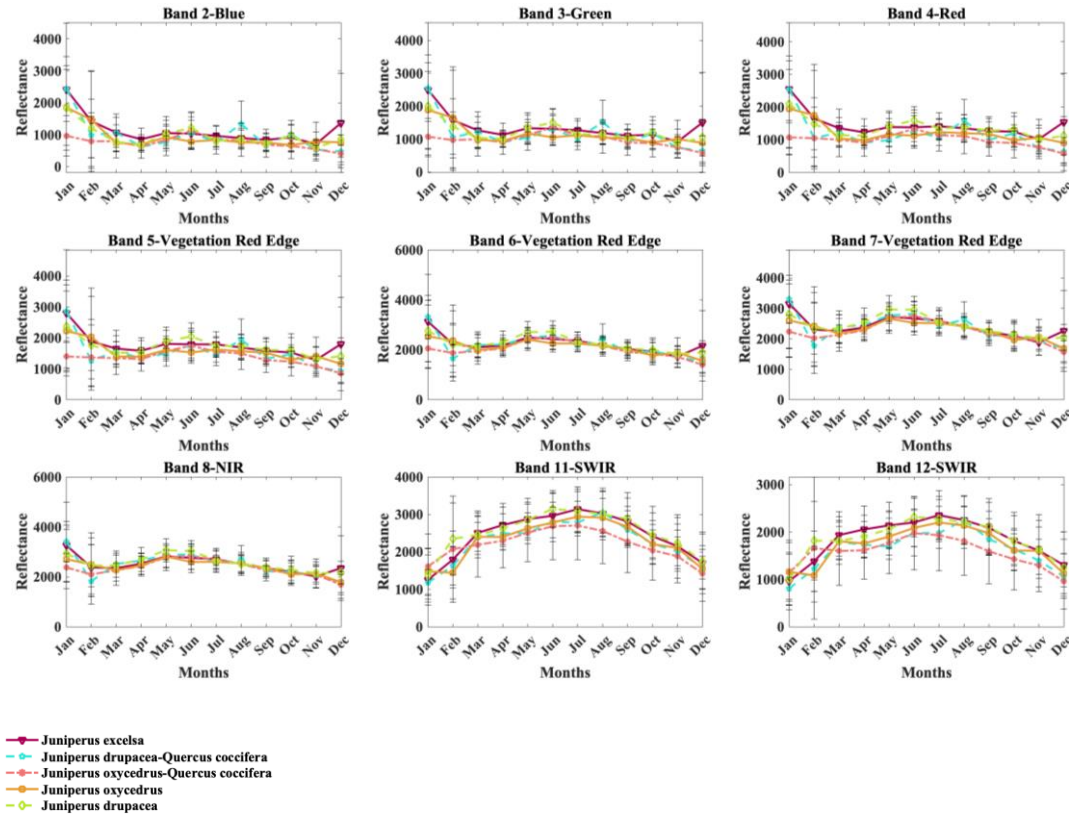

Figure 5.2. Temporal change of each band for all merged Juniper classes (*Juniperus spp.*) with error bars for one standard deviation.

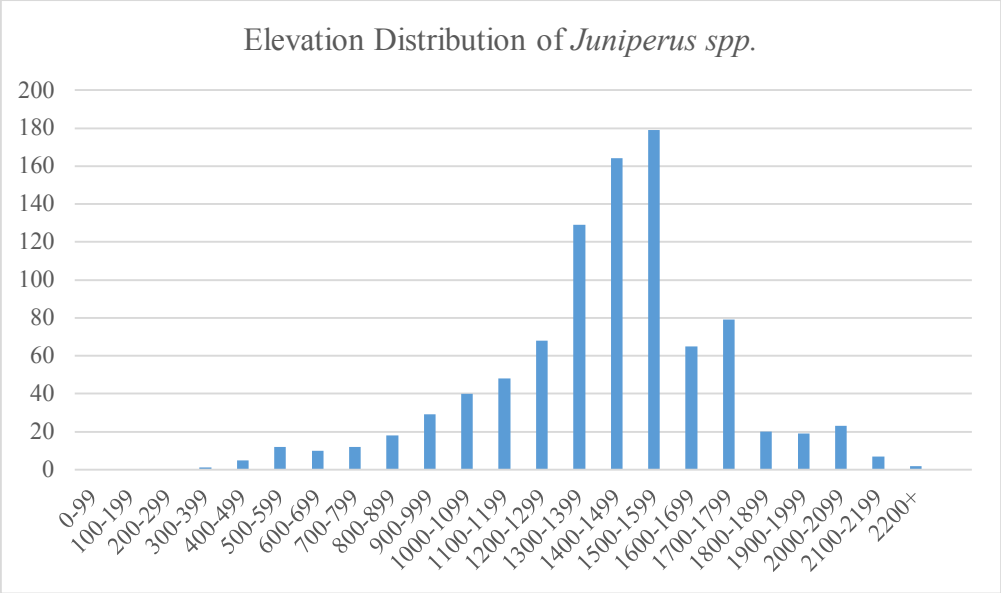

Figure 5.3. Histogram showing elevation (m) distribution of *Juniperus spp.*

5.4 Feature Selection

RFE is applied in order to assess the performance of all potential features. For all three classification schemes, the RF model is run 10 times with different seed values and the results are then averaged in order to even out the variations in the performance induced by the random nature of the RF algorithm (Gregorutti et al., 2017).

5.4.1 Remotely-Sensed Features

Figure 5.4 shows how the reduction of remotely-sensed features contribute to the RF classification accuracy. The peak point is illustrated in the curve in order to make a distinction for the highly important features. The peak point is marked after the first 32 features, which highlights that the first 32 features are highly important. These 32 features are listed in Table 5.2.

Table 5.2. Peak remotely sensed features.

Feature7	Normalized Summer-Winter NDVI
STP1	April NDWI
NDWIf1	STP2
STP3	June GVI
NDWIf2	October NDWI
GDVIf2	April SAVI
NDWIf3	September GVI
Feature1	STP7
May GVI	November NDWI
Feature6	STP4
April GVI	July GVI
March GVI	Feature4
STP8	Feature5
October GVI	SAVIf1
May NDWI	GVIf2
November GVI	GVIf4

Using more than 32 features does not significantly help in increasing the overall accuracy as illustrated in Figure 5.4 below.

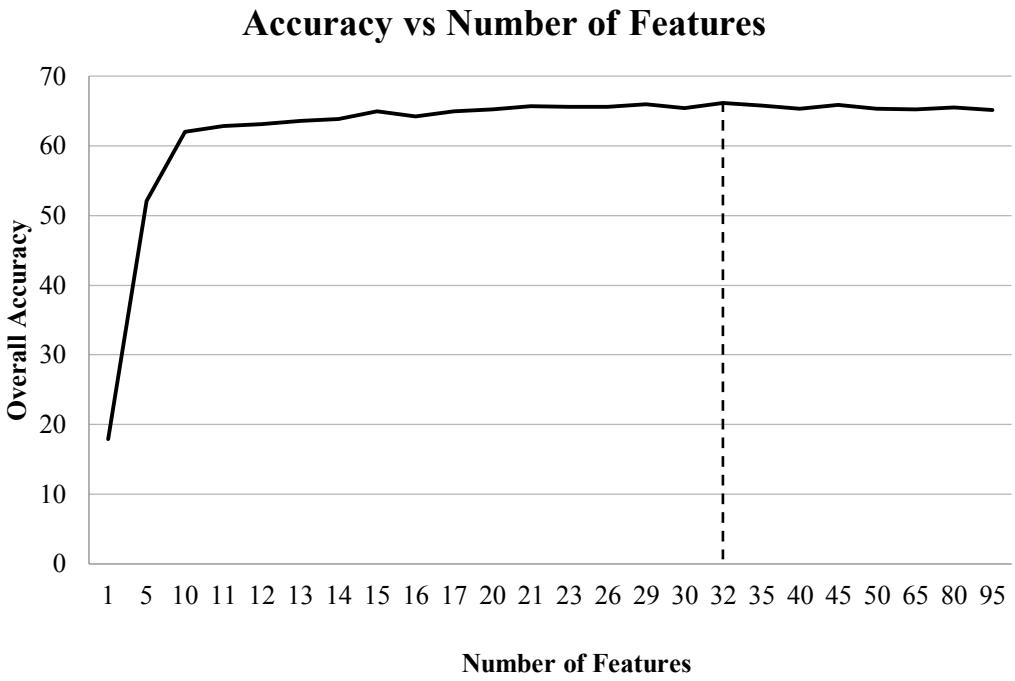

Figure 5.4. Overall Accuracy plotted against number of remotely-sensed features.

Figure 5.5 - Figure 5.16 show the behavior of the spectral signatures of each class in each month. In December, January, and February we can observe the effects of snow cover on alliances that generally grow at higher altitudes (e.g., *Juniperus spp.*). Their spectral signatures closely resemble each other, making it challenging for the classifier algorithm to make a clear distinction between each class, even between indisputable alliances like evergreen (e.g., *Pinus brutia*) and deciduous (e.g., Deciduous oak).

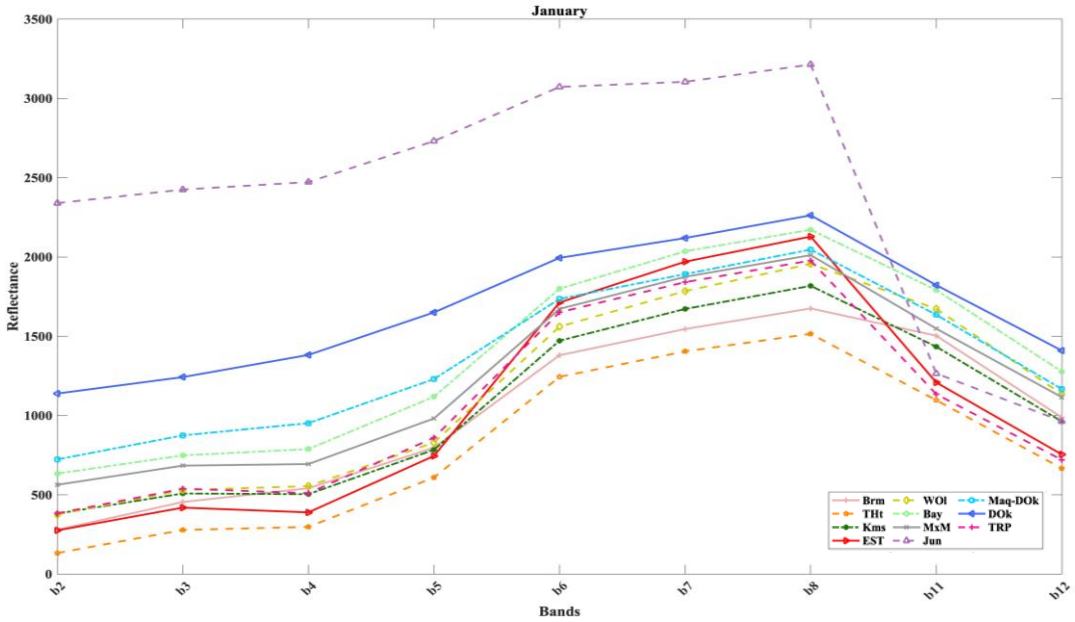

Figure 5.5. Spectral signatures of the classes in January.

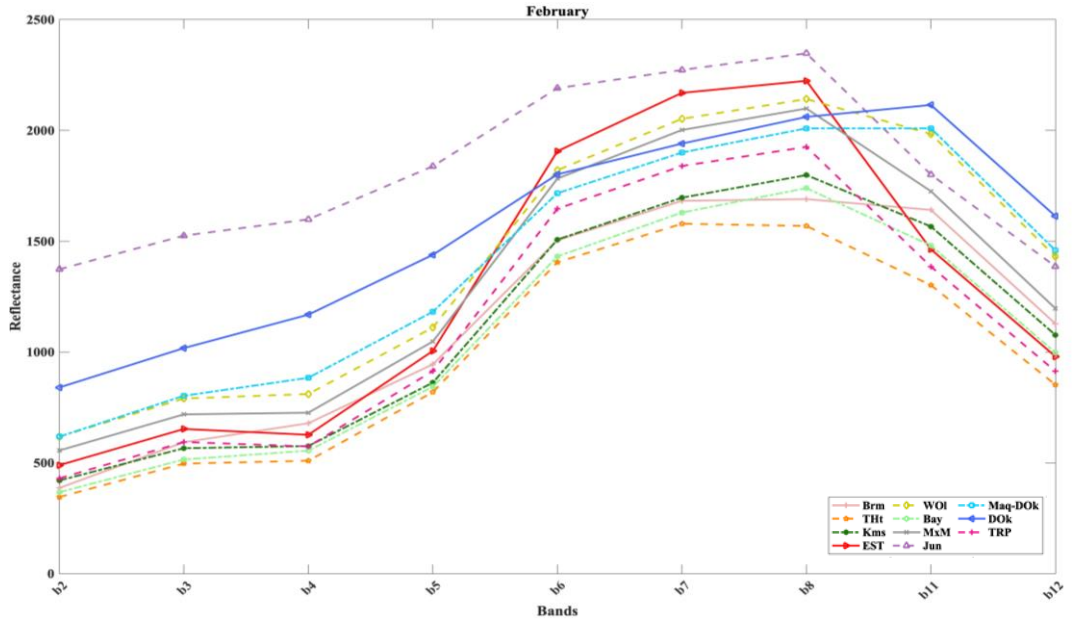

Figure 5.6. Spectral signatures of the classes in February.

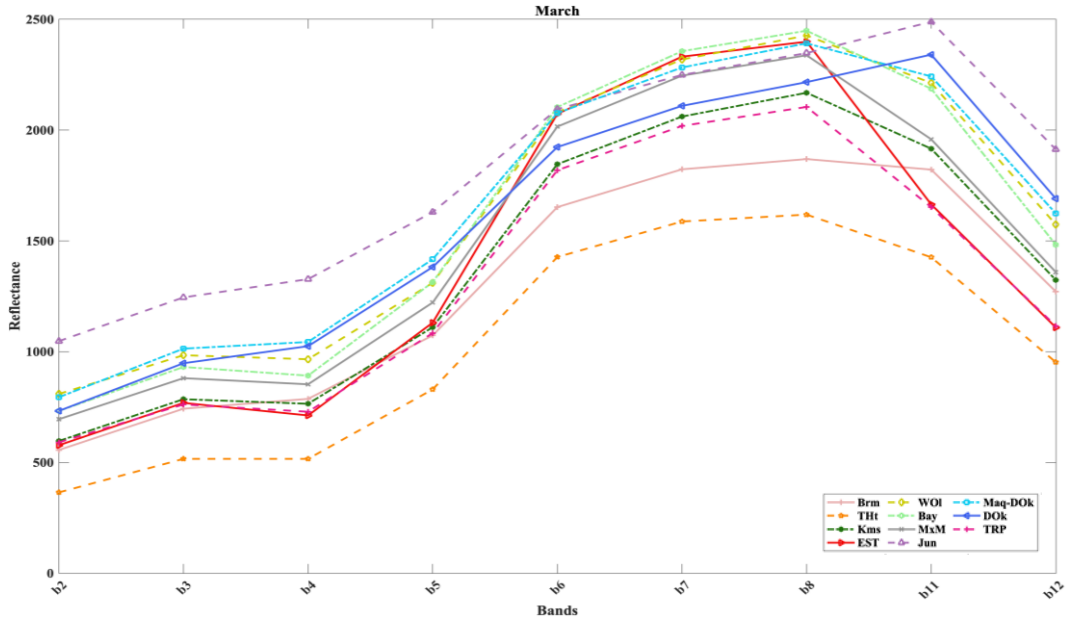

Figure 5.7. Spectral signatures of the classes in March.

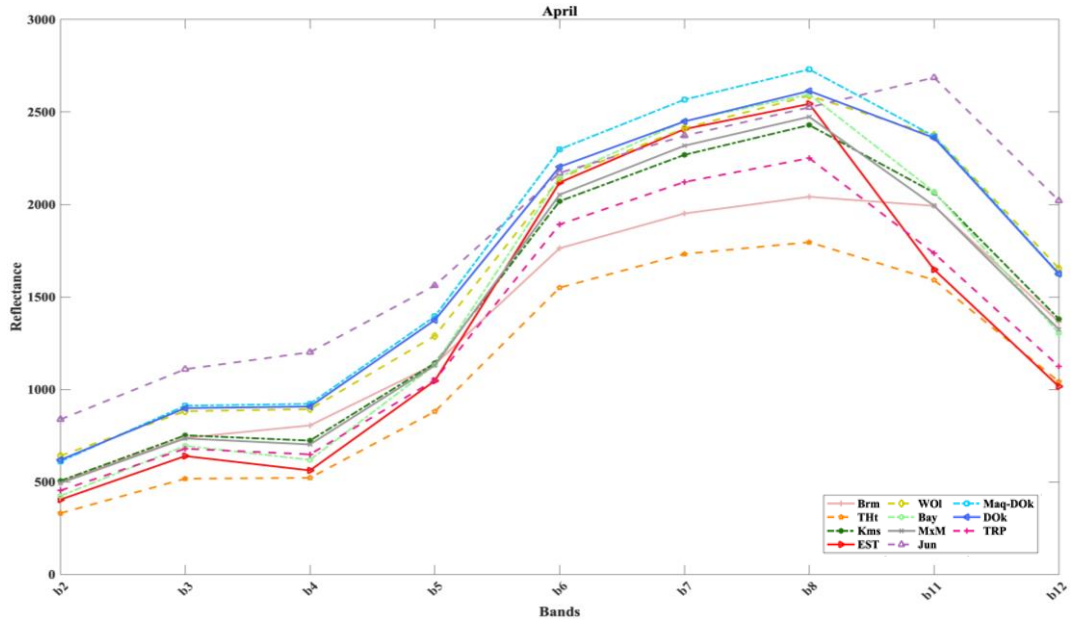

Figure 5.8. Spectral signatures of the classes in April.

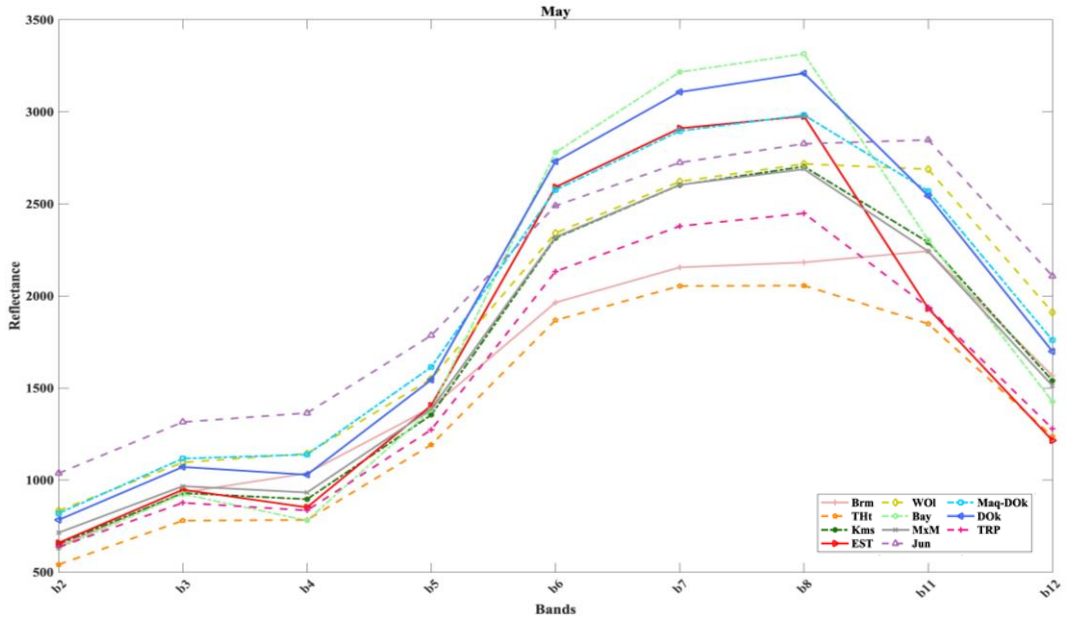

Figure 5.9. Spectral signatures of the classes in May.

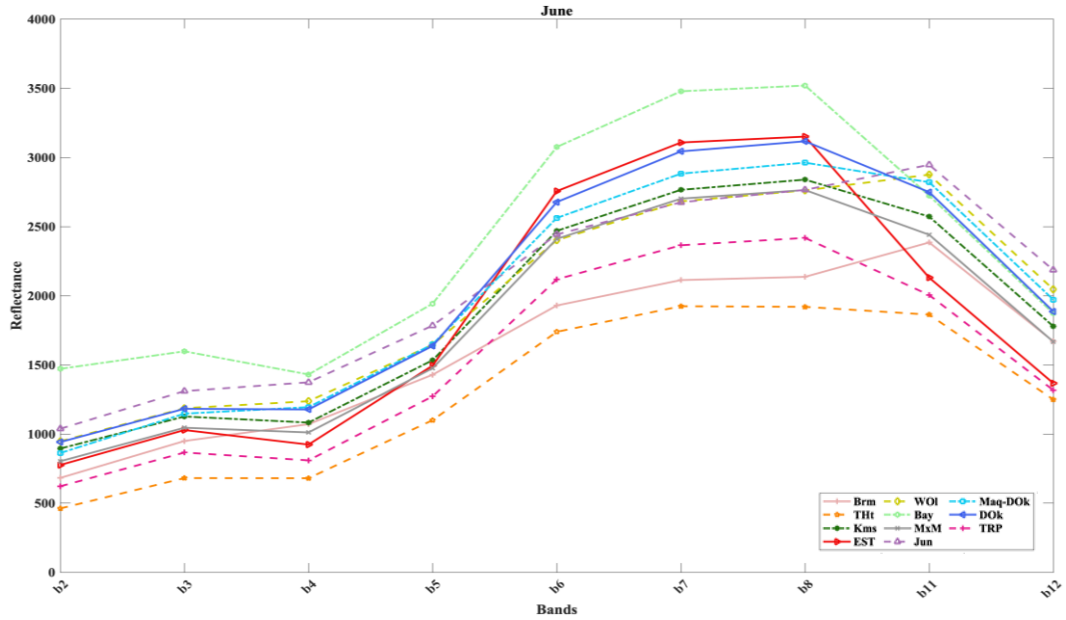

Figure 5.10. Spectral signatures of the classes in June.

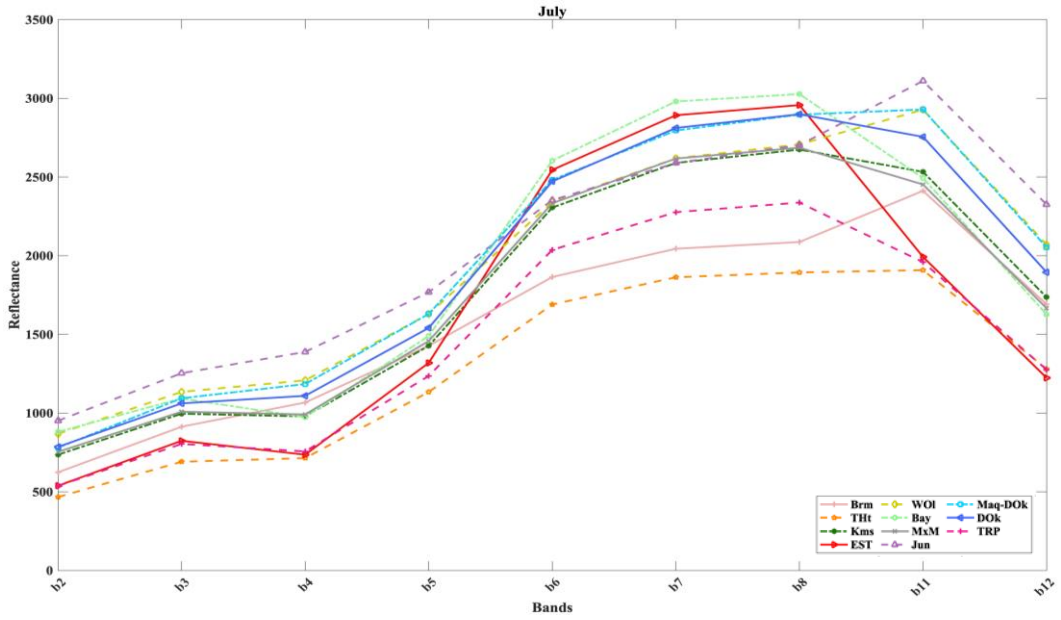

Figure 5.11. Spectral signatures of the classes in July.

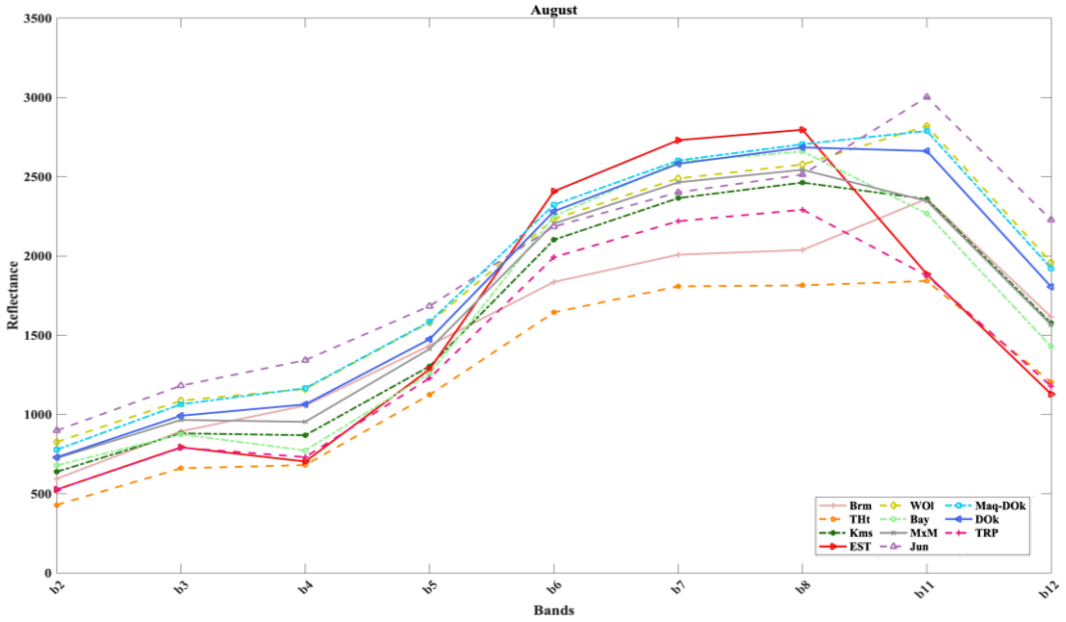

Figure 5.12. Spectral signatures of the classes in August.

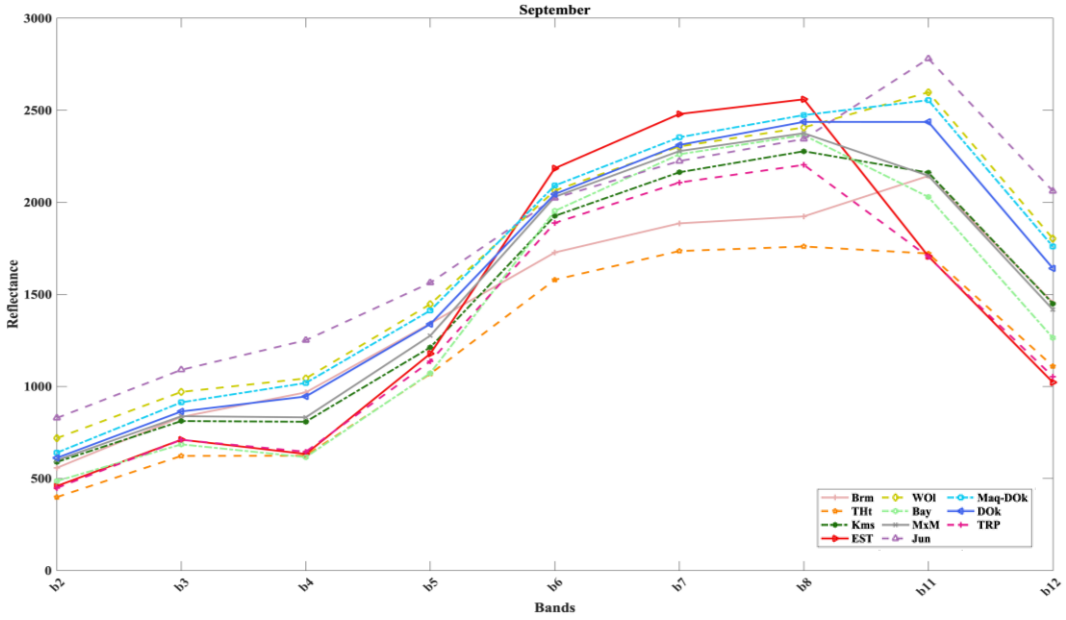

Figure 5.13. Spectral signatures of the classes in September.

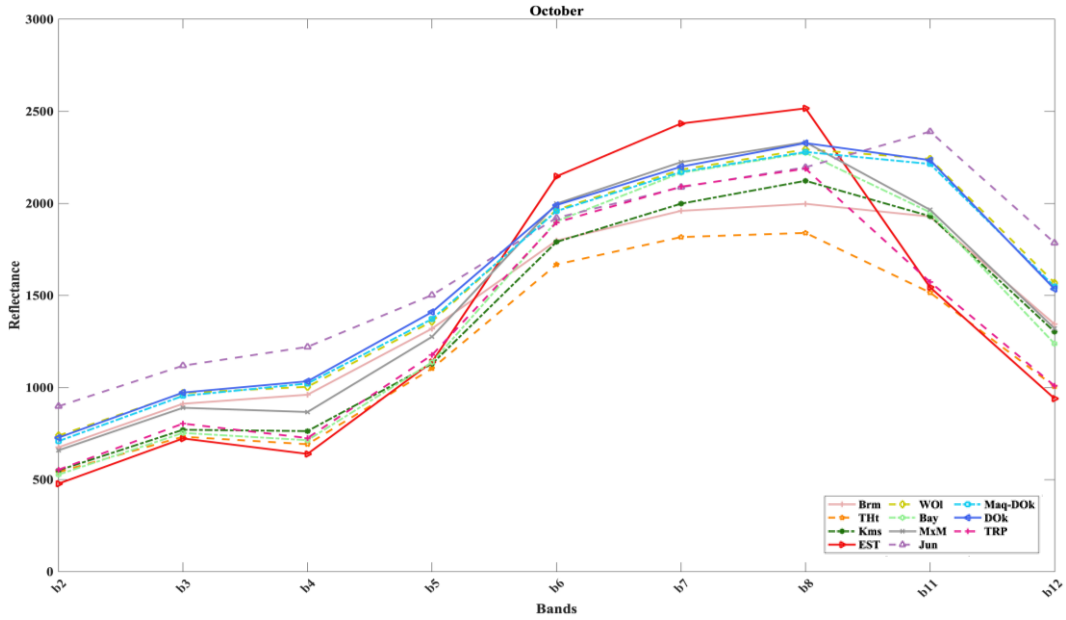

Figure 5.14. Spectral signatures of the classes in October.

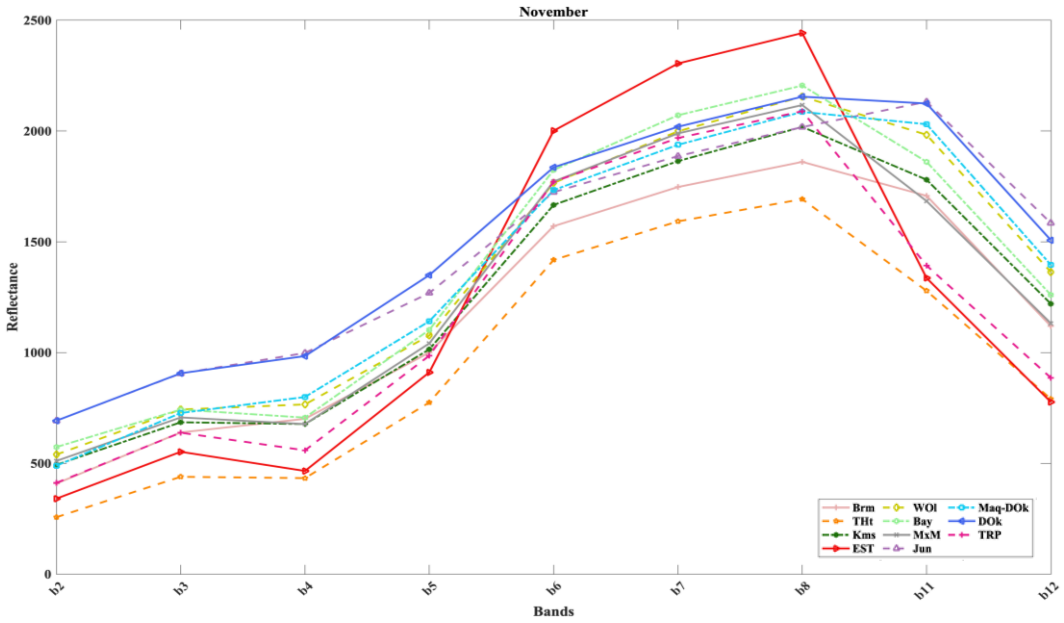

Figure 5.15. Spectral signatures of the classes in November.

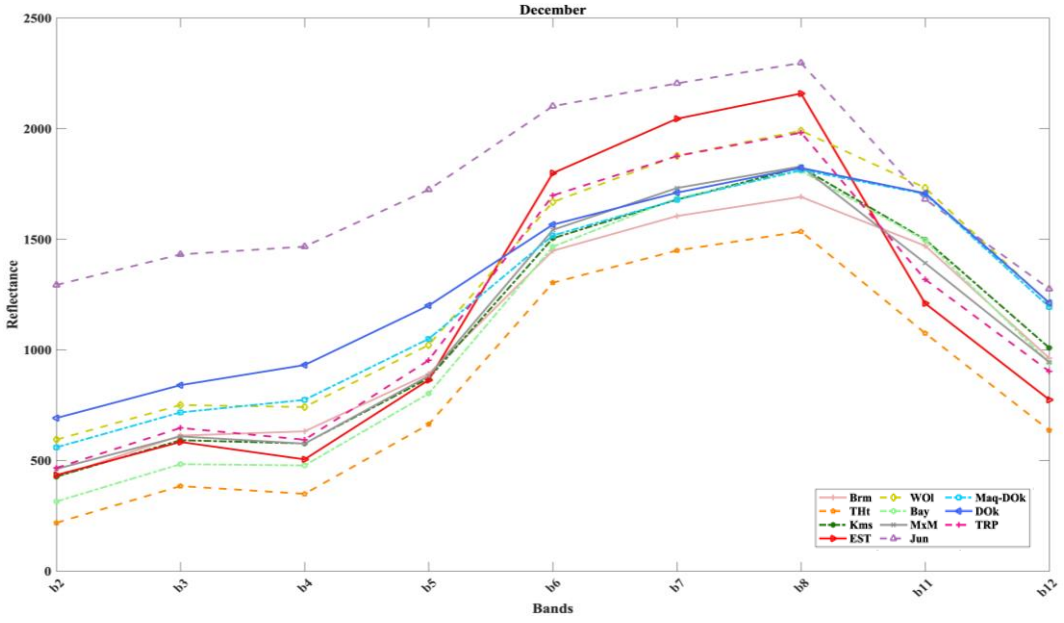

Figure 5.16. Spectral signatures of the classes in December.

Figure 5.17, Figure 5.21, and Figure 5.26 - Figure 5.29 illustrate the time-series for all the VIs and WI (i.e., NDVI, NDWI, SAVI, EVI, GVI, GDVI) used in this study.

Figure 5.17 portrays the NDVI time-series of all the alliances. Increase of NDVI in January is a peculiar behavior that does not generally happen since the presence of snow does not contribute to NDVI. The reason of the increase is not related to snow as no increase can be observed for junipers. This increase could be caused by grasses that continue to grow at low altitudes in January due to increased precipitation. This hypothesis is supported by the fact that the alliances with high NDVI values in January are those that favor lower altitudes (e.g., *Arbutus andrachne*). Histograms showing the elevation distribution of each alliance are shown in section 4.2.2.2.

The general increase of NDVI that can be seen in November could be caused by unwanted contribution of adjacent grass pixels and autumn rains. Figure 5.18, Figure 5.19, and Figure 5.20 show the NDVI time-series of random polygons taken from treeless areas in low (600 – 800 m), medium (1300 – 1600 m), and high (>2000 m) altitude, respectively. These figures show how lack of precipitation during the summer months contribute to the NDVI values. Because of minimum tree density/coverage, grasses in these areas dry up completely in July and August, which results in extremely low NDVI values. Figure 5.18 - Figure 5.20 also prove that increase of NDVI from October to January that can be seen in Figure 5.17 is due to grass.

A gradual decrease of NDVI can be observed from September to October for deciduous alliances (Deciduous Oak (DOk) and Maquis – Deciduous Oak (Maq-DOk)). The same behaviors can also be observed in the NDVI of Kermes Oak or Evergreen Oak (*Quercus coccifera (Quercus ilex, Quercus aucheri)*) and Tree Heath (*Erica arborea*), though these alliances are evergreen. This could be caused by presence of trees or shrubs from other alliances among the trees or shrubs of the dominant alliances.

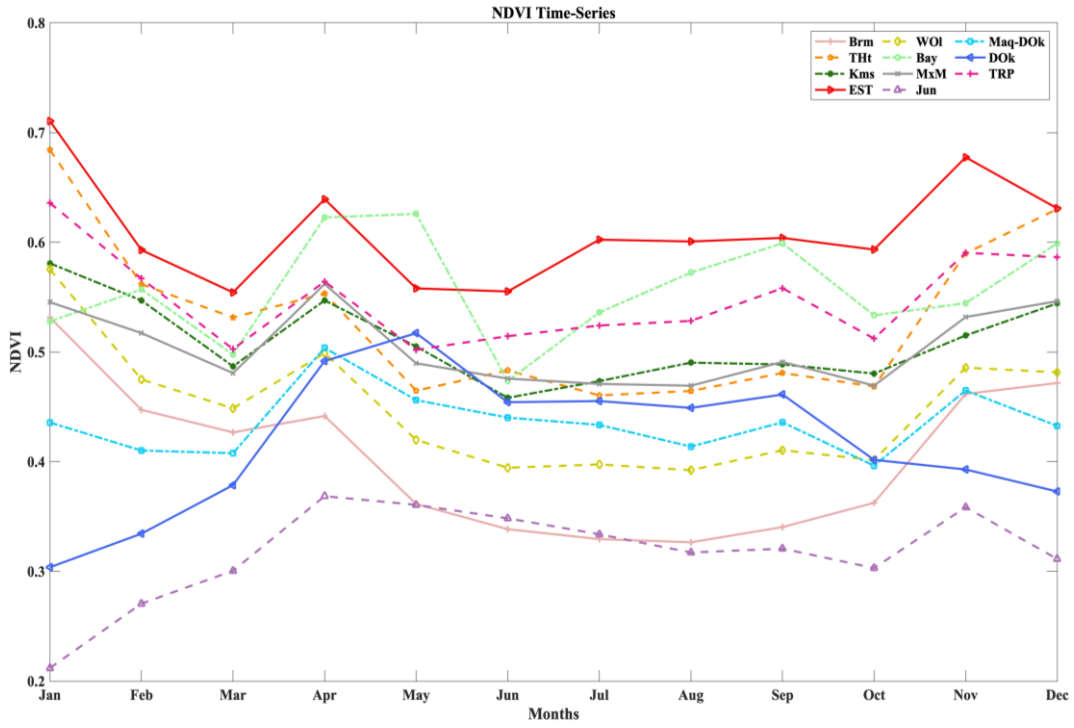

Figure 5.17. NDVI time-series.

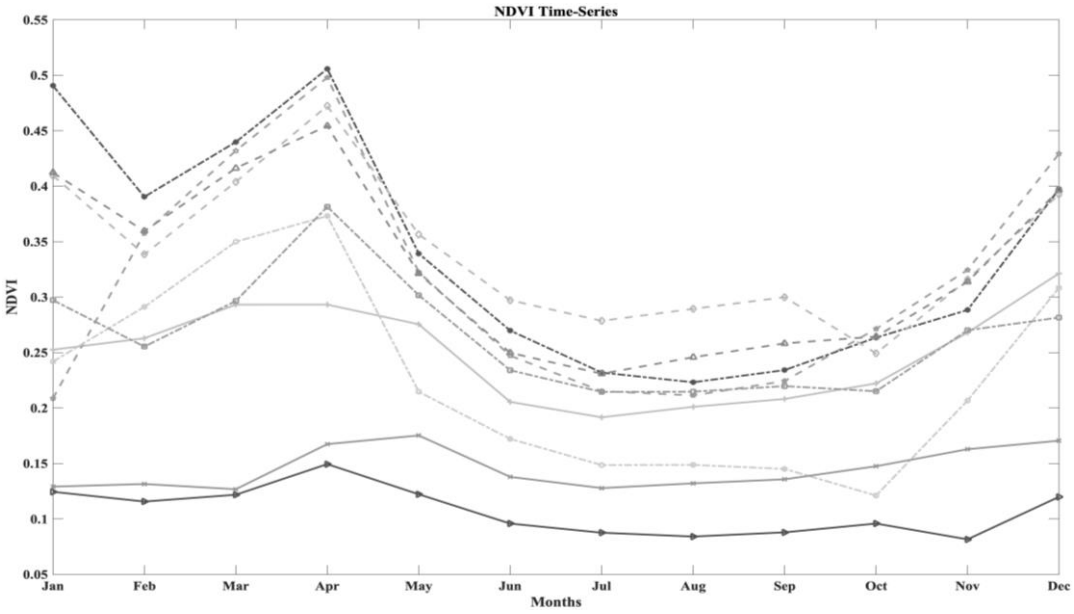

Figure 5.18. NDVI time-series of treeless areas in low altitude.

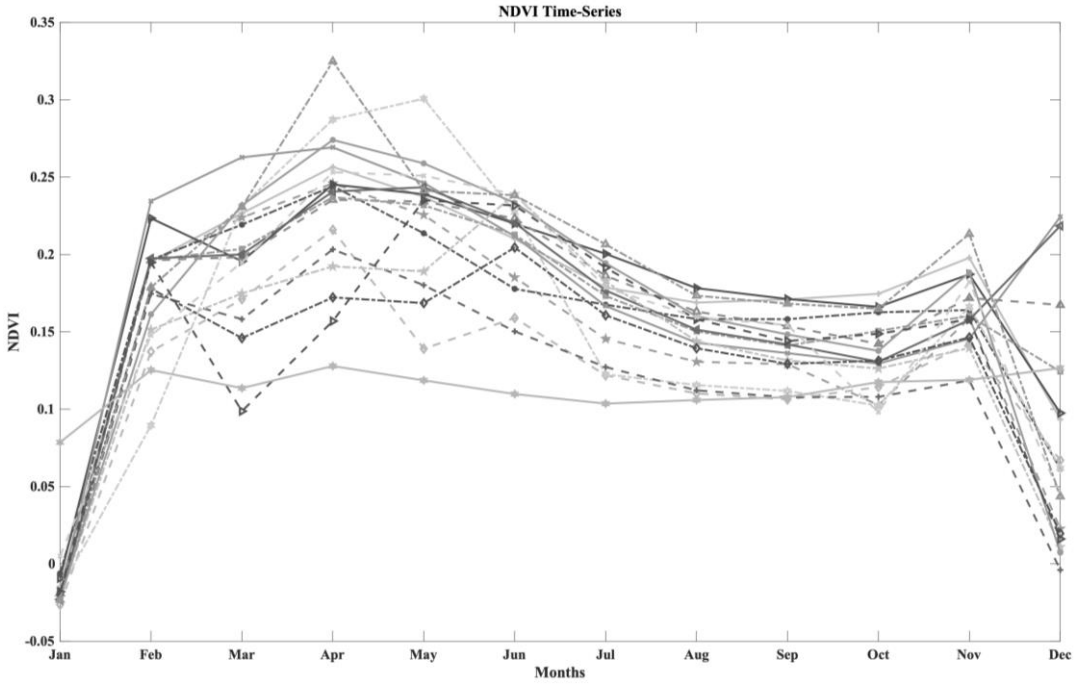

Figure 5.19. NDVI time-series of treeless areas in medium altitude.

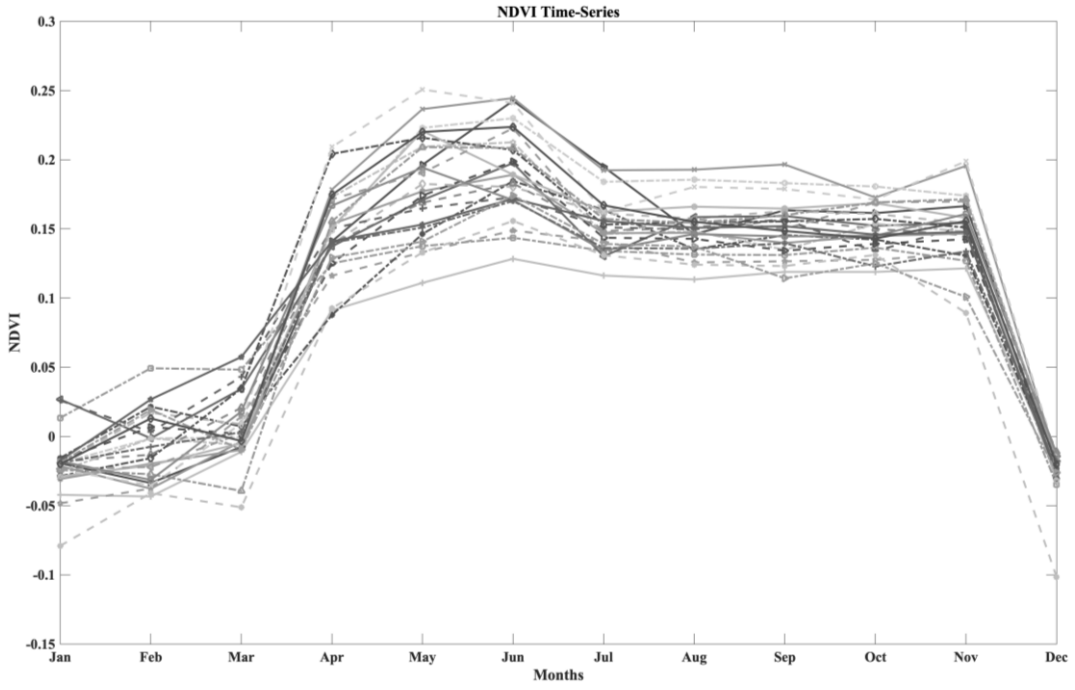

Figure 5.20. NDVI time-series of treeless areas in high altitude.

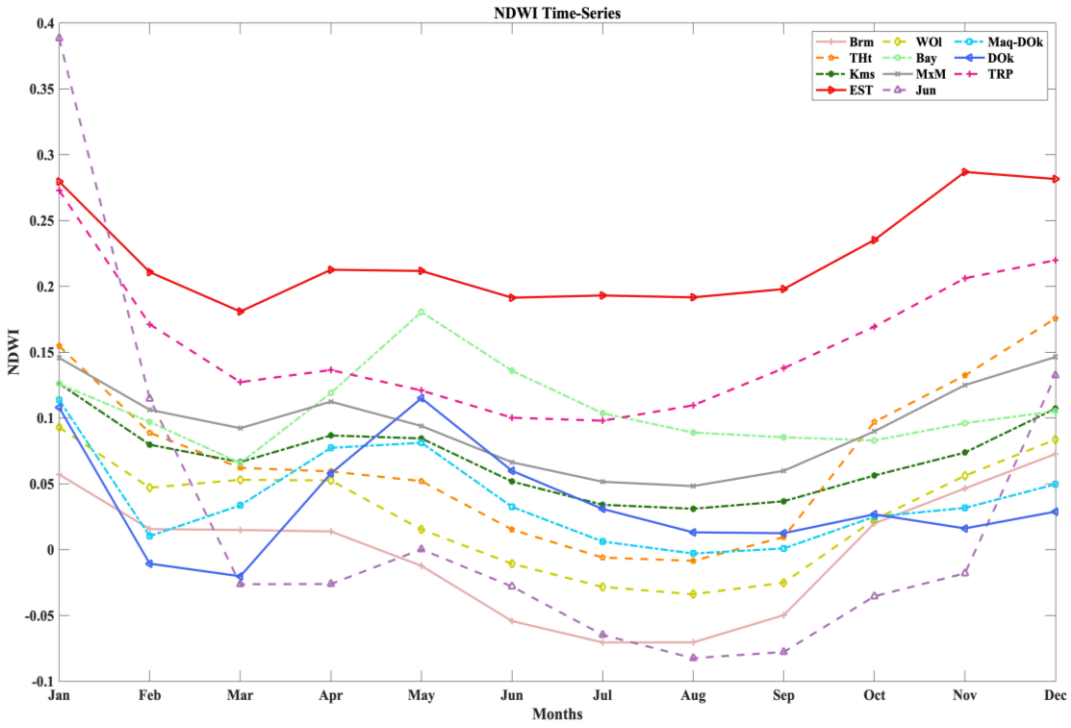

Figure 5.21. NDWI time-series.

Figure 5.21 illustrates the NDWI time-series that reacts to the variabilities of the moisture condition in vegetation. A general decreasing trend of NDWI can be seen from January to March for all alliances. NDWI continues to have a general decreasing trend for the evergreen alliances (e.g., THt, WOl, TRP, EST, Kms, Jun) until the summer months due to the decrease in precipitation. On the other hand, an increasing trend can be observed to take place from March up to May for the deciduous alliances (e.g., DOk and Maq-DOk), which is caused by the re-emerging presence of moisture as the new leaf buds start to appear along with the warmer temperatures. Figure 5.23 shows a column chart illustrating the changes of the monthly mean temperature of the areas on which Maq – DOk grow. A relatively subtle increase can be observed to take place in the evergreen alliance *Laurus nobilis* from March to May. This could be associated with regular increase of rainfall in spring. The areas upon which Bay tend to grow might be more humid than the areas

where DOk grow, as it can be seen in Figure 5.22 and in Figure 5.24. In May, DOk has precipitation value of approximately 42 mm, which is less than Bay that has precipitation of approximately 52 mm. From May to August, another decreasing trend can be seen for all alliances. The reason behind this is because of lack of rain during the summer months. Hence, NDWI values also decrease.

Figure 5.22 and Figure 5.24 show column charts illustrating the changes of monthly precipitation (mm) values taken from the areas on which Maq – DOk and Bay grow, respectively. Figure 5.25 shows a column chart illustrating the changes of the monthly mean temperature of the areas on which Bay grow.

The precipitation and mean temperature data for the column charts in this section are acquired from WorldClim Climatology V1 dataset (Hijmans et al., 2005). Generation process of this dataset is similar to the WorldClim BIO Variables V1 as explained in Section 4.2.2.1. Note that these values are generated through interpolation on a 30 arc-second resolution grid as well as through calculation of averages for 1960 – 1990 period. Hence, they cannot be used as direct correlation for interpreting the NDWI behaviors of each alliance. They can, however, be used to support the hypotheses presented above.

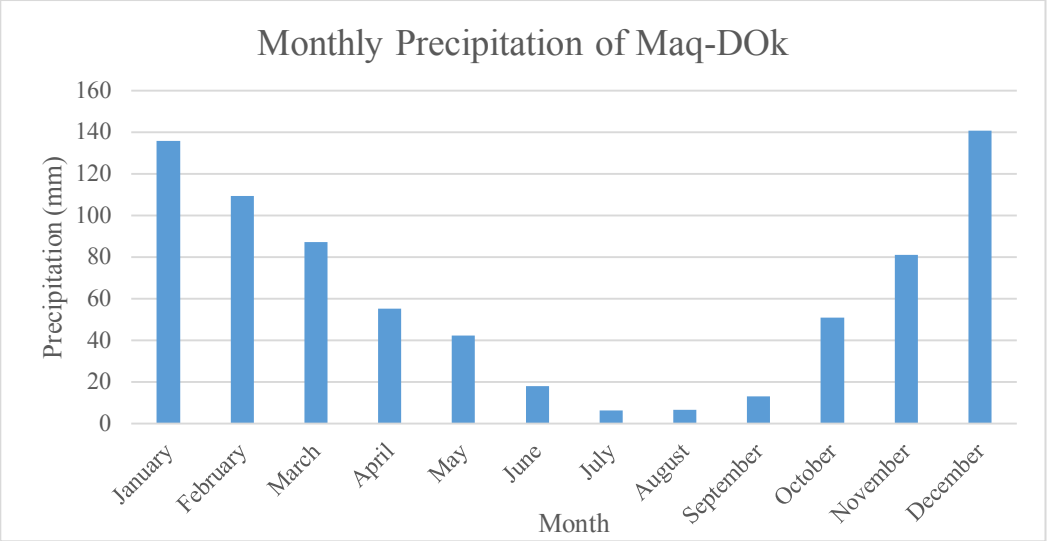

Figure 5.22. Column chart showing the monthly precipitation (mm) of Maq-DOk.

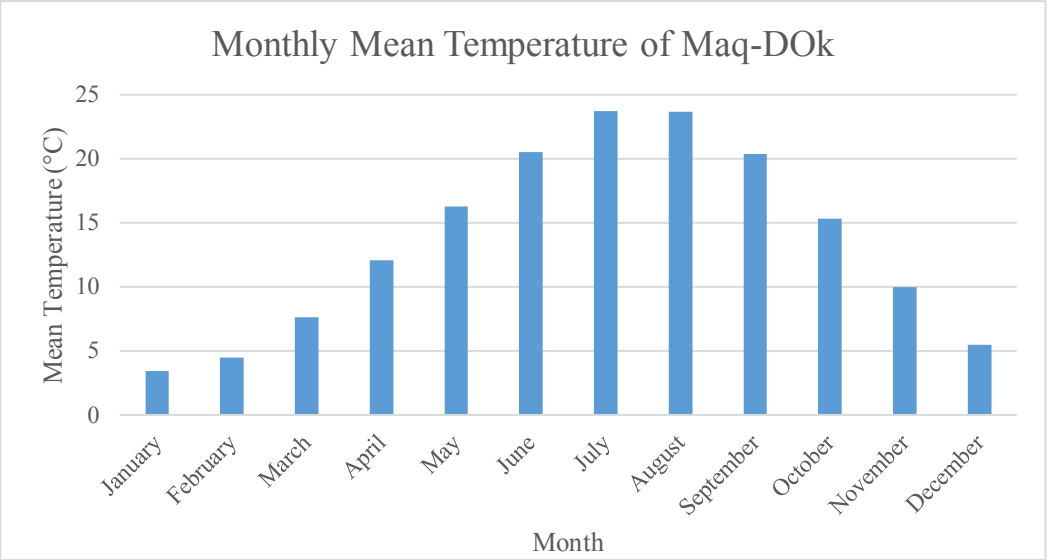

Figure 5.23. Column chart showing the monthly mean temperature (°C) of Maq-DOk.

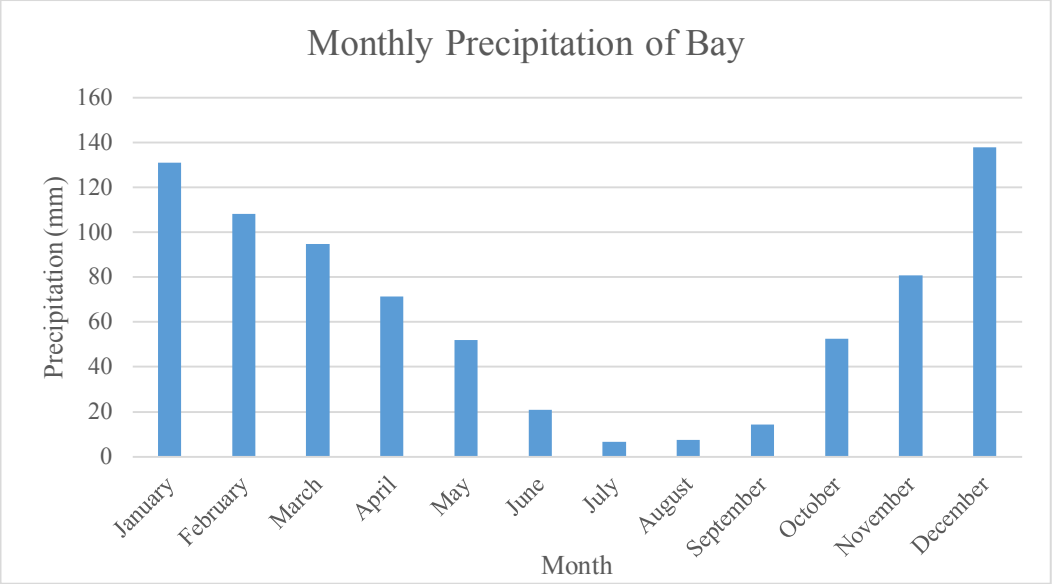

Figure 5.24. Column chart showing the monthly precipitation (mm) of Bay.

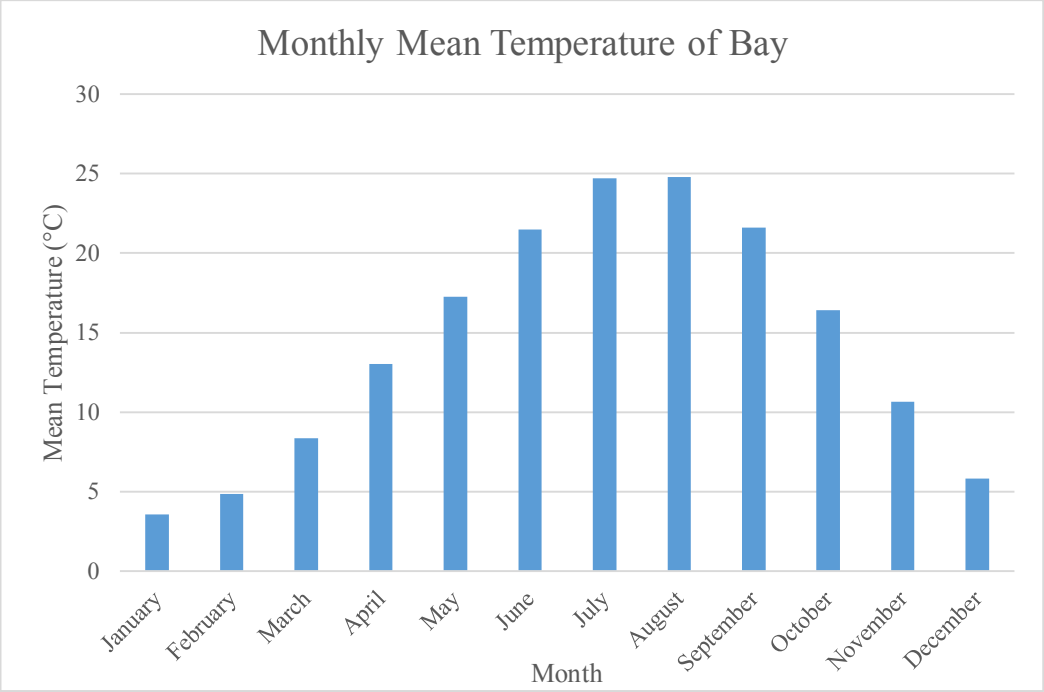

Figure 5.25. Column chart showing the monthly mean temperature (°C) of Bay.

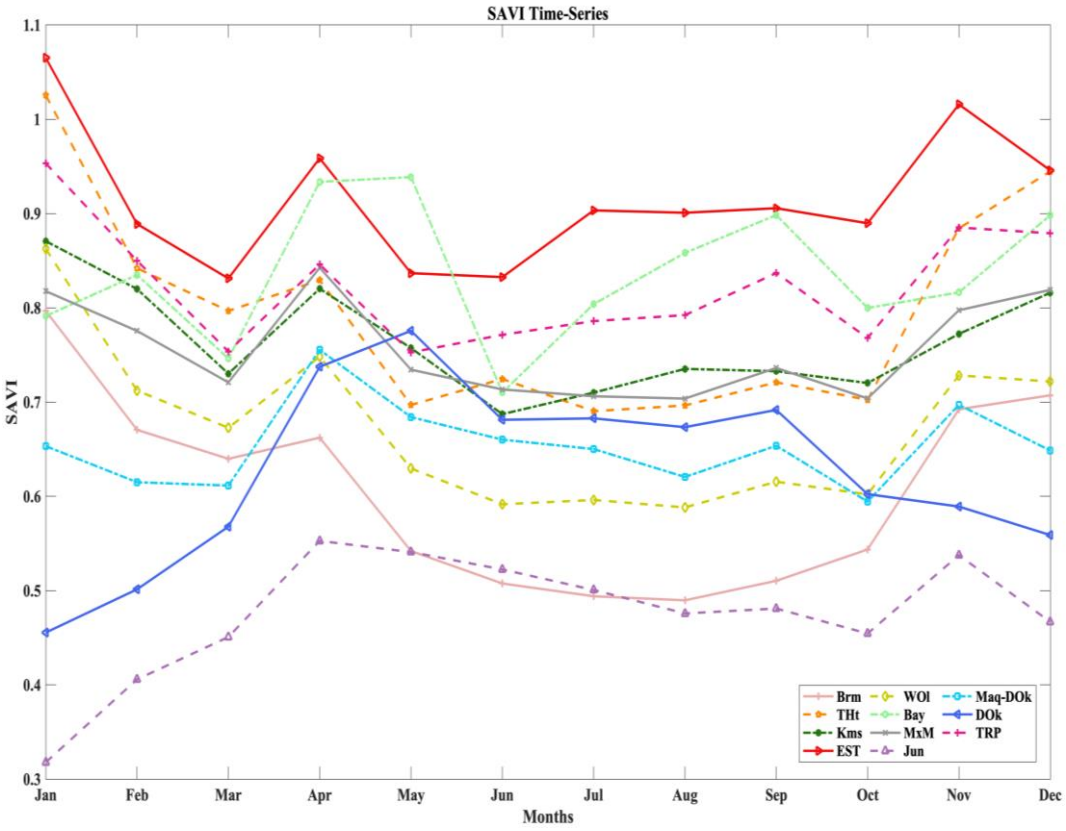

Figure 5.26. SAVI time-series.

Figure 5.26 portrays SAVI time-series. A general increasing trend can be seen to take place from March to April, making peak values in April, followed by a decreasing trend from April to May in all classes except Bay and DOk. SAVI values decreased from May to June for Bay and DOk, which was a little later in comparison to the other classes. Slight fluctuations can be observed throughout the summer months. Another SAVI peak can also be observed in November.

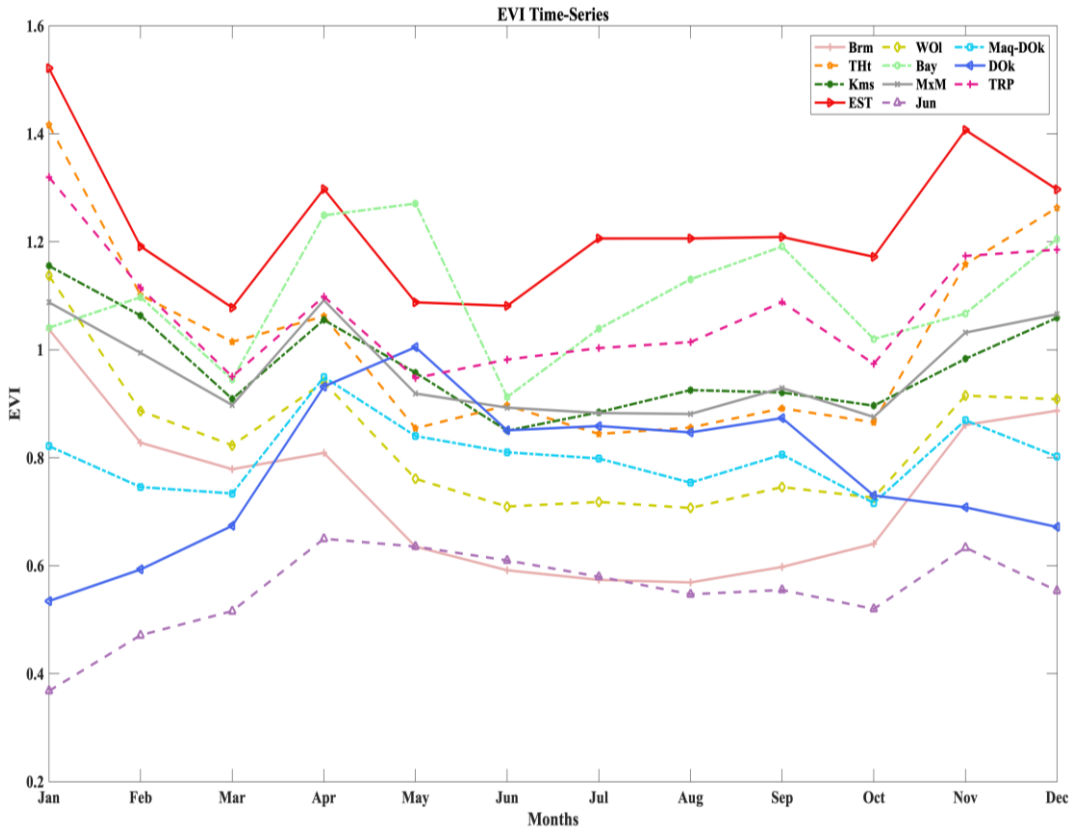

Figure 5.27. EVI time-series.

Figure 5.27 shows the EVI time-series. General increasing trend can be observed from March to April. EVI peak can be observed in April for all classes, except for Bay and DOk who have their peak EVI values in May. After the peak, EVI values tend to go down, which was then followed by slight variations until the next peak which occurred in September for Bay and DOk and in November for the rest of the classes.

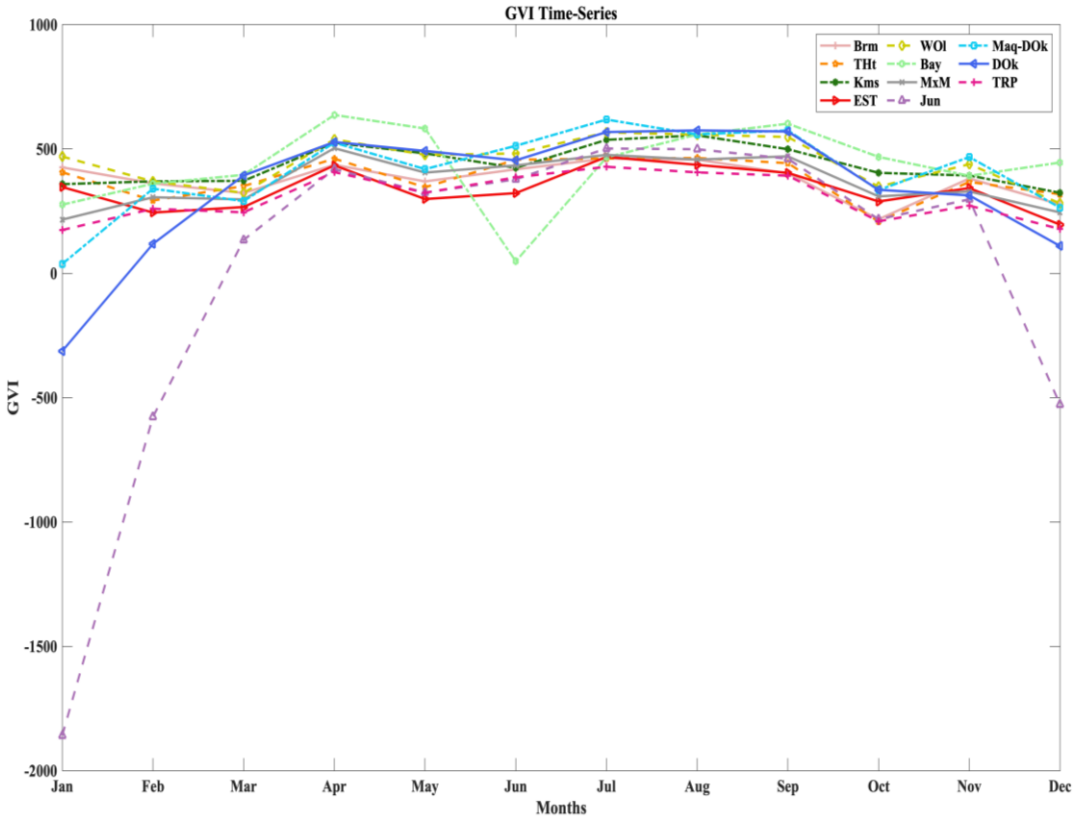

Figure 5.28. GVI time-series.

Figure 5.28 illustrates the GVI time-series. The GVI values can be seen to be fluctuating within 0 – 500 range for all months for all the classes, with the exception of extremely low GVI values in the months of December, January, and February for *Juniperus spp.* (Jun). This could be caused by the high snow cover observed in those winter months. Another anomaly can be observed in the GVI value of *Olea europea ssp. europea var. sylvestris* (WOl) in June, which dropped to almost zero, and in April, which increased to above 500.

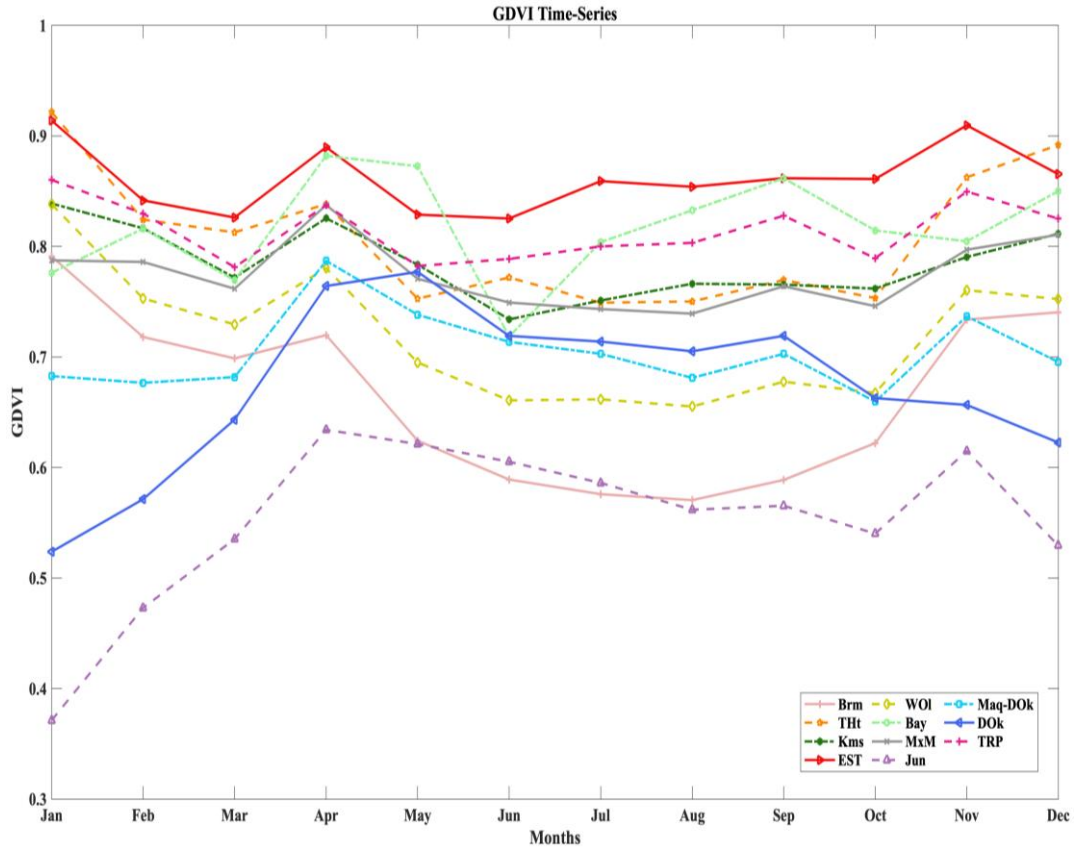

Figure 5.29. GDVI time-series.

Figure 5.29 portrays the GDVI time-series. GDVI values for all classes generally behave the same way in terms of trends. Two peaks can be observed in the GDVI values. The first peak took place in April for all the classes except Bay and DOk, who have their first peak one month later in May. The second peak can be observed to take place in November for all classes except Bay and DOk. The second GDVI peak for Bay and DOk took place in September.

Figure 5.30 - Figure 5.35 illustrate the temporal changes of the spectral signatures of each band for all classes. In the visible blue part of the spectrum (B2), THt and Jun has the lowest reflectance and highest reflectance values, respectively, throughout the year relative to the other alliances. This is true for the green and red part of the visible spectrum as well, except for the value of the red band of EST in autumn,

which is slightly lower than THt. Within the visible blue spectrum, the reflectance values are generally low relative to the reflectance that can be observed coming from the other visible spectrums. Relatively low reflectance values can be observed in April for all the visible bands of all alliances compared to the rest of the year. In autumn months (i.e., from September to October), a general increase can be seen to take place in the spectral reflectance values of the visible bands (i.e., B2, B3, and B4) for all alliances except Kms. From October to November, a decreasing trend can be observed in the visible bands for all the alliances except for *Laurus nobilis*. During June, in the blue band (B2), green band (B3), red band (B4), and NIR band (B8), *Laurus nobilis* has the highest spectral reflectance values. In the NIR band (B8) higher diversity can be observed within the reflectance patterns in comparison to the reflectance patterns of the visible bands (Grabska et al., 2019). A peak can be observed in NIR (B8) reflectance in May for the deciduous alliances DOk and Maq-DOk, and the evergreen alliances THt, Brm, TRP, and Jun, while Bay, MxM, EST, Kms, and WOl have their peak in June. NIR reflectance of Jun, DOk, Bay, and Maq-DOk have a sharp decrease from January to February. In the SWIR spectrum (B11 and B12), reflectance patterns generally have higher values in summer months compared to the rest of the year.

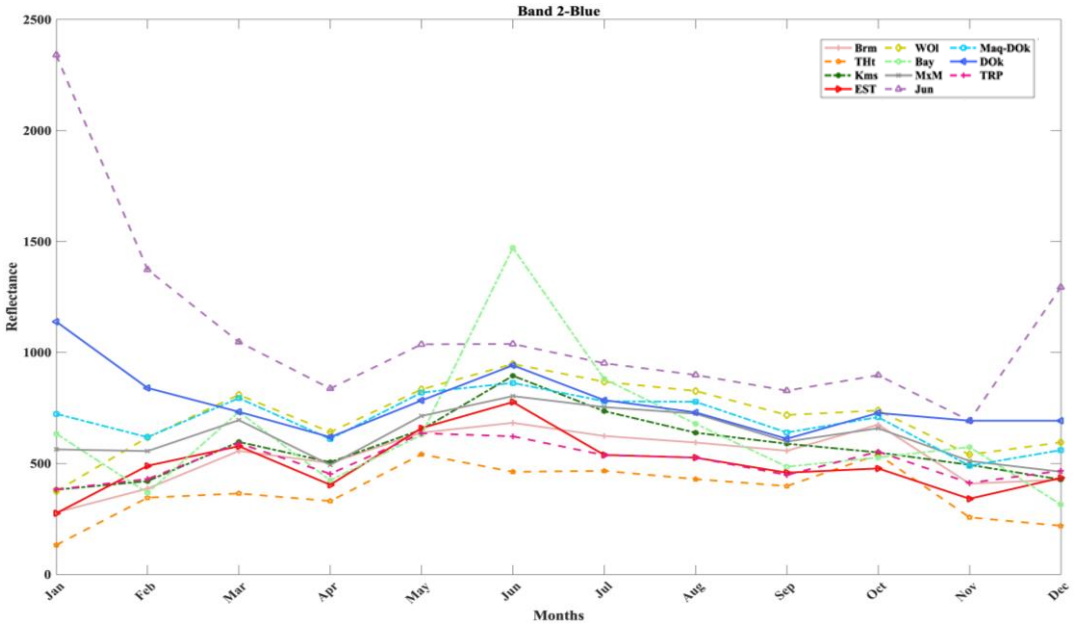

Figure 5.30. Temporal changes of band 2 (blue).

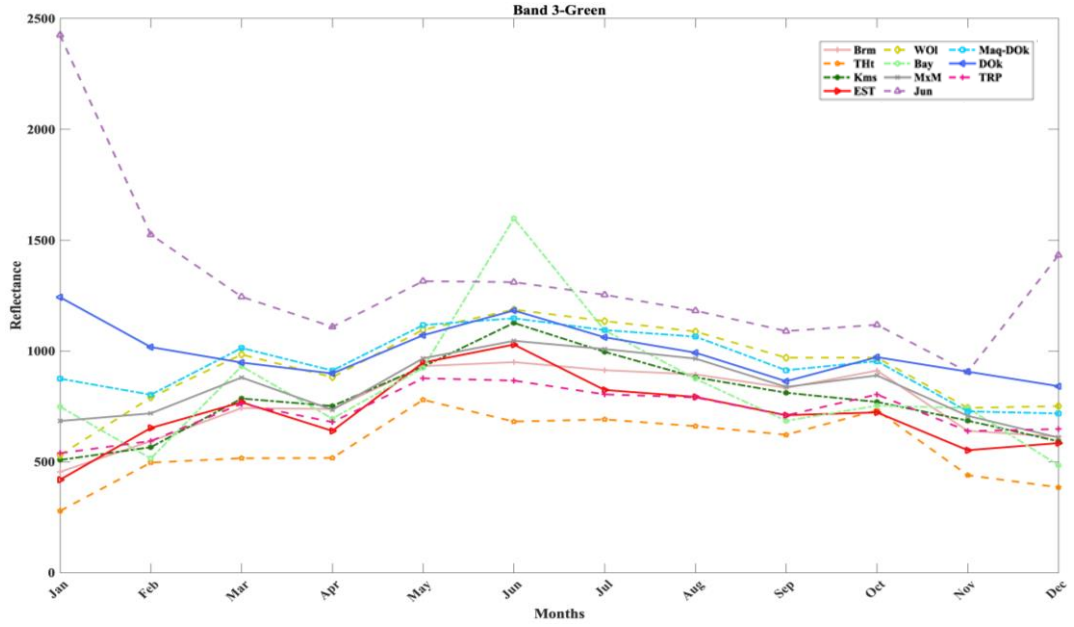

Figure 5.31. Temporal changes of band 3 (green).

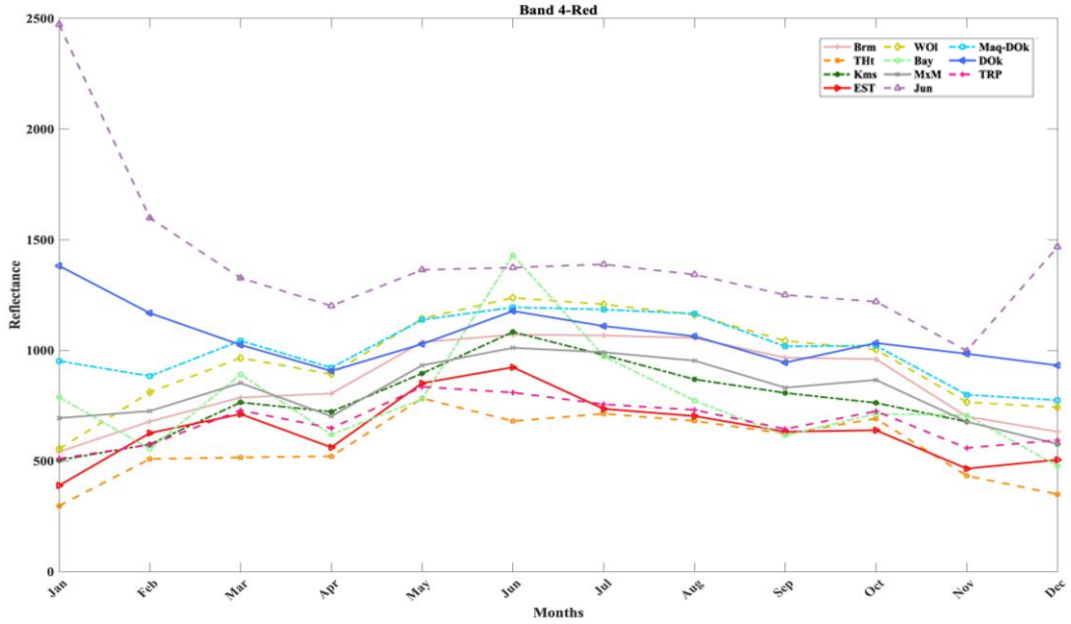

Figure 5.32. Temporal changes of band 4 (red).

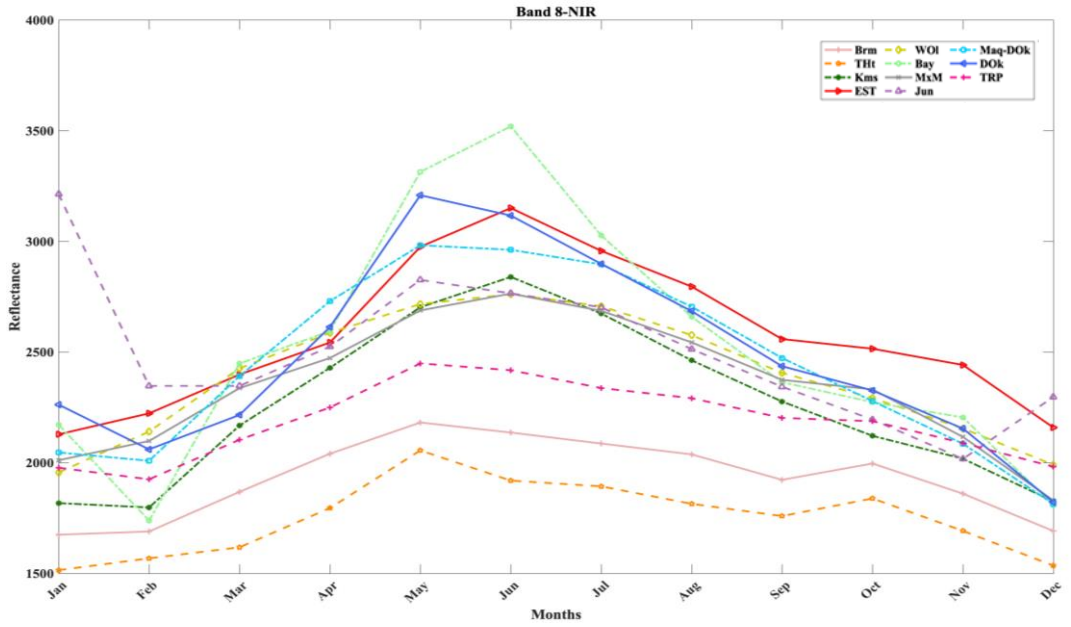

Figure 5.33. Temporal changes of band 8 (NIR).

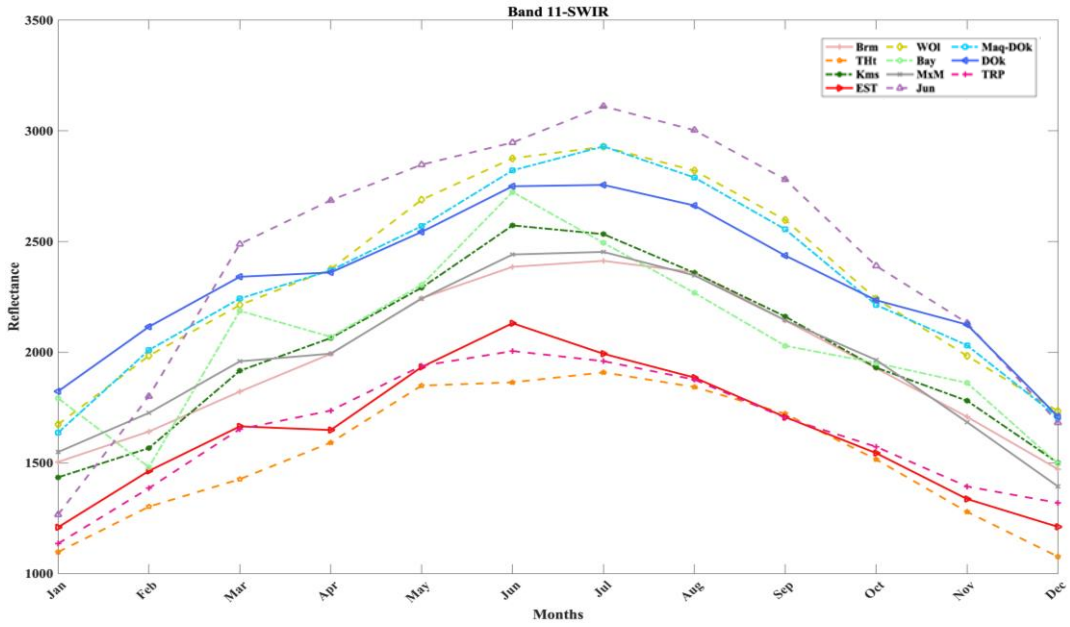

Figure 5.34. Temporal changes of band 11 (SWIR1).

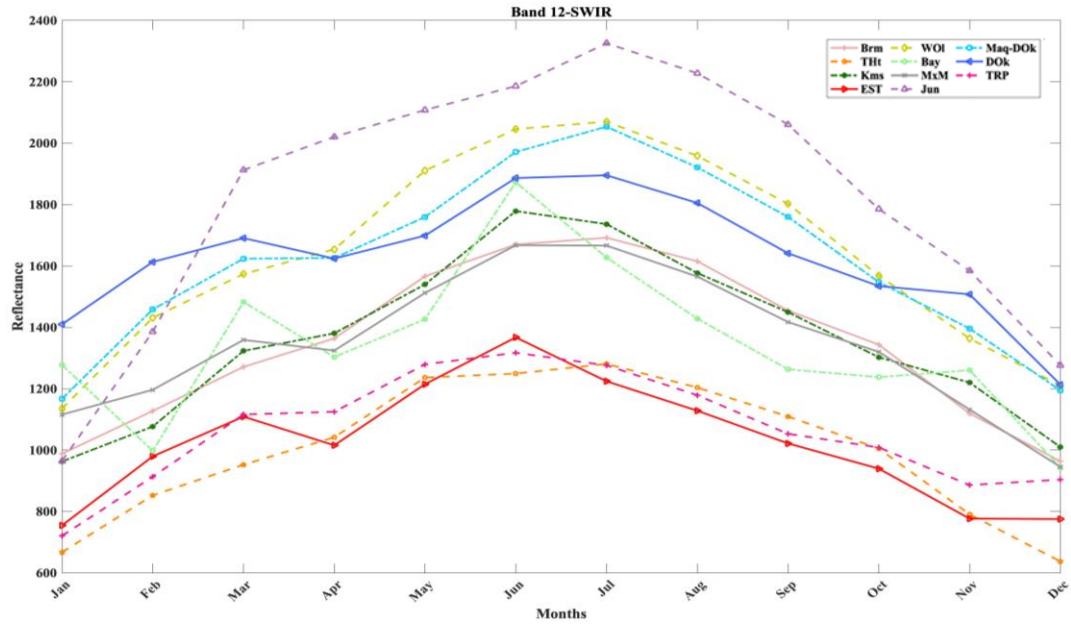

Figure 5.35. Temporal changes of band 12 (SWIR2).

5.4.2 Environmental Features

Among the environmental features, BIO3 (isothermality) and BIO14 (precipitation of driest month) are eliminated due to low importance, while the rest of the remaining environmental features are kept as they are highly influential. In the end, a total of 21 environmental features remained. These features are listed in Table 5.3.

Table 5.3. Peak environmental features.

Surface Curvature	BIO11
Distance to Streams	BIO12
Distance to Ridges	BIO13
BIO1	BIO15
BIO2	BIO16
BIO4	BIO17
BIO5	BIO18
BIO6	BIO19
BIO8	Elevation
BIO9	Slope
BIO10	

5.4.3 Combination of Remotely-Sensed Features and Environmental Features

In terms of the feature importance, when remotely-sensed features and environmental features are combined, the most important feature is BIO2 (mean diurnal range), followed by STP3 (which is the coefficient corresponding to the (y) of the STP), and BIO13 (precipitation of wettest month). Then comes NDWI of October, BIO5 (maximum temperature of warmest month), BIO4 (temperature

seasonality), Feature2, and BIO17 (precipitation of driest quarter). Slope, NDWIf3 (coefficient of (x)), BIO12 (annual precipitation), elevation, STP8 (the coefficient corresponding to the (xy^2) of the STP), and GVI of November also contribute significantly to the model.

On the contrary, all NDVI, SAVI, EVI, and GDVI values from all the months are eliminated.

Figure 5.36 shows how feature reductions contribute to the RF classification accuracy. The peak point in the overall accuracy is marked after the first 14 features. Using more than 14 features actually decreases the overall classification accuracy. These 14 features along with their respective importance are shown in Figure 5.37.

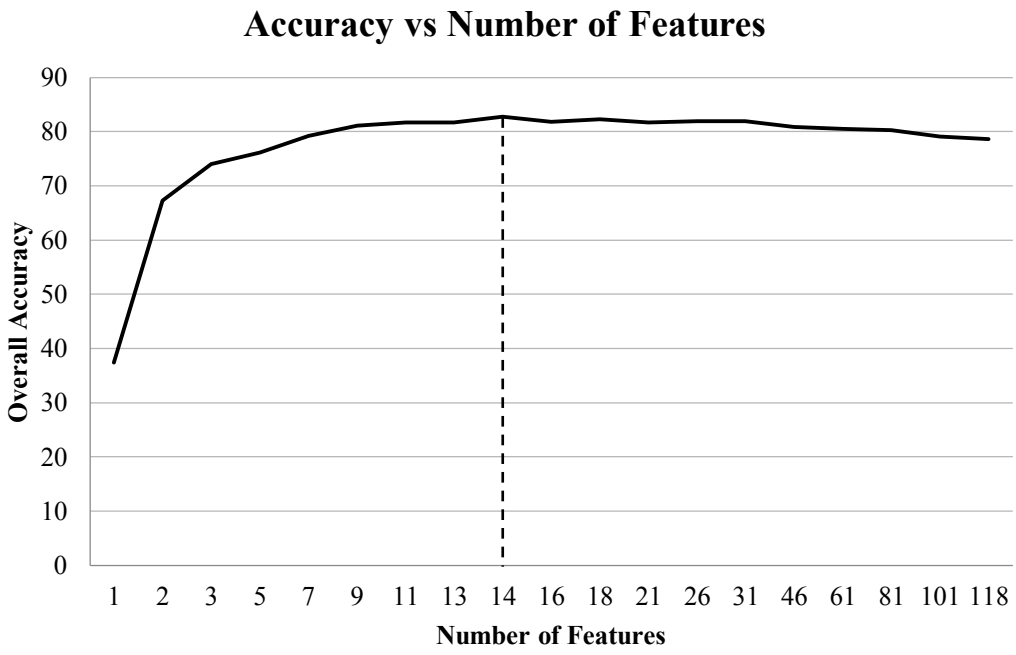

Figure 5.36. OA plotted against total number of combined features.

5.5 Final Classification

In the end, a total of eleven alliance classes are used in the final classification. Table 5.4 shows the distribution of GT polygons among the eleven dominant maquis alliances used in the final classification analysis.

Table 5.4. Distribution of the GT polygons among the eleven alliance classes.

English Name	**Latin**	**Number of Polygons**
Broom (Brm)	*Genista acanthoclada*	525
Tree Heath (THt)	*Erica arborea*	216
Kermes Oak (including other evergreen oak) (Kms)	*Quercus coccifera (Quercus ilex, Quercus aucheri)*	320
Eastern Strawberry Tree (EST)	*Arbutus andrachne*	965
Wild olive (WOl)	*Olea europaea ssp. europaea var. sylvestris*	444
Bay, Laurel (Bay)	*Laurus nobilis*	376
Mixed Maquis (MxM)	Mixed *Maquis*	283
Junipers (Jun)	*Juniperus spp.*	987
Maquis - Deciduous oak (Maq-DOk)	*Maquis* – Deciduous oak	208
Deciduous oak (DOk)	Deciduous oak	564
Turkish Red Pine (TRP)	*Pinus brutia*	301

Figure 5.37 shows the predictor feature importance used in the final classification based on combination of remotely-sensed features and environmental features.

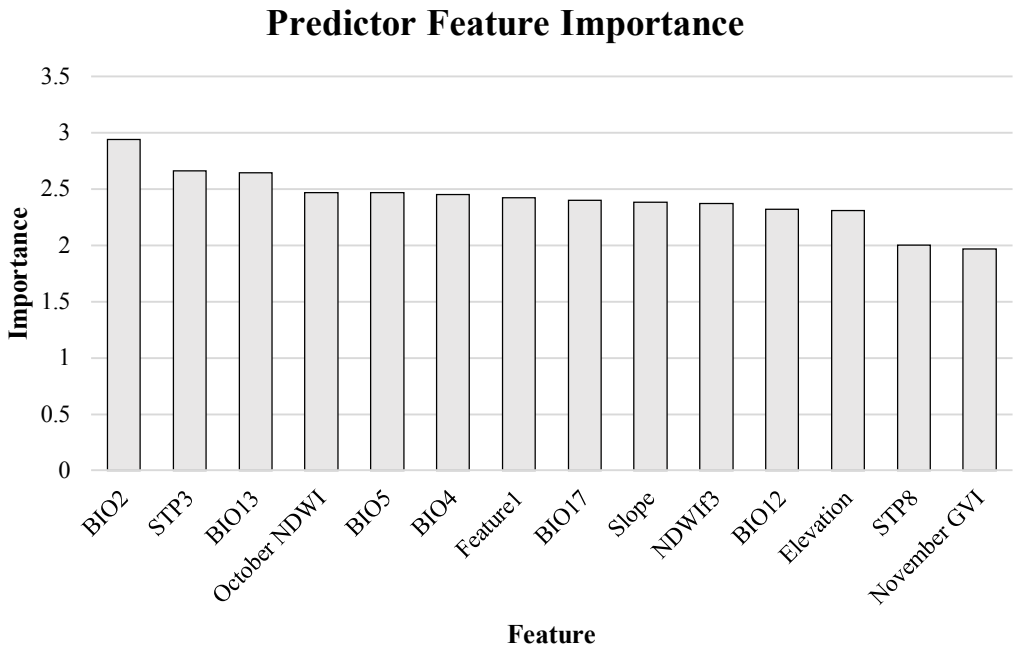

Figure 5.37. Predictor feature importance chart.

5.6 Classification Maps

The alliance-level classification maps of dominant maquis-types in the Mediterranean region of Turkey acquired from RF classification using remotely-sensed features, environmental features, as well as a combination of remotely-sensed features and environmental features are presented in Figure 5.38, Figure 5.40, and Figure 5.42 respectively.

As stated by (Demirbas Caglayan et al., 2020), even though *Pinus brutia* (TRP) makes up less than 13% of the total masked area in all three classification schemes, foresters simply label and refer to the whole area as “sparse *Pinus brutia* forests”.

5.6.1 Classification Map Based on Remotely-Sensed Features

The alliance-level classification map acquired from RF classification using remotely-sensed features result in a very heterogeneous map of great variations with 64% classification accuracy as shown in Figure 5.38. Figure 5.39 presents the same classified map as Figure 5.38, but exclusively of the masked areas. Based on this map, for the classification done with only remotely-sensed features, the most dominant alliance is *Juniperus spp.* (53.7%), followed by the mixed maquis class (11.4%), *Arbutus andrachne* (11.3%), Deciduous oak (8.6%), *Olea europaea ssp. europaea var. sylvestris* (5.7%), *Genista acanthoclada* (2.3%), *Laurus nobilis* (1.9%), *Quercus coccifera (Quercus ilex, Quercus aucheri)* (1.3%), Maquis – Deciduous oak (0.9%), and *Erica arborea* (0.7%). *Pinus brutia* makes up a total of only 2.2% of the masked areas. Considering the heterogeneity of the region, remotely-sensed features generate a more natural-looking map in comparison to the map generated from RF classification using environmental features. Because, the meteorological variables are interpolated from large grids in the order of kilometers and their variation is very smooth. Topographic features are also smooth when compared to pixel size. On the other hand, spectral measurements can change abruptly from a pixel to the next depending on the land cover.

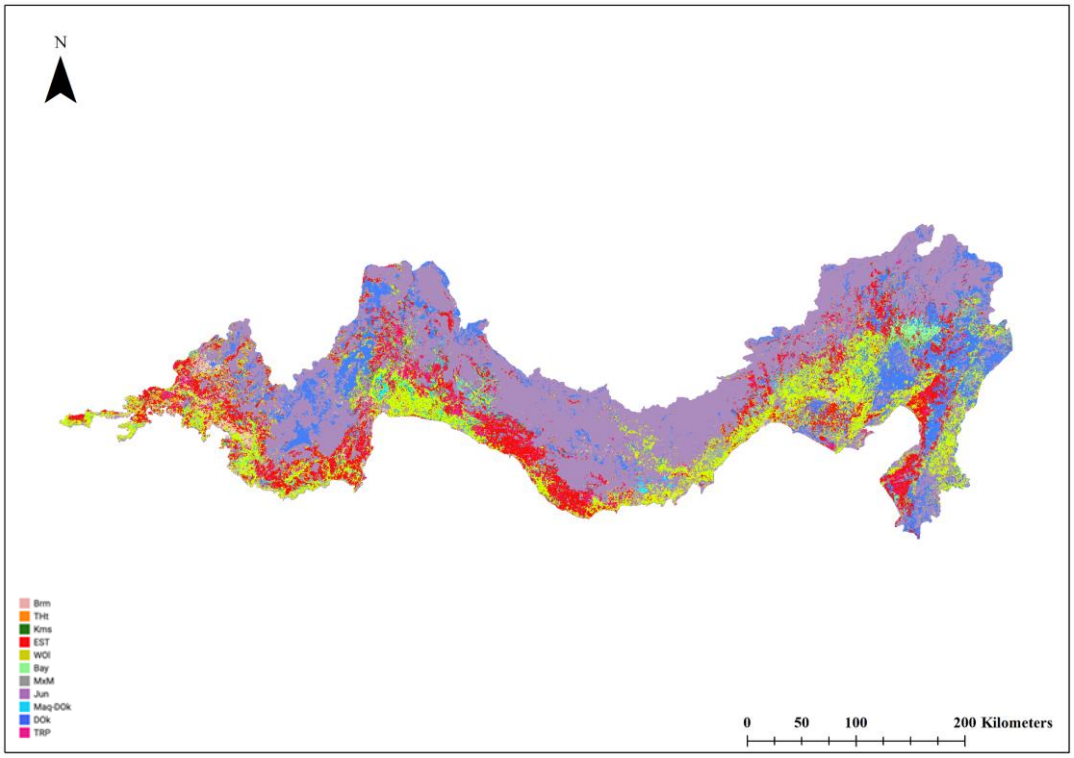

Figure 5.38. Alliance-level classification map using only remotely-sensed features.

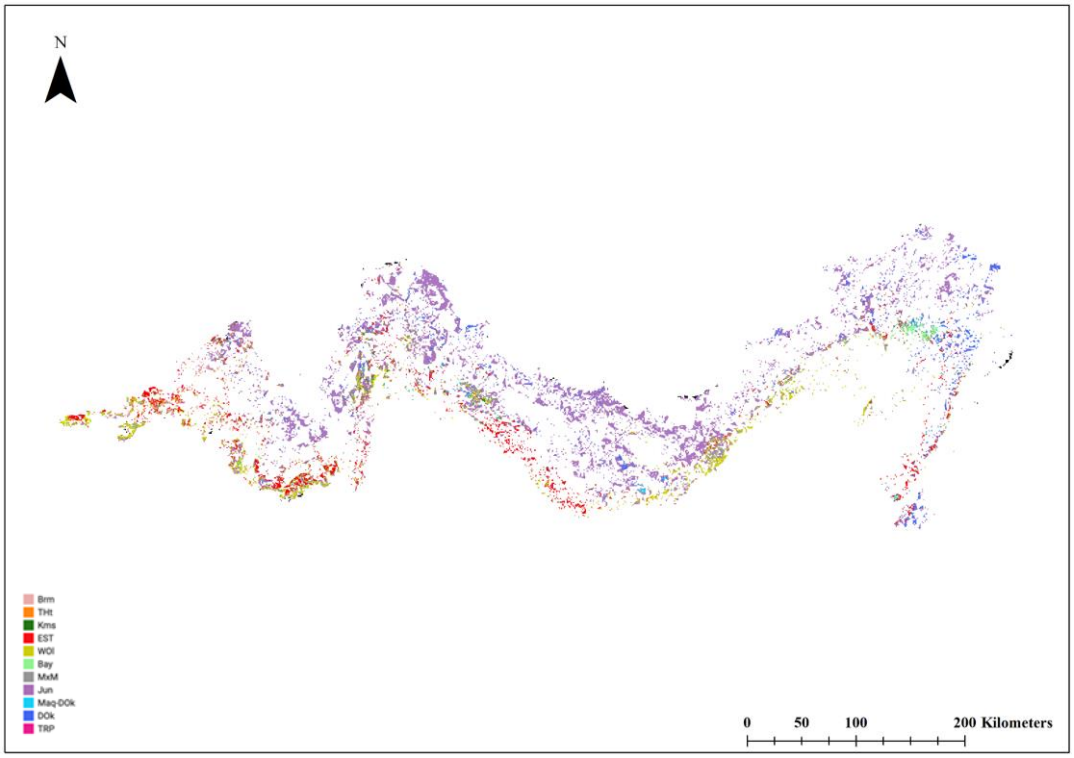

Figure 5.39. Alliance-level classification map using only remotely-sensed features with the maquis mask.

5.6.2 Classification Map Based on Environmental Features

The alliance-level classification map obtained from RF classification using environmental features only results in a smoother-looking map with 82.1% classification accuracy as shown in Figure 5.40. Figure 5.41 presents the masked areas of Figure 5.40. The classification map produced based on environmental features generated the following percentages: *Juniperus spp.* (45.5%), followed by deciduous oak (7.5%), the mixed maquis class (6.9%), *Olea europaea ssp. europaea var. sylvestris* (6.8%), *Genista acanthoclada* (5.9%), *Arbutus andrachne* (5.5%), *Quercus coccifera (Quercus ilex, Quercus aucheri)* (3.5%), *Laurus nobilis* (2.8%),

Maquis – Deciduous oak (1.6%), and *Erica arborea* (0.9%). While *Pinus brutia* makes up a total of only 12.6% of the masked areas.

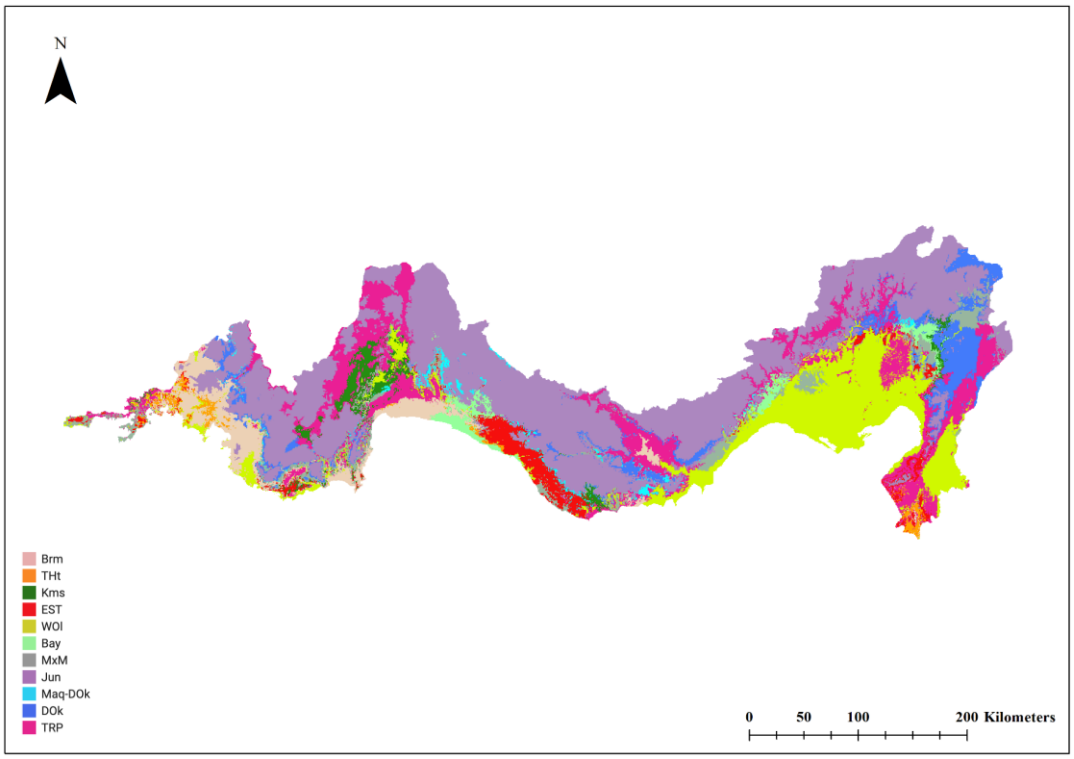

Figure 5.40. Alliance-level classification map using only the environmental features.

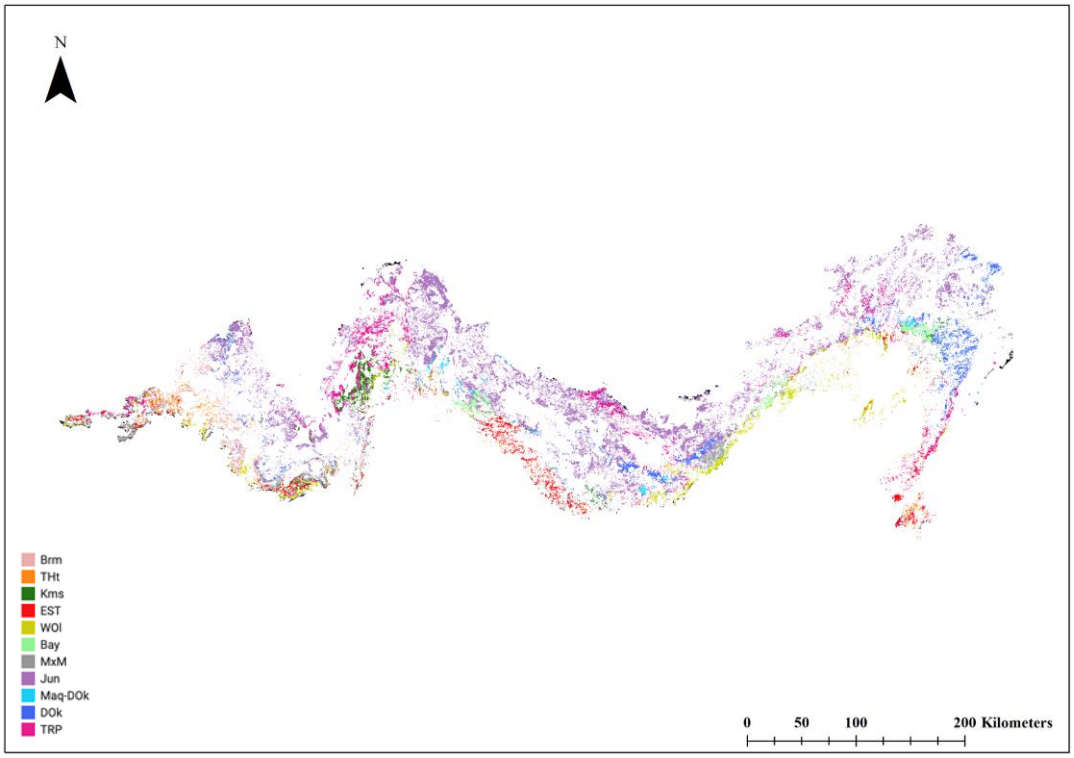

Figure 5.41. Alliance-level classification map using only environmental features with the maquis mask.

5.6.3 Classification Map Based on Combination of Remotely-Sensed Features and Environmental Features

Combining remotely-sensed features with environmental features results in 80.1% classification accuracy as shown in Figure 5.42. Figure 5.43 presents the same classified map as Figure 5.42, however exclusive to the masked areas. The classification map produced based on combined features generated the following percentages: *Juniperus spp.* (49.4%), followed by the mixed maquis class (8.0%), Deciduous oak (7.3%), *Olea europaea ssp. europaea var. sylvestris* (6.6%), *Arbutus andrachne* (6.3%), *Genista acanthoclada* (5.7%), *Quercus coccifera (Quercus ilex, Quercus aucheri)* (5.1%), *Laurus nobilis* (2.8%), *Erica arborea* (1.4%), Maquis -

Deciduous oak (0.9%). *Pinus brutia* makes up 6.5% of the total masked areas. The resulting map is not as detailed as the map generated by remotely-sensed features, but not as smooth as the map generated by environmental features, as it can be seen in Figure 5.42.

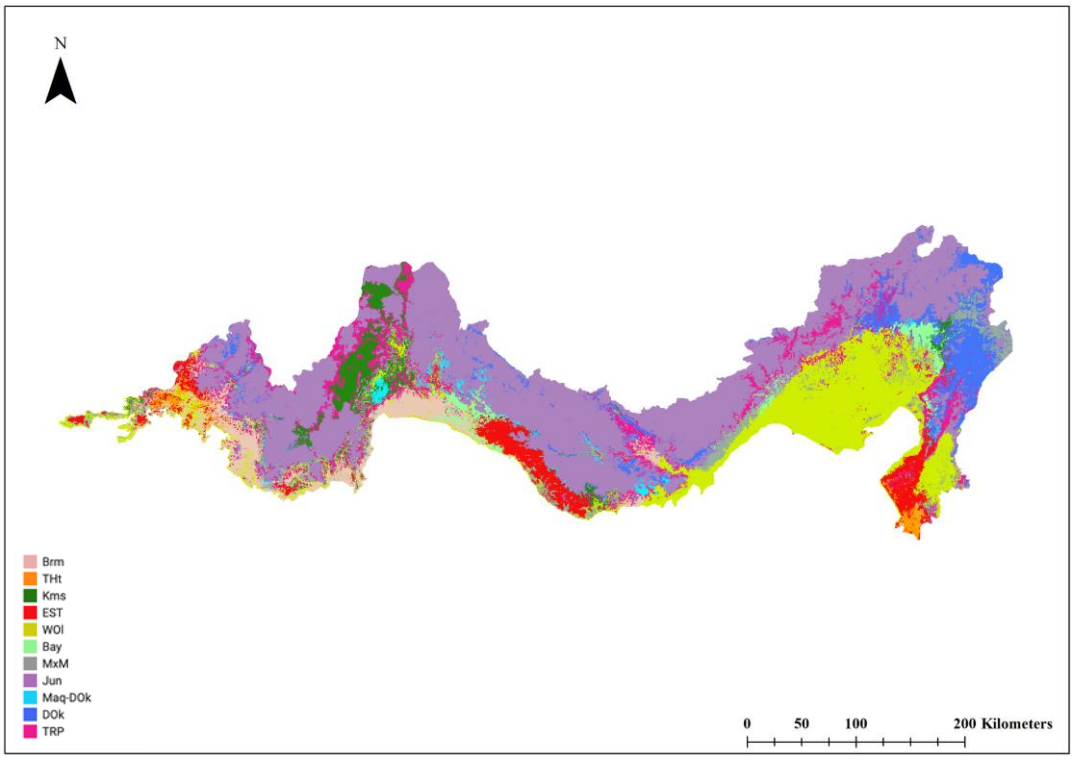

Figure 5.42. Alliance-level classification map using both set of features.

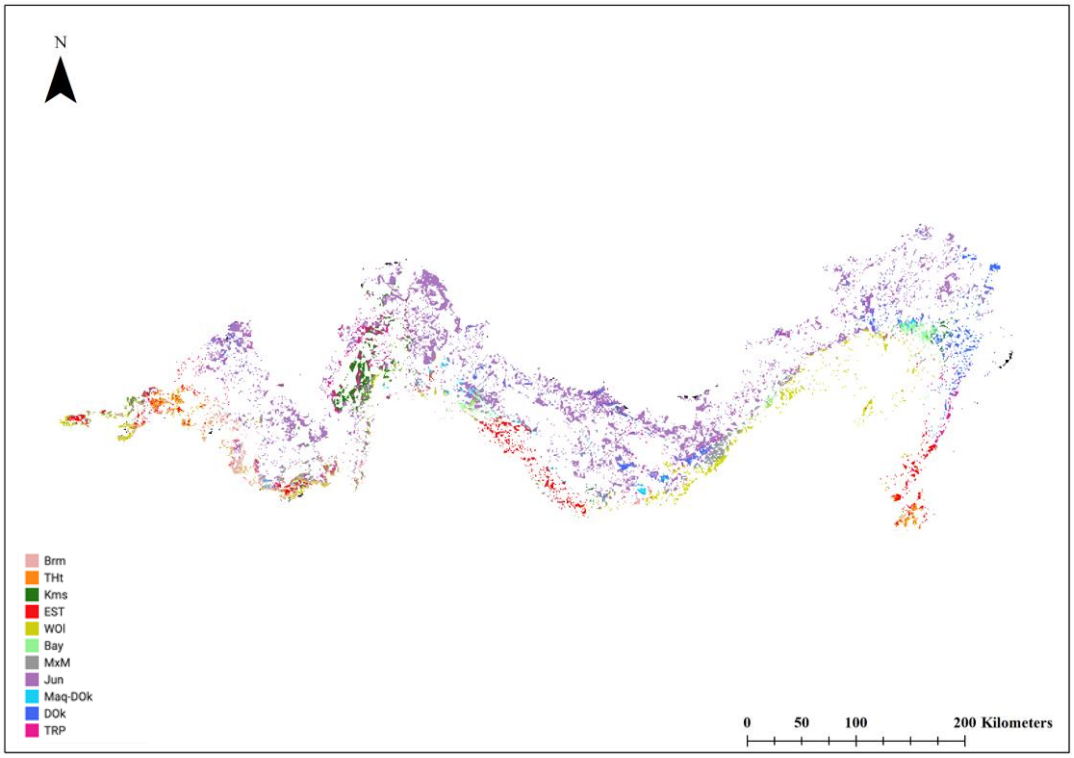

Figure 5.43. Alliance-level classification map with both set of features and the maquis mask.

5.7 Classification Accuracies

In order to produce the alliance-level classification maps, classifications were done on GEE. GEE has ready-to-use datasets that are instantly available, making it very convenient for large-scale geospatial analysis. Table 5.5 shows comparison between Cohen's kappa coefficient and the overall classification accuracy obtained by GEE's RF implementation and those obtained from the MATLAB's RF implementation by using the same sample points and predictor features. Results acquired from both programs show approximately the same outcome. For the remaining discussions of this thesis, only accuracies obtained from MATLAB will be discussed. GEE is used for convenience of obtaining region wide classification maps.

Table 5.5. Comparison between kappa values and overall RF classification accuracies acquired from GEE and MATLAB for classification using 21 combined features.

	Kappa	Overall Accuracy
GEE	0.80	82.1%
MATLAB	0.80	82.4%

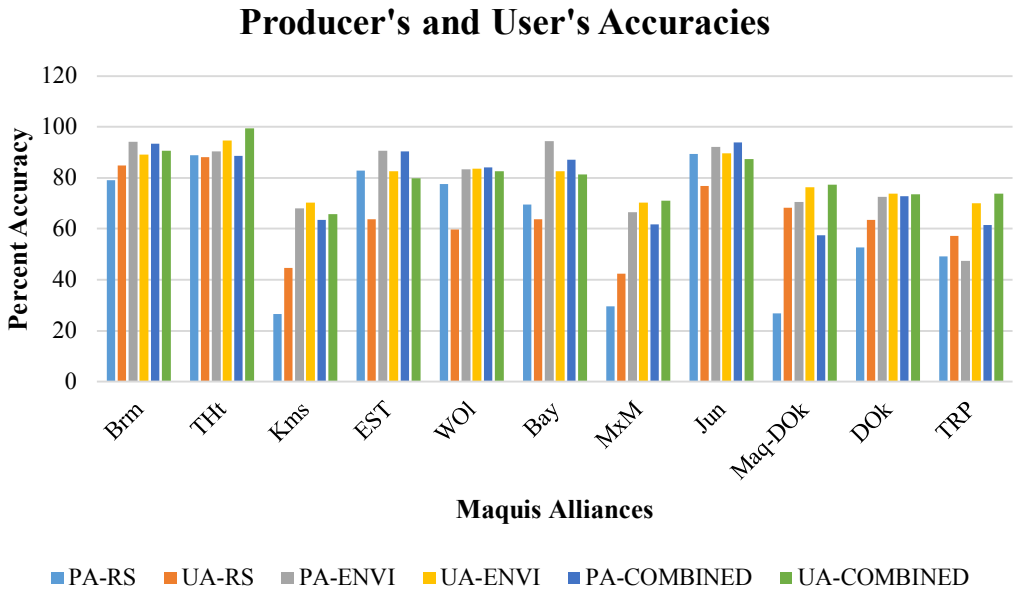

Figure 5.44. Producer's and User's accuracies for all three classification schemes.

Figure 5.44 shows a column chart showing the comparison between Producer's Accuracy (PA) and User's Accuracy (UA) for all three different classification schemes using RF. The details regarding results obtained from all three classification schemes using the RF classifier algorithm are explained in the following subsections.

5.7.1 Remotely-Sensed Features Classification Accuracy

Table 5.6 shows the confusion matrix of RF classification performed using remotely-sensed features. The overall accuracy obtained from remotely-sensed features is 66.1% (21 features with highest importance). Cohen's kappa coefficient is 0.63. PA ranged from 26.6% (*Quercus coccifera, Quercus ilex, Quercus aucheri,* Kermes Oak or Evergreen Oaks (Kms)) to 89.4% (*Juniperus spp.*, Junipers (Jun)) while UA ranged from 42.3% (Mixed Maquis (MxM)) to 88.1% (*Erica arborea*, Tree Heath (THt)) as can be seen in Table 5.6.

Kermes Oak or Evergreen Oaks were mostly misclassified as Wild Olive and as Laurel, Bay. This result is unexpected as Wild olive has a distinctive color that can be recognized even by the naked eye. The reason behind this might be due to a combination of contribution of grass, inaccuracies in radiometric correction, and sensor noise.

Confusion between Mixed Maquis with Eastern Strawberry Tree and Wild Olive is caused by the existence of these two alliances in the Mixed Maquis class.

And the large confusion between Deciduous Oak with Junipers is another unexpected result as autumn NDVI values of the two alliances should be very distinguishable. The grass growing in autumn may have compensated the decrease of Deciduous Oak's NDVI values.

Table 5.6. Confusion matrix of RF classification using remotely-sensed features.

	Brm	THt	Kms	EST	WOl	Bay	MxM	Jun	Maq-DOk	DOk	TRP	PA (%)
Brm	**406**	11	7	12	37	1	14	9			17	**79.0**
THt	13	**193**		3		1	3				4	**88.0**
Kms	8	1	**67**	19	48	40	18	20	2	13	16	**26.6**
EST	4		8	**360**	11	13	15	12	1	1	10	**82.8**
WOl	10		19	16	**353**	4	26	19		1	7	**77.6**
Bay	1		5	16	8	**220**	25	11	3	24	4	**69.4**
MxM	14	1	17	67	70	16	**110**	31	3	16	27	**29.6**
Jun	4	2	7	8	25	5	14	**831**	4	26	4	**89.4**
Maq-DOk	2		10	23	18	9	5	25	**43**	24	1	**26.9**
DOk	5	1	2	6	6	29	13	97	6	**191**	7	**52.6**
TRP	11	10	8	34	14	7	17	26	1	5	**129**	**49.2**
UA (%)	**84.9**	**88.1**	**44.7**	**63.8**	**59.8**	**63.8**	**42.3**	**76.9**	**68.3**	**63.5**	**57.1**	

5.7.2 Environmental Features Classification Accuracy

Table 5.7 shows the confusion matrix of RF classification performed using environmental features. The overall accuracy obtained from environmental features is 82.4% (for 21 features) with 0.80 Cohen's kappa coefficient. PA ranged from 47.3% (*Pinus brutia*, Turkish Red Pine (TRP)) to 94.3% (Laurel, Bay, *Laurus nobilis*) while UA ranged from 70.1% (*Pinus brutia*, Turkish Red Pine (TRP)) to 94.7% (*Erica arborea*, Tree Heath (THt)) as portrayed in Table 5.7.

Mixed Maquis were largely misclassified as Eastern Strawberry Tree and Wild Olive. This result is the same as the result obtained from classification using only remotely-sensed features, and the reason behind this is due to the existence of these two alliances in the Mixed Maquis class in unknown proportions.

Junipers can be seen to be misclassified as Turkish Red Pine. The reason behind this can because they tend to grow in similar environments.

Deciduous Oak were confused with Laurel, Bay and Junipers. The reason is also because they tend to grow in similar environments. Oak and junipers can frequently be observed together.

Table 5.7. Confusion matrix of RF classification using environmental features.

	Brm	THt	Kms	EST	WOl	Bay	MxM	Jun	Maq-DOk	DOk	TRP	PA (%)
Brm	**484**	6	2	1	5		12			1	3	**94.2**
THt	12	**196**		3		1	4				1	**90.3**
Kms	2		**171**	2	7	16	15	9	6	14	10	**67.9**
EST	2	2	2	**394**	4		16	1	9	4	1	**90.6**
WOl	19		13	10	**379**	5	15	6		1	7	**83.3**
Bay	1		5			**299**	1	4		6	1	**94.3**
MxM	14	3	13	27	26	2	**247**	12	2	15	11	**66.4**
Jun	1			2	9	9	5	**857**	8	24	15	**92.2**
Maq-DOk			6	17			3	13	**113**	7	1	**70.6**
DOk			12	5		27	13	35	5	**263**	3	**72.5**
TRP	8		19	16	24	3	21	21	5	21	**124**	**47.3**
UA (%)	**89.1**	**94.7**	**70.4**	**82.6**	**83.5**	**82.6**	**70.2**	**89.5**	**76.4**	**73.9**	**70.1**	

5.7.3 Combination of Remotely-Sensed Features and Environmental Features Classification Accuracy

The confusion matrix of RF classification using all combined features is shown in Table 5.8. The overall accuracy acquired from the combined features is 81.9% (for 21 features) and the Cohen's kappa coefficient is 0.80. PA ranged from 58.8% (Maquis – Deciduous Oak (Maq-DOk)) to 93.2% (*Genista acanthoclada*, Broom (Brm)) while UA ranged from 68.6% (Mixed Maquis) to 99.5% (*Erica arborea*, Tree Heath (THt)) as can be seen in Table 5.8.

Mixed Maquis were largely confused with Eastern Strawberry Tree and Deciduous Oak because these the MxM class might contain these alliances.

Junipers were largely misclassified as Deciduous Oak and vice versa is also true as Deciduous Oak can be seen to be largely misclassified as Junipers. The reason is because they grow in similar environments.

Table 5.8. Confusion matrix of RF classification using combination of remotely-sensed features and environmental features.

	Brm	**THt**	**Kms**	**EST**	**WOl**	**Bay**	**MxM**	**Jun**	**Maq-DOk**	**DOk**	**TRP**	**PA (%)**
Brm	**480**	1	3	2	12	1	6	2	1		6	**93.4**
THt	18	**192**		3			1				3	**88.5**
Kms	1		**160**	3	16	22	7	11	5	13	14	**63.5**
EST			2	**393**	6		20		6	2	6	**90.3**
WOl	11		13	9	**383**	6	19	7	1	1	5	**84.2**
Bay	1		11	1	5	**276**	1	10	1	11		**87.1**
MxM	12		27	30	24		**230**	12		23	14	**61.8**
Jun			1	2	8	5	8	**872**	6	24	4	**93.8**
Maq-DOk			5	25			3	24	**92**	10	1	**57.5**
DOk			6	7		26	13	37	6	**264**	4	**72.7**
TRP	6		15	17	9	3	16	23	1	11	**161**	**61.5**
UA (%)	**90.7**	**99.5**	**65.8**	**79.9**	**82.7**	**81.4**	**71.0**	**87.4**	**77.3**	**73.5**	**73.9**	

Further analyses are made by comparing the classification results obtained using different machine learning algorithms as can be seen in Table 5.9. RF algorithm shows the best results (OA = 81.9%, Kappa = 0.80), followed by SVM (OA = 46%, Kappa = 0.40), and QDA (OA = 68%, Kappa = 0.60). This classification was performed by using the same predictor features and default parameters.

Table 5.9. Classification accuracy obtained from different classifiers.

RF	SVM	QDA
81.9%	46%	68%

CHAPTER 6

DISCUSSIONS

6.1 Introduction

The objective of this chapter is to discuss all the findings of this study. Discussions about the resulting classification maps are done in Section 6.2 and discussions about the classification results (e.g., peak features, confusion matrix, overall accuracy, Cohen's kappa values) of all three classification schemes are done in Section 6.3.

6.2 Classification Maps

The classification maps produced in this study are of great importance, mainly in order to construct models that explain the dynamics of forest and maquis, as such models will help researchers to evaluate their role in ecosystems and predict their responses to climate change, but also for other benefits, such as forest fire-prevention management (Baeza et al., 2005), better use of economic resources in maquis areas, and wildlife protection.

The spatial resolution of the maps (20 m) is adequate enough for the purpose of differentiating maquis down to the alliance-level. And the accessibility of the GEE cloud computing platform with ready-to-use datasets that are instantly available makes it convenient for this study to efficiently be repeated for monitoring purposes as well as to be implemented on broader spatial extents.

Figure 6.1 presents the details of the total percentages that each class occupies within the masked area. Contrary to popular belief, *Pinus brutia* (TRP) make up less than

13% of the total masked areas for all three classification schemes. This is similar in conclusion to the findings of (Demirbas Caglayan et al., 2020).

The percentage of Junipers are much larger than the other alliances. The reason can be because of the existence of areas that are without trees or are covered with very sparse trees at high altitudes. Since these areas have the official status of forest, they are included in the maquis mask. Most of the Juniper polygons in the GT are sparse, and due to the lack of "steppe" class in the ontology, these areas are presumably classified as Juniper.

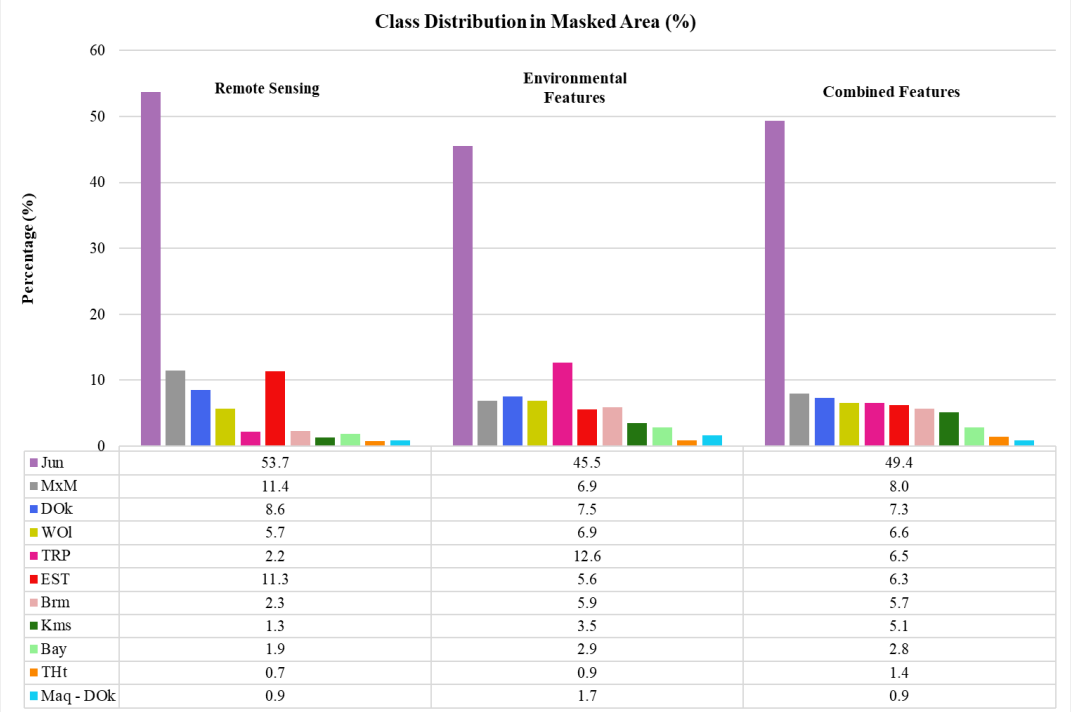

	Remote Sensing	Environmental Features	Combined Features
Jun	53.7	45.5	49.4
MxM	11.4	6.9	8.0
DOk	8.6	7.5	7.3
WOl	5.7	6.9	6.6
TRP	2.2	12.6	6.5
EST	11.3	5.6	6.3
Brm	2.3	5.9	5.7
Kms	1.3	3.5	5.1
Bay	1.9	2.9	2.8
THt	0.7	0.9	1.4
Maq - DOk	0.9	1.7	0.9

Figure 6.1. Percentages of each class in the masked areas obtained from all three classification schemes.

6.3 Classification Results

Classification results for all three classification schemes are highly accurate in comparison to other similar studies conducted in the Mediterranean climate (Clark, 2020; Demirbas Caglayan et al., 2020). The classification analysis in this study used the RF classifier in comparison to other classifiers (SVM and QDA). The results showed that for all three classification schemes, relative to SVM and QDA, the RF classifier resulted in the best classification accuracy. These results suggest that the RF classifier algorithm is an effective classifier thus should be considered in other shrublands classification applications. Table 6.1 shows the comparison of overall accuracies and Cohen's kappa values obtained with RF from different number of features. For all classification schemes, the highest accuracies are obtained when the peak number of features are used based on the RFE results.

Table 6.1. Comparison of OA and Cohen's kappa for all classification schemes.

Feature Set	**First 14 features**	**Peak features**
Remotely-sensed features	OA = 63.95% Cohen's kappa = 0.58	(32 features) OA = 66.15% Cohen's kappa = 0.61
Environmental features	OA = 80.02% Cohen's kappa = 0.77	(21 features) OA = 82.79% Cohen's kappa = 0.80
Combined features	OA = 82.49% Cohen's kappa = 0.80	(14 features) OA = 82.49% Cohen's kappa = 0.80

Several limitations were encountered throughout this study:

- The classifications were performed on manually picked dataset. Random selection may lead to different results.
- Application of the methodology performed in this study on other Mediterranean biomes is out of the scope of this thesis. No conclusions are derived regarding its applicability.

6.3.1 Classification Using Remotely-Sensed Features

Remotely-sensed features are successful in discriminating maquis alliances. However, these features have considerably higher importance when the pixels are of pure composition or composed of just one class. In this study, it was not always feasible to acquire sample points that solely consist of a single maquis class. This is caused by the highly diverse and complex nature of the maquis types. As a result, for some points, there are a number of classes contributing to the observed spectral response of the pixel. Hence the confusion between some classes (e.g., confusion between *Quercus coccifera*, *Quercus ilex*, *Quercus aucheri*, Mixed *Maquis*, and *Arbutus andrachne*, and confusion between *Quercus coccifera*, *Quercus ilex*, *Quercus aucheri*, Mixed *Maquis*, and *Laurus nobilis*).

Another obstacle that was encountered with remotely-sensed features is the variation of canopy cover. Not all alliances form a dominant class and some alliances (i.e., *Genista acanthoclada*, *Erica arborea*, and *Laurus nobilis*) have the tendency to grow as individual trees or small groups, resulting in high variability in canopy cover (density) of individual reference data. Partial canopy cover is generally a result of degradation due to anthropogenic pressure.

In addition to the variability in canopy cover, the 'contamination' of the signal with grasses due to unwanted contribution of adjacent grass pixels to the observed spectral response also lowers the performance of the remotely sensed features.

Obtaining cloud-free and snow-free imagery for the entire study area is a necessity when working with satellite imagery. However, due to the relatively vast study area, the chances to attain such images as input for a model are often decreased. As a result, images retrieved from winter months (December, January, and February, and partly March) had to be excluded due to the significant snow cover. Alliances that grow at higher altitudes (e.g., *Juniperus spp, Quercus coccifera, Quercus ilex, Quercus aucheri*) can be seen to show similar spectra due to snow cover, as explained in Section 5.4.1.

SWIR bands (B11 and B12) are highly affected by moisture. As a result, the reflectance of vegetation in these bands are generally low, while those of dry soil and rocks are relatively higher. At times and at certain places where moisture increased, which can be caused by several different factors such as recent precipitation or natural soil humidity, the reflectance will go down. This explains the peculiar behaviors of the spectral reflectance curves of B11 and B12, as can be observed in the spectral signatures of all the months as shown in Figure 5.5 to Figure 5.16.

6.3.2 Classification Using Environmental Features

Environmental features have a huge effect on the alliances, resulting in very high classification accuracy (82.4%) when classification is performed by using environmental features alone. This is true even with low resolution features and lack of soil and geology layers.

6.3.3 Classification Using Combination of Remotely-Sensed Features and Environmental Features

For the combined classification scheme, the feature with the highest importance is BIO2 (mean diurnal range). Mean diurnal range is calculated by taking the difference between the maximum mean monthly temperature and the minimum mean monthly temperature. It is reasonable that this feature proves to be the most significant as it can perfectly describe as well as limit the growing areas of each alliance.

Classification using combination of remotely-sensed features and environmental features produced approximately the same classification accuracy as the classification using only environmental features. However, the resulting classification map from the combined classification scheme is more heterogeneous. When frequent changes that can be observed in the field are considered, combining remotely-sensed features with environmental features could potentially result in a better accuracy than using environmental features alone. Nevertheless, a much denser dataset is required in order to achieve this. Additionally, classification performance with remotely-sensed features can be increased considerably if the contribution of grass is handled explicitly. In that case, one might expect the combination of both feature sets to perform better than environmental features alone.

As mentioned above, relative to SVM and QDA, the RF classifier improved the classification accuracy by 35.9 - 13.9%, respectively.

CHAPTER 7

CONCLUSIONS AND RECOMMENDATIONS FOR FUTURE WORK

7.1 Introduction

The objectives of this chapter are to summarize the study and to give recommendations for future work. They are distributed as follows: Section 7.2 summarizes all findings found in the study, Section 7.3 lists some recommendations for future work, and Section 7.4 explains the applications that will benefit from this study.

7.2 Conclusions

The aim of this study is to classify the areas labeled as maquis at alliance-level by means of machine learning algorithms and Sentinel-2 Level-2A multi-spectral imagery along with various environmental variables in the 95.000 km^2 Mediterranean Region of Turkey. Three different classification schemes are proposed: classification by using only remotely-sensed features, classification by using only environmental features, and classification by using remotely-sensed features and environmental features combined. All three classification schemes are evaluated by using the same sample points and training and testing methods, and then compared and analyzed. Analyses include comparisons between different resulting classified maps and results based on implemented features and comparisons between classifier algorithms for the combined scheme. This study produces the following conclusions:

- RF Classification using environmental features alone produced greater accuracy than RF classification using only remotely-sensed features. OA for classification using environmental features was 17.2% higher than classification using remotely-sensed features. However, the resulting classified map generated with remotely-sensed features alone showed much greater heterogeneity resembling the natural conditions in comparison to the classified map generated with environmental features. The reason is because the meteorological variables are interpolated from large grids in the order of kilometers and their variation is very smooth. Topographic features are also smooth when compared to pixel size. On the other hand, spectral measurements can change abruptly from a pixel to the next depending on the land cover.

- RF classification using environmental features alone produced approximately the same classification accuracy as classification using combination of environmental features and remotely-sensed features. Nevertheless, the resulting classification map from the combined classification scheme is more heterogeneous. When frequent changes that can be observed in the field are considered, combining remotely-sensed features with environmental features could potentially result in a better accuracy than using environmental features alone. However, a much denser dataset is required in order to achieve this. In addition, explicit handling of contribution from the grass can improve the remote sensing and combined results.

The analyses in this study were made possible because of the availability of the GT data, which were collected through an extensive field survey. These data were in adequate size and consistency, and evenly distributed throughout the entire study area. For larger spatial extents, such data might not be available or they might come from a number of different sources and collected with different collection methods, class distinctions, and error rates (Clark et al., 2018). All in all, having good and clean GT data in terms of quality, quantity, and distribution proves to be the most

important aspect for alliance-level classification mapping research in larger spatial scales.

7.3 Future Work

All alliances have diversity in lifeform and structural characteristics that increased spectral-temporal variation and complicated discrimination among them. Further research should focus on unraveling the ability of spectral-temporal variations to differentiate between alliances at broad spatial scales (Clark, 2020).

Based on the results obtained in this study, it is logical to assume that better classification accuracy can be obtained by explicitly addressing the canopy cover and contributions from the grass. Pixel level unmixing can also be used for addressing mixed classes. However, appropriate data set is required for this purpose. Better classification accuracy might also be obtained by using future hyperspectral satellites and by increasing the number of samples in poorly represented classes. Addition of soil and geology layers to the predictor features might also improve the classification accuracy.

7.4 Applications of this Study

This thesis can be applied for different years to see how the maquis distribution changes over year. This may give clues about the impact of fires, successions, etc. Since meteorological data is part of the prediction, the impact of future climate change can be predicted and this information can serve mitigation of the effects.

REFERENCES

Acker, J., Williams, R., Chiu, L., Ardanuy, P., Miller, S., Schueler, C., . . . Manore, M. (2014). Remote Sensing from Satellites. Elsevier. Retrieved from https://linkinghub.elsevier.com/retrieve/pii/B9780124095489094409

Almeida, F., Balbuena, A., Vazquez, R., & Cortes Macias, R. (2014). Trends and evolution of tourism in the Mediterranean Basin. *International Geographical Union Regional Conference at Krakow.*

Atalay, İ., & Efe, R. (2008). *International Symposium on Geography Environment and Culture in the Mediterranean Region Ecoregions of the Mediterranean Area and the Lakes Region of Turkey.*

Atalay, I., Efe, R., & Öztürk, M. (2014, 3 19). Ecology and Classification of Forests in Turkey. *Procedia - Social and Behavioral Sciences, 120*, 788-805.

Atalay, I., Efe, R., & Öztürk, M. (2014, 3 19). Effects of Topography and Climate on the Ecology of Taurus Mountains in the Mediterranean Region of Turkey. *Procedia - Social and Behavioral Sciences, 120*, 142-156.

Baeza, M., Valdecantos, A., & Vallejo, R. (2005). Management of Mediterranean shrublands for forest fire prevention. In M. Baeza, A. Valdecantos, & R. Vallejo.

Bajocco, S., De Angelis, A., & Salvati, L. (2012, 12 1). A satellite-based green index as a proxy for vegetation cover quality in a Mediterranean region. *Ecological Indicators, 23*, 578-587.

Breiman, L. (2001). Random Forests. *Machine Learning, 45*(1), 5-32.

Brodley, C., & Friedl, M. (1997, 9 1). Decision tree classification of land cover from remotely sensed data. *Remote Sensing of Environment, 61*(3), 399-409.

Caliskan, B. K., & Zeydanli, U. (2020). *Identification and Mapping of the Maquis of Mediterranean Region of Turkey.* Ankara.

Caprioli, M., Di Bari, P., Leone, A., Ripa, M., Tarantino, E., Caprioli, M., . . . Tarantino, E. (2003). *A Hybrid Land Cover Classification of Landsat-7 Etm+ Data for an Efficient Vegetation Mapping.*

Casermeiro, M., Molina, J., De La Cruz Caravaca, M., Hernando Costa, J., Hernando Massanet, M., & Moreno, P. (2004, 6 1). Influence of scrubs on runoff and sediment loss in soils of Mediterranean climate. *Catena, 57*(1), 91-107.

Castro-Esau, K., Sa´nchez, G., Sa´nchez-Azofeifa, S., Rivard, B., Wright, S., & Quesada, M. (2006). *Variability in leaf optical properties of mesoamerican trees and the potential for species classification.*

Cheng, K., & Wang, J. (2019). Forest type classification based on integrated spectral-spatial-temporal features and random forest algorithm-A case study in the Qinling Mountains. *Forests, 10*(7).

Clark, M. L. (2017, 10). Comparison of simulated hyperspectral HyspIRI and multispectral Landsat 8 and Sentinel-2 imagery for multi-seasonal, regional land-cover mapping. *Remote Sensing of Environment, 200*, 311-325.

Clark, M. L. (2020, 1). Comparison of multi-seasonal Landsat 8, Sentinel-2 and hyperspectral images for mapping forest alliances in Northern California. *ISPRS Journal of Photogrammetry and Remote Sensing, 159*, 26-40.

Clark, M. L., Buck-Diaz, J., & Evens, J. (2018, 6). Mapping of forest alliances with simulated multi-seasonal hyperspectral satellite imagery. *Remote Sensing of Environment, 210*, 490-507.

Cowling, R., Rundel, P., Lamont, B., Arroyo, M., & Arianoutsou, M. (1996). Plant diversity in mediterranean-climate regions. *Trends in Ecology and Evolution, 11(9)*, 362-366. Elsevier Ltd.

Dadon, A., Mandelmilch, M., Ben-Dor, E., & Sheffer, E. (2019, 11 27). Sequential PCA-based Classification of Mediterranean Forest Plants using Airborne Hyperspectral Remote Sensing. *Remote Sensing, 11*(23), 2800.

De Jong, S., & Burrough, P. (1995). *A Fractal Approach to the Glassification of Mediterranean Vegetation Types in Remotely Sensed lmages.*

Demirbas Caglayan, S., Leloglu, U. M., Bilgin, C., Waser, L., & Psomas, A. G. (2020). Species Level Classification of Mediterranean Sparse Forests - Maquis Formations Using Sentinel-2 Imagery. *Geocarto International*.

Domaç, A., & Süzen, M. L. (2006, 4). Integration of environmental variables with satellite images in regional scale vegetation classification. *International Journal of Remote Sensing, 27*(7), 1329-1350.

Efe, R., Cravins, G., .z türk, M., & Atalay, I. (2008). *Natural Environment and Culture in the Mediterranean Region.* Cambridge Scholars Pub.

ESRI. (2020). *Curvature function—Help*. Retrieved from ArcGIS for Desktop: https://desktop.arcgis.com/en/arcmap/10.3/manage-data/raster-and-images/curvature-function.htm

Evans, J. S., Murphy, M. A., Holden, Z. A., & Cushman, S. A. (2011). Modeling species distribution and change using random forest. *Predictive Species and Habitat Modeling in Landscape Ecology: Concepts and Applications*, 139-159.

Gabarrón-Galeote, M., Martínez-Murillo, J., Quesada, M., & Ruiz-Sinoga, J. (2013, 12 11). Seasonal changes in the soil hydrological and erosive response depending on aspect, vegetation type and soil water repellency in different mediterranean microenvironments. *Solid Earth, 4*(2), 497-509.

Gao, B. C. (1996, 12). *NDWI - A normalized difference water index for remote sensing of vegetation liquid water from space*.

Gorelick, N., Hancher, M., Dixon, M., Ilyushchenko, S., Thau, D., & Moore, R. (2017). Google Earth Engine: Planetary-scale geospatial analysis for everyone. *Remote Sensing of Environment*.

Grabska, E., Hostert, P., Pflugmacher, D., & Ostapowicz, K. (2019, 5). Forest stand species mapping using the sentinel-2 time series. *Remote Sensing, 11*(10).

Gregorutti, B., Michel, B., & Saint-Pierre, P. (2017, 5 1). Correlation and variable importance in random forests. *Statistics and Computing, 27*(3), 659-678.

Grignetti, A., Salvatori, R., Casacchia, R., & Manes, F. (1997). Mediterranean vegetation analysis by multi-temporal satellite sensor data. *International Journal of Remote Sensing, 18*(6), 1307-1318.

Grossman, D., Faber-Langendoen, D., Weakley, A., Anderson, M., Bourgeron, P., Crawford, R., . . . Sneddon, L. (1998). International classification of ecological communities: terrestrial vegetation of the United States. Volume 1. The National Vegetation Classification System: development, status, and applications.

Hijmans, R., Cameron, S., Parra, J., Jones, P., & Jarvis, A. (2005, 12 1). Very high resolution interpolated climate surfaces for global land areas. *International Journal of Climatology, 25*(15), 1965-1978.

Huete, A. R. (1988). A soil-adjusted vegetation index (SAVI). *Remote Sensing of Environment, 25*(3), 295-309.

Immitzer, M., Vuolo, F., & Atzberger, C. (2016, 2 23). First Experience with Sentinel-2 Data for Crop and Tree Species Classifications in Central Europe. *Remote Sensing, 8*(3), 166.

Jarvis, A., Guevara, E., Reuter, H., & Nelson, A. (2008). Hole-filled SRTM for the globe : version 4 : data grid.

Jiang, H., Deng, Y., Chen, H., Tao, L., Sha, Q., Chen, J., . . . Zhang, S. (2004, 6 24). Joint analysis of two microarray gene-expression data sets to select lung adenocarcinoma marker genes. *BMC Bioinformatics, 5*.

Joffre, R., & Rambal, S. (2001). Mediterranean Ecosystems. In R. Joffre, & S. Rambal, *Encyclopedia of Life Sciences.* John Wiley & Sons, Ltd.

Justice, C., Townshend, J., Holben, A., & Tucker, C. (1985). Analysis of the phenology of global vegetation using meteorological satellite data. *International Journal of Remote Sensing, 6*(8), 1271-1318.

Kampouri, M., Kolokoussis, P., Argialas, D., & Karathanassi, V. (2019, 10 15). Mapping of forest tree distribution and estimation of forest biodiversity using Sentinel-2 imagery in the University Research Forest Taxiarchis in Chalkidiki, Greece. *Geocarto International, 34*(12), 1273-1285.

Karasiak, N., Sheeren, D., Fauvel, M., Willm, J., Dejoux, J. F., & Monteil, C. (2017, 9). Mapping tree species of forests in southwest France using Sentinel-2 image time series. *2017 9th International Workshop on the Analysis of Multitemporal Remote Sensing Images, MultiTemp 2017*.

Kauth, R., & Thomas, G. S. (1976). The tasselled cap - A graphic description of the spectral-temporal development of agricultural crops as seen by Landsat.

Kollert, A., Bremer, M., Löw, M., & Rutzinger, M. (2021, 2). Exploring the potential of land surface phenology and seasonal cloud free composites of one year of Sentinel-2 imagery for tree species mapping in a mountainous region. *International Journal of Applied Earth Observation and Geoinformation, 94*, 102208.

Lapini, A., Pettinato, S., Santi, E., Paloscia, S., Fontanelli, G., & Garzelli, A. (2020, 1 22). Comparison of Machine Learning Methods Applied to SAR Images for Forest Classification in Mediterranean Areas. *Remote Sensing, 12*(3), 369.

Laurin, G., Avezzano, R., Bacciu, V., Frate, F., Papale, D., & Virelli, M. (2018, 6 1). Cosmo-skymed potential to detect and monitor mediterranean maquis fires and regrowth: A pilot study in Capo Figari, Sardinia, Italy. *IForest, 11*(3), 389-395.

Lehner, B., & Grill, G. (2013, 7 15). Global river hydrography and network routing: Baseline data and new approaches to study the world's large river systems. *Hydrological Processes, 27*(15), 2171-2186.

Lehner, B., Verdin, K., & Jarvis, A. (2008, 3 4). New global hydrography derived from spaceborne elevation data. *Eos, Transactions American Geophysical Union, 89*(10), 93-94.

Lwin, K. K., Ota, T., Shimizu, K., & Mizoue, N. (2019, 12). Assessing the importance of tree cover threshold for forest cover mapping derived from global forest cover in Myanmar. *Forests, 10*(12).

Macintyre, P., van Niekerk, A., & Mucina, L. (2020, 3 1). Efficacy of multi-season Sentinel-2 imagery for compositional vegetation classification. *International Journal of Applied Earth Observation and Geoinformation, 85*, 101980.

Manevski, K., Manakos, I., Petropoulos, G., & Kalaitzidis, C. (2011, 12 1). Discrimination of common Mediterranean plant species using field spectroradiometry. *International Journal of Applied Earth Observation and Geoinformation, 13*(6), 922-933.

Maselli, F., Rodolfi, A., Romanelli, S., Conese, C., & Bottai, L. (2000). Classification of Mediterranean vegetation by TM and ancillary data for the evaluation of fire risk. *International Journal of Remote Sensing, 21*(17), 3303-3313.

Mather, P., & Tso, B. (2016). *Classification Methods for Remotely Sensed Data.* CRC Press.

MATLAB. (2019). *9.7.0.1190202 (R2019b).* Natick, Massachusetts: The MathWorks Inc.

Médail, F. (2008). Mediterranean. In F. Médail, *Encyclopedia of Ecology, Five-Volume Set* (pp. 2296-2308). Elsevier Inc.

Mountrakis, G., Im, J., & Ogole, C. (2011, 5). Support vector machines in remote sensing: A review. *ISPRS Journal of Photogrammetry and Remote Sensing, 66*(3), 247-259.

O'donnell, M., & Ignizio, D. (2012). *Bioclimatic Predictors for Supporting Ecological Applications in the Conterminous United States Data Series 691.* U.S. Geological Survey (USGS).

Olson, D. M., Dinerstein, E., Wikramanayake, E. D., Burgess, N. D., Powell, G. V., Underwood, E. C., . . . Kassem, K. (2001). Terrestrial ecoregions of the world: A new map of life on Earth. *BioScience, 51*(11), 933-938.

Palahi, M., Mavsar, R., Gracia, C., Birot, Y., & Garcia, C. (2008). *Mediterranean forests under focus Regard sur les forêts méditerranéennes.*

Peet, F., & Sahota, T. (1986). Surface Curvature as a Measure of Image Texture. *IEEE Transactions on Pattern Analysis and Machine Intelligence, PAMI-7*(6), 734-738.

Pelletier, C., Valero, S., Inglada, J., Champion, N., & Dedieu, G. (2016, 12). Assessing the robustness of Random Forests to map land cover with high resolution satellite image time series over large areas. *Remote Sensing of Environment, 187*, 156-168.

Persson, M., Lindberg, E., & Reese, H. (2018, 11). Tree Species Classification with Multi-Temporal Sentinel-2 Data. *Remote Sensing, 10*(11), 1794. Retrieved from http://www.mdpi.com/2072-4292/10/11/1794

Pettorelli, N., Vik, J. O., Mysterud, A., Gaillard, J. M., Tucker, C. J., & Stenseth, N. C. (2005, 9). Using the satellite-derived NDVI to assess ecological responses to environmental change. *Trends in Ecology and Evolution, 20*(9), 503-510.

Rouse, J., Haas, R., Schell, J., & Deering, D. (1973). *Monitoring the Vernal Advancement and Retrogradation (Green Wave Effect) of Natural Vegetation.* Texas.

(2013). *SENTINEL-2 User Handbook.* European Space Agency.

Shoshany, M. (2000). *Satellite remote sensing of natural Mediterranean vegetation: a review within an ecological context.*

Suc, J. P. (1984). Origin and evolution of the mediterranean vegetation and climate in Europe. *Nature, 307*(5950), 429-432.

The European Space Agency. (2020). Retrieved from https://www.esa.int/

Tomaselli, R. (1977). Degradation of the Mediterranean maquis. *Ambio, 6*(6), 356-362.

TSMS - Turkish State Meteorological Service. (2020). Retrieved July 6, 2020, from https://mevbis.mgm.gov.tr/mevbis/ui/index.html#/Workspace

Wessel, M., Brandmeier, M., & Tiede, D. (2018). Evaluation of different machine learning algorithms for scalable classification of tree types and tree species based on Sentinel-2 data. *Remote Sensing, 10*(9).

Wu, W. (2014, 1). The Generalized Difference Vegetation Index (GDVI) for Dryland Characterization. *Remote Sensing, 6*(2), 1211-1233. Retrieved from http://www.mdpi.com/2072-4292/6/2/1211

Zimmermann, N. E., Edwards, T. C., Moisen, G. G., Frescino, T. S., & Blackard, J. A. (2007). Remote sensing-based predictors improve distribution models of rare, early successional and broadleaf tree species in Utah. *Journal of Applied Ecology, 44*(5), 1057-1067.

APPENDICES

A. Appendix A: Details of the Alliances

All photographs listed on Appendix A are courtesy of Dr. Uğur Zeydanlı (DKM archive).

Table A.1. Details of alliance: *Sarcopoterium spinosum*.

Latin Name	*Sarcopoterium spinosum*	
Turkish Name	Sarcopeterium	
English Name	Prickly, spiny, or thorny burnet	
Abbreviation		
Habitus	Shrub: Compact, cushion, or mound forming, dense	
Physiognomic features	Evergreen, broad-leaved	

Table A.2. Details of alliance: *Genista acanthoclada*.

Latin Name	*Genista acanthoclada*
Turkish Name	Genista
English Name	Broom
Abbreviation	Brm
Habitus	Shrub: Dense, bushy
Physiognomic features	Deciduous, broad-leaved

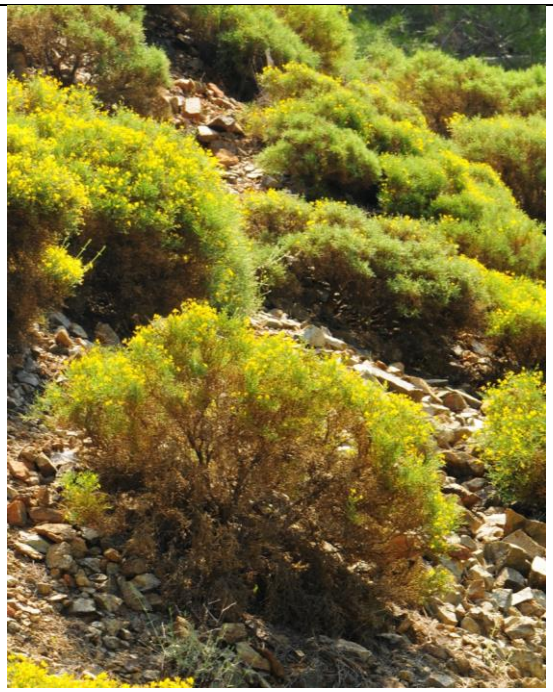

Table A.3. Details of alliance: *Erica arborea*.

Latin Name	*Erica arborea*
Turkish Name	Püren
English Name	Tree Heath
Abbreviation	THt
Habitus	Shrub: Dense, low growing shrub
Physiognomic features	Evergreen, broad-leaved

Table A.4. Details of alliance: *Quercus coccifera (Quercus ilex, Quercus aucheri)*.

Latin Name	*Quercus coccifera (Quercus ilex, Quercus aucheri)*	
Turkish Name	Kermes, pırnal, boz pırnal	
English Name	Kermes oak (including other evergreen oak)	
Abbreviation	Kms	
Habitus	Shrub-Small tree: Thorny shrub which can grow up to 10 m	
Physiognomic features	Evergreen, broad-leaved	

Table A.5. Details of alliance: *Arbutus andrachne*.

Latin Name	*Arbutus andrachne*
Turkish Name	Sandal
English Name	Eastern Strawberry Tree
Abbreviation	EST
Habitus	Shrub-Small tree: Dense high growing shrub which can go up to 8 m
Physiognomic features	Evergreen, broad-leaved

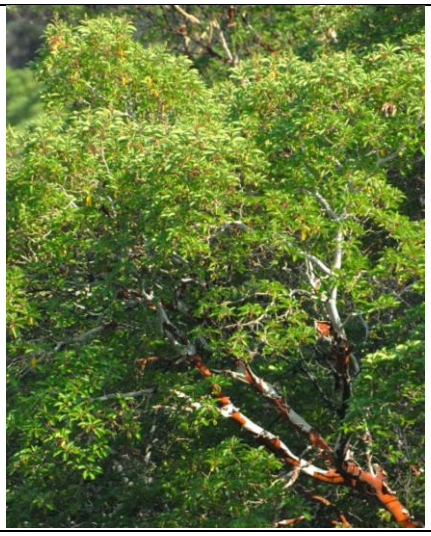

Table A.6. Details of alliance: *Olea europea ssp. europea var. sylvestris*.

Latin Name	*Olea europea ssp. europea var. sylvestris*
Turkish Name	Zeytin
English Name	Wild olive
Abbreviation	WOl
Habitus	Shrub - small tree: One of the tallest elements of the maquis which can grow up to 12 m
Physiognomic features	Evergreen, broad-leaved

Table A.7. Details of alliance: *Laurus nobilis*.

Latin Name	*Laurus nobilis*
Turkish Name	Akdeniz defnesi
English Name	Bay, Laurel
Abbreviation	Bay
Habitus	Shrub-Small tree: Maquis element which can grow up to 15 m along the streams
Physiognomic features	Evergreen, broad leaved

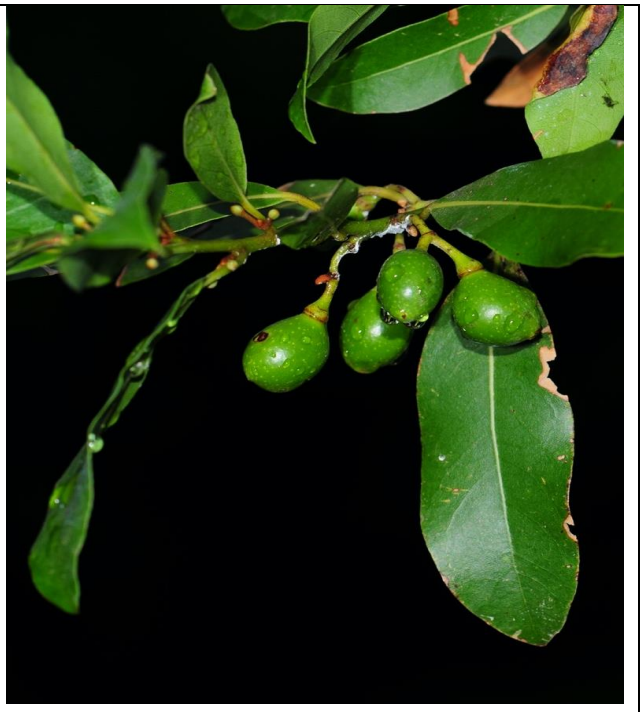

Table A.8. Details of alliance: Mixed *Maquis*.

Latin Name	Mixed *Maquis*
Turkish Name	Karışık
English Name	Mixed *Maquis*
Abbreviation	MxM
Habitus	
Physiognomic features	

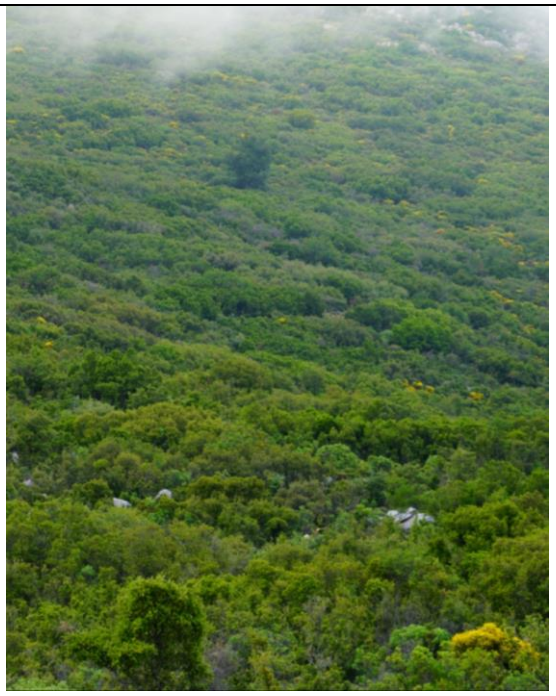

Table A.9. Details of alliance: *Cercis siliquastrum*.

Latin Name	*Cercis siliquastrum*
Turkish Name	Erguvan
English Name	Judas-tree
Abbreviation	
Habitus	Small tree
Physiognomic features	Deciduous, broad-leaved

Table A.10. Details of alliance: *Styrax officinalis*.

Latin Name	*Styrax officinalis*
Turkish Name	Tesbih
English Name	Storax
Abbreviation	
Habitus	Shrub: 2-5 m
Physiognomic features	Deciduous, broad-leaved

Table A.11. Details of alliance: *Ceratonia siliqua*.

Latin Name	*Ceratonia siliqua*	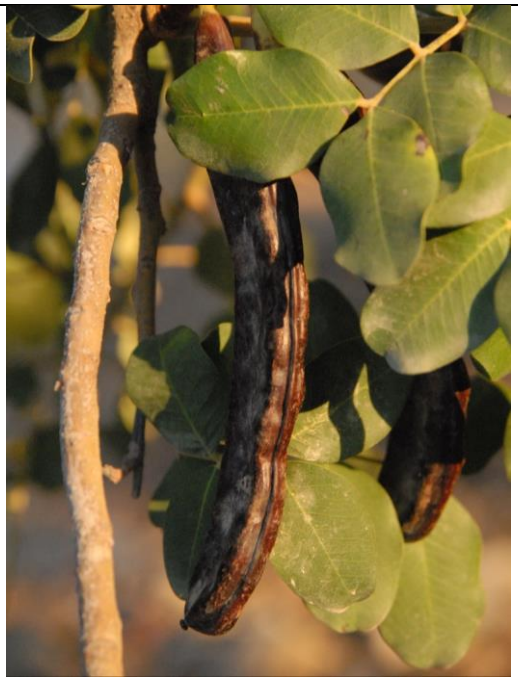
Turkish Name	Harnup	
English Name	Carob	
Abbreviation		
Habitus	Small tree: 5-10 m	
Physiognomic features	Evergreen, broad-leaved	

Table A.12. Details of alliance: *Nerium oleander*.

Latin Name	*Nerium oleander*	
Turkish Name	Zakkum	
English Name	Nerium or oleander	
Abbreviation		
Habitus	Shrub: 2-5 m	
Physiognomic features	Evergreen, broad-leaved	

Table A.13. Details of alliance: *Pistacia terebinthus*.

Latin Name	*Pistacia terebinthus*
Turkish Name	Menengiç
English Name	Turpentine tree or terebinth
Abbreviation	
Habitus	Shrub-Small tree: Which can grow up to 8 m
Physiognomic features	Deciduous, broad-leaved

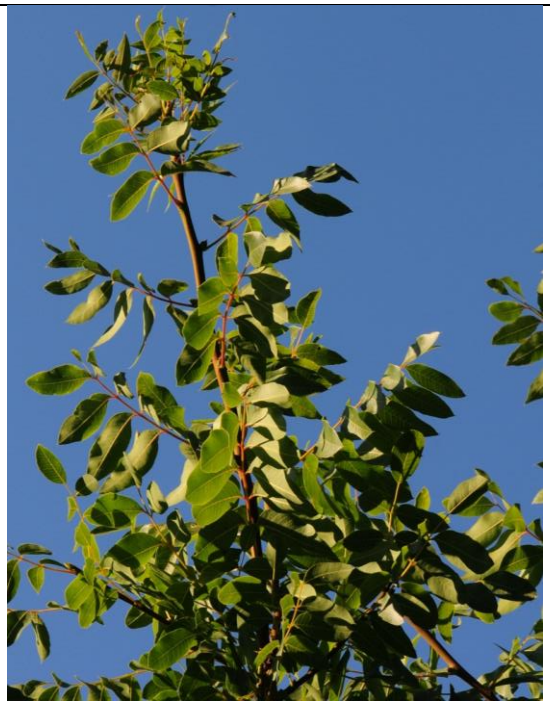

Table A.14. Details of alliance: *Pistacia vera*.

Latin Name	*Pistacia vera*
Turkish Name	Antep Fıstığı
English Name	Pistachio
Abbreviation	
Habitus	Small tree: Which can grow up to 8 m
Physiognomic features	Deciduous, broad-leaved

Table A.15. Details of alliance: *Vitex agnus-castus*.

Latin Name	*Vitex agnus-castus*	
Turkish Name	Hayıt	
English Name	Chastetree	
Abbreviation		
Habitus	Shrub	
Physiognomic features	Deciduous, broad-leaved	

Table A.16. Details of alliance: *Juniperus drupacea - Quercus coccifera.*

Latin Name	*Juniperus drupacea - Quercus coccifera*	
Turkish Name	Andız ardıcı - Kermes	
English Name	Syrian juniper - Kermes oak	
Abbreviation	Jun	
Habitus	Tree- Shrub	
Physiognomic features	-Evergreen, needle-leaved -Evergreen, broad-leaved	

Table A.17. Details of alliance: *Juniperus oxycedrus – Quercus coccifera*.

Latin Name	*Juniperus oxycedrus - Quercus coccifera*
Turkish Name	Katran ardıcı - Kermes
English Name	Prickly juniper - Kermes oak
Abbreviation	Jun
Habitus	Shrub – small tree
Physiognomic features	-Evergreen, needle-leaved -Evergreen, broad-leaved

Table A.18. Details of alliance: *Juniperus excelsa*.

Latin Name	*Juniperus excelsa*
Turkish Name	Boylu ardıç
English Name	Greek juniper
Abbreviation	Jun
Habitus	Small tree – Tree: Which can grow up to 25 m in suitable habitats
Physiognomic features	Evergreen, scale-like leaved

Table A.19. Details of alliance: *Juniperus oxycedrus*.

Latin Name	*Juniperus oxycedrus*
Turkish Name	Katran Ardıcı
English Name	Prickly juniper
Abbreviation	Jun
Habitus	Small tree- Tree: Which can grow up to 20 m in suitable habitats
Physiognomic features	Evergreen, needle-leaved

Table A.20. Details of alliance: *Juniperus drupacea*.

Latin Name	*Juniperus drupacea*
Turkish Name	Andız ardıcı
English Name	Syrian juniper
Abbreviation	Jun
Habitus	Small tree – Tree: Which can grow up to 25 m in suitable habitats
Physiognomic features	Evergreen, needle-leaved

Table A.21. Details of alliance: *Maquis – Quercus sp.* (*Q. trojana, libani, cerris*).

Latin Name	*Maquis – Quercus sp. (Q. trojana, libani, cerris)*	
Turkish Name	Maki - Yaprak Döken Meşe	
English Name	Maki - Deciduous oak	
Abbreviation	Mak-DOk	
Habitus	Shrub-Small Tree	
Physiognomic features	Evergreen-Deciduous, Broad-leaved	

Table A.22. Details of alliance: *Quercus sp.* (*Q. trojani, libani, cerris, ithaburensis*).

Latin Name	*Quercus sp. (Q. trojani, libani, cerris, ithaburensis)*	
Turkish Name	Yaprak Döken Meşe	
English Name	Deciduous oak	
Abbreviation	DOk	
Habitus	Shrub-Small Tree	
Physiognomic features	Deciduous, Broad-leaved	

Table A.23. Details of alliance: *Pinus brutia*.

Latin Name	*Pinus brutia*
Turkish Name	Kızılçam
English Name	Turkish Red Pine
Abbreviation	TRP
Habitus	Tree
Physiognomic features	Evergreen, needle-leaved